QUANTIFYING EVAPORATION IN THE LOWER ATMOSPHERE USING MACHINE DRIVEN CURVE FITTING TO PARAMETERIZE DROP SIZE DISTRIBUTIONS

A Thesis

presented to

the Faculty of the Graduate School

at the University of Missouri - Columbia

In Partial Fulfillment

of the Requirements for the Degree

Master of Science

---

by

CHRISTOPHER A STEWARD

Dr. Neil Fox: Advisor

May 2020

The undersigned, appointed by the dean of the Graduate School, have examined the thesis entitled

QUANTIFYING EVAPORATION IN THE LOWER ATMOSPHERE USING MACHINE DRIVEN CURVE FITTING TO PARAMETERIZE DROP SIZE DISTRIBUTIONS

Presented by Christopher A. Steward,

a candidate for the degree of Master of Science,

and hereby certify that, in their opinion, it is worthy of acceptance.

_____

Dr. Neil Fox

_____

Dr. Anthony Lupo

_____

Dr. Allen Thompson

ACKNOWLEDGEMENTS

I would like to start off by expressing my sincerest gratitude to all my professors for guiding me through this journey I embarked on after a 6 years hiatus from academics. Dr. Neil Fox's, Dr. Anthony Lupo's and Dr. Patrick Market's patience, words of wisdom and unrelenting encouragement not only allowed me to accomplish my original goal of completing my undergraduate, it gave me the confidence and wherewithal to move on to the next level of doing what I love. I would also like to thank Dr. Allen Thompson for his expertise and allowing me to explore other research routes during my graduate study. I hope to work with him in future research projects involving hydrometeor parameterization. I would also like to thank the Missouri Student Veterans Association for providing outstanding service and advice to myself and all the Mizzou Student Veterans utilizing the GI bill.

The accomplishment of this research would have been impossible without the help of Evan Travis and Brendan Heaven as well as all the undergraduates from the Mizzou Meteorology Club who would answer the call when extra hands were needed for balloon observations and forecast guidance. Thanks to Jon Bongard for his tutelage, allowing me to jump headfirst into this research as well as his unconditional friendship. Also, thanks to Paula Sumrall and all the other graduate students for their love and support in the most trying of times.

Most importantly, thanks to my three children Addison, Jackson and Rowen for their understanding and remarkable resilience, allowing their dad to follow his dream. Thanks to my mother Lisa Cooper, stepfather Dr. Tracy Cooper, my father Robert Steward, my sister MU alumn Caitlin Steward and my brother Micheal Steward for their love and encouragement through all these years. Also, thanks to Liz Barry for her incredible support, love and compassion. And lastly, thanks to my stepmother Dr. Kerry Clark for her wisdom, unwavering love and inspiration of which I am forever grateful.

Table of Contents

Contents

LIST OF TABLES AND FIGURES

Figures

Figure Page

Tables

Table Page

ABSTRACT

Evaporation of hydrometeors in the atmosphere is a process by which liquid water becomes water vapor. Consequences of this process can affect quantitative precipitation forecasts, convective downdrafts quantification, flooding forecasts, and many other forecasting parameters. Accurate and precise forecast modeling often misrepresents this microscale process due to the multiple feedbacks involved, and under- or mis- quantified parameters. Resolving parameters such as the drop size distribution and statistical representation will help to rectify these inadequacies. In this study, multiple observation instruments are used to observe how rain evolves in a dry atmosphere. Instruments include weather balloon radiosondes, laser disdrometers and a vertically pointing micro-rain radar (MRR). These data are then processed using a multitude of modeling methods to best quantify evaporation rates.

Several case studies were conducted with the goal of observing and modeling evaporation in a dry layer. Using the MRR and disdrometer data, drop size distributions were observed from the base of the cloud layer to the surface. Calculated liquid water content was used as a parameter to compare the modeled change in water content to the MRR and disdrometer observations. Through this process, a newly developed drop size distribution parameterization using linear regression modeling and a Gaussian distribution mixture was implemented and was shown to be a better method, capturing the larger drops in the distribution. The Gaussian mixture also demonstrated an accurate parameterization in the evaporation quantification when vertical motions were accurately represented. However, accurately quantifying vertical motions using balloon data was problematic in the cases presented and will need to be the subject for future interrogation.

1. Introduction

1.1 Purpose

Through the evaporative process, the microphysical changes that occur in the atmosphere can influence subsequently more changes in the dynamical influences on storm or system behaviors. The result of this process has been shown to increase the baroclinicity across a surface frontal boundary (Barth and Parsons 1996). This also becomes apparent when considering cold pooling due to the latent heat exchange of evaporation and sublimation. Evaporation is responsible for maintaining downdrafts under the base of clouds for both cold and warm core rain processes (Li and Srivastava 2001). Furthermore, evaporation impacts forecast accuracy in quantitative precipitation forecasts (QPF) where it can result in an overestimation of rain fall rates and inaccurate rainfall onset (Pallardy and Fox 2018). The presence of a dry layer between the cloud base and the surface is a common occurrence in both convective and non-convective rain processes in the Midwestern United States (Iselin et al. 1997). Evaporation rates within a dry layer are determined by several environmental factors. The vertical motion of the air, the depth and strength of the dry layer, and the evolving drop size concentration distribution from below the cloud base are all factors to be accounted for in the quantification of evaporation.

Previous works attempting to account for evaporation and other microphysical processes were limited by the ability to observe the microphysical processes and to resolve large data sets and accurately incorporate this data into model QPF forecasts due to computational inadequacies (Georgakakos and Hudlow 1984). This led to highly parameterized and inaccurate quantities in forecasts that have been carried on through the

years (Duda et al. 2014). New technologies in meteorological and hydrological sensors and computing capability have opened the door for studies in these microphysical endeavors, much of which are utilized in this study. Li and Srivastava (2001) showed that using a rainfall rate reflectivity relationship (Z-R) and differential reflectivity (ZDR) a correlation can be quantified using a single drop parameter. This study makes several assumptions that can misrepresent how rainfall behaves in the atmosphere. A steady vertical distribution of the temperature and humidity profile as well as no vertical motions are both assumed. Drop sorting through vertical wind shear and collision and coalescence are also neglected. This study did however observe evaporation using a Z-ZDR relationship more accurately than evaporation estimates from a simple Z relationship. This analytical solution paved the way for further studies in using dual polarization in evaporation estimates.

Pallardy and Fox (2018) using the Z-ZDR relationship sought to observe and improve the radar rainfall estimations by using observations from dual-polarization radar and a network of rain gauges. The findings of this research suggest that radar rainfall estimates are inaccurate at the surface due to a static evaporation scheme or no scheme whatsoever. This becomes exacerbated as beam height increases and the range increases from the radar's position where equivalent relative humidity is neglected through a significant portion of the atmospheric column. This increased range also inherently changes the atmospheric conditions in which the rain is being observed and the accuracy of modeled evaporation rates. Using model soundings as representation also poses a question as to the accuracy of the evaporation quantification through a modeled profile and is addressed in this study. Also noted in Pallardy and Fox (2018) was that heavier rainfall estimations

by the radar and observed by the gauges underestimated the rainfall totals. One factor possibly influencing radar rainfall estimations noted was the accuracy of the modeled DSD. This study will cover the current schemes being used, as well as propose a new method of modeling distributions using a Gaussian model and machine learning capabilities.

A way to resolve the inaccuracies of the beam height sampling is observing rainfall through the vertical column. Such methods were accomplished by Williams (2016). The William's study set up two vertically pointing radars, positioned to observe vertical motions and changing DSDs, then related those changes to the change in LWC as a measure of evaporation. Williams's 2-month field research concluded that using vertical pointing radars was an appropriate method to study microphysical states of rain processes. By evaluating vertical changes at discrete times and heights of rain drop size, concentrations and LWC could be accurately assessed. These methods will also be the subject of further exploration in this study.

The critical calculations of evaporation are limited largely in part to accurate representation of the evolution of the drop size distribution and are complicated processes to resolve numerically (Seifert 2008). Finding correlations in DSDs has implications for many different parameters in meteorology. The difficulty in modeling these correlations is due to many feedback mechanisms with microphysical processes like evaporation. Water vapor released from an evolving DSD into its regulating environment will increase the relative humidity of that column and thus effect the rate of change of the DSD. Further feedbacks include latent heat exchange where vertical motions of the air control the time drops are suspended in that column. Evaporation creates a downward motion of

cooler air, and subsequently decreases the residence time. This results in decreasing evaporation rates and a decrease in the latent heat exchange. Other contributing factors are coalescence between the cloud base and the surface, drop sorting due to horizontal wind shear, and many other environmental factors.

The exponential drop distribution modeled by Marshall and Palmer (1948):

$$N(D) = N_0 \exp(-\Lambda D) \quad (1)$$

is a well-recognized method of modeling DSDs, where N(D) is the drop concentration as a function of drop size, N_0 is the concentration of drops, Λ is the slope parameter of the drop size distribution and D is the drop size. This was one of the first attempts to model drop size to concentration distributions and was formulated from counting drops on dyed filter papers for the purpose of correlation with radar echoes. This method was then modified by Ulbrich (1983) to include a unitless scaling parameter μ to better correspond to changes in the distribution representing a Gamma relationship:

$$N(D) = N_t D^{\mu} \exp(-\Lambda D) \quad (2)$$

This distribution follows the assumption that the number of drops in a volume will follow a Poisson distribution, and that the diameters of those drops are determined from a gamma distribution. The need for a shaping parameter of the DSD from a practical perspective was highlighted by Fox (2004) in a study looking at the impacts of DSD on soil erosion. Fox (2004) showed that the exponential model puts too much weight on the larger drops resulting in an over estimation of soil erosion as larger drops have higher kinetic energy (KE), displacing soil at a higher rate. However, research into the correlation of the Λ and the μ variables has been called into question with developments

of more advanced observing disdrometers (Moisseev and Chandrasekar 2007). Thus, arises the need for further research into other drop size distribution modeling. In the DSD analysis and modeling of this paper, parameters of DSD such as KE, rain rate (RR), liquid water content (LWC) and reflectivity (Z) will be examined using Gamma and the new aforementioned Gaussian distribution.

Other attempts have been made in the past to more accurately model rain distributions. As rain falls from the cloud base, spontaneous fragmentation and collisions can change the distribution of rain drop sizes, limiting rain drop growth. These interactions do not occur uniformly for all concentrations of drop sizes, time or special scales and can look different from storm to storm. In attempting to parameterize the evolution of the rain drop spectra to account for this discretion, a statistical method was developed called the method of moments (Ulbrich 1983); (Feingold et al. 1988). Ulbrich (1983) showed that by changing the μ parameter, calculations of rainfall intensity can be more accurately calculated. These methods will be explored further in this paper.

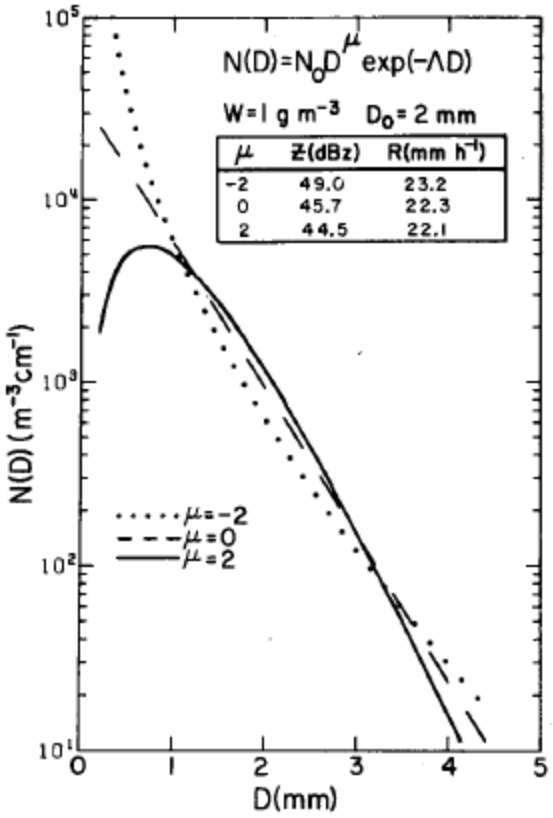

Figure 1 - The shaping parameter μ changes the shape of the DSD described by the method of moments, and how that change effects rain rates and reflectivity for a single drop size D_0 (2 mm) while still generating the same observable LWC (W =g m^{-3}). Taken from Ulbrich (1983).

Serio et al. (2019) looked at several other DSD models proposed in past studies through quantification of KE. The lognormal distribution (LN), Weibull (W), Exponential (MP) and Gamma (U) are the most notable. This review of a lognormal distribution cites several studies (Levin 1971; Bradley and Stow 1977; Markowitz and Markowitz 1976; Feingold and Levin 1986; Willis and Tattelman 1989; Ochou et al. 2007) claiming this method is preferred for DSD calculations due to the simple geometric interpretation of its parameters as well as easily interpreted moments. Best (1950), Weibull (1951), Wilks (1989) and Alonge and Afullo (2012) describes rain distribution

formation as a chain reaction where drops grow until turbulence and collisions changes the distribution modeled by the Weibull distribution.

In this study, a new method using a Gaussian distribution to represent DSD will be proposed and examined comparing parameters such as KE, RR, Z and LWC to the Gamma distribution traditionally used. The Gaussian distribution will also be used in the evaporation equation, with the results compared to that of the traditionally examined Gamma distribution.

Correctly modeling drop size distributions is limited by the ability to observed drops in the atmosphere (Kostinski and Jameson 1997) and at the surface (Löffler-Mang and Joss 2000). A study by Gunn and Kinzer (1948) was a forerunner in determining methods of observing varying rain drop sizes at the surface.

$$V(D) = 49 * \left(\frac{D}{10}\right) * e^{-2*(\frac{D}{10})} \quad (3)$$

Equation 3 is the interpreted formula of the Gunn and Kinzer model relating drop size D (mm) to terminal velocity V(D) (m s^{-1}). By assuming that drops would reach terminal velocity, raindrop sizes would exhibit different downward velocities as a function of its size due to the frictional drag. Others followed on to this work modifying the Gunn and Kinzer formula.

$$V(D) = 3.778 * D^{0.67} \quad (4)$$

$$V(D) = 9.43 * (1 - e^{-0.5195*D^{1.147}}) \quad (5)$$

Equation 4 shows the Atlas and Ulbrich (1976) and Equation 5 shows the Ferro (2001) calculation.

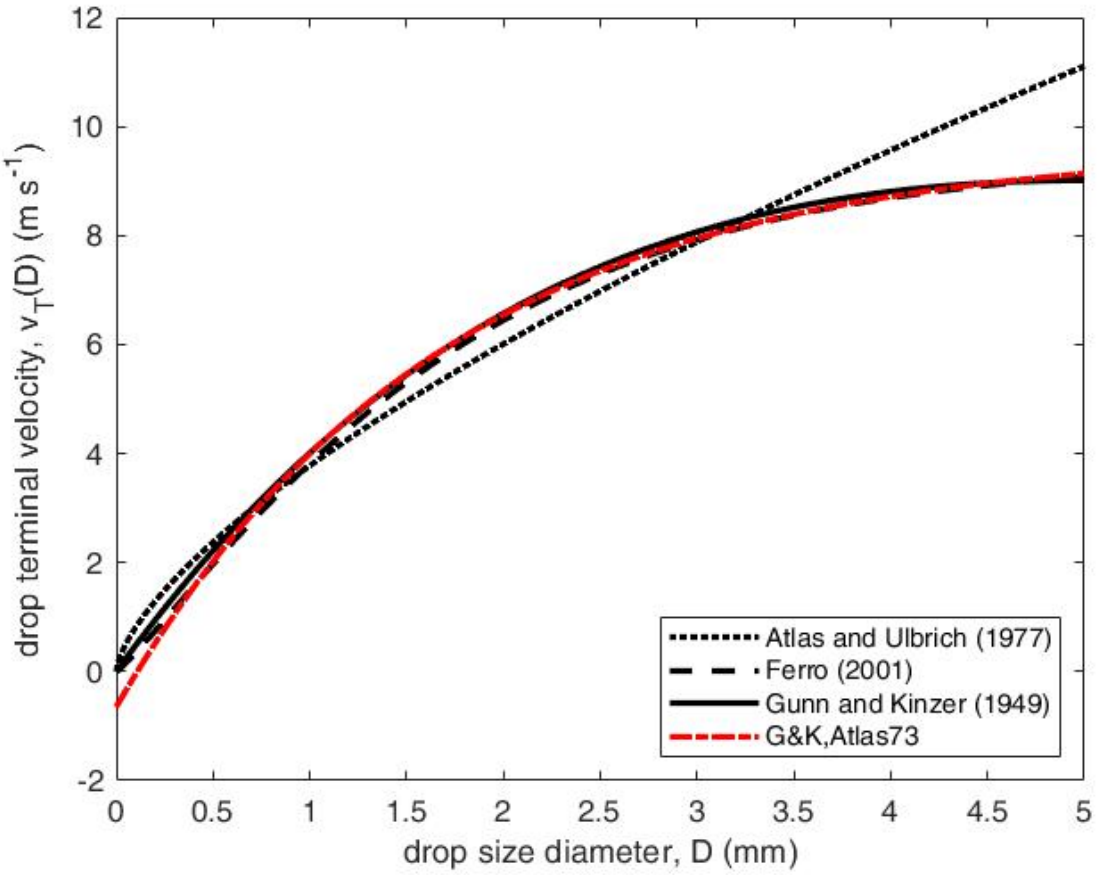

Figure 2 – A comparative look at fall velocity calculation theories based on diameter size.

Figure 2 reveals how theoretical fall velocities for drop sizes compare to one another. The fall velocity used in modeling DSD will be the Ferro (2001) (Equation 5) calculation for surface-observed fall velocities. This calculation most closely matches the MRR calculation software which includes a height parameter ($\delta v(h)$), to account for the change in air density with height.

$$V(D) = (9.65 - 10.3 * e^{-0.6*D})\delta v(h) \qquad (6)$$

Serio et al. (2019) used laser disdrometers to compare the DSD's of a volume of air using fall velocities. Similar methods will be applied in this study.

1.2 Goals

Given evaporation is a complicated process to model, and DSD's are a key component in that calculation, the following challenges will need to be addressed:

- Evaluate drop distributions through a multitude of rain intensities and formation processes through a laser disdrometer and attempt to model those distributions through machine learning methods.
- Assess the Micro Rain Radar (MRR) data and correctly match and model drop distributions observed with the laser disdrometer.
- Deploy radiosondes to develop case study data collecting real atmospheric conditions to use to compare to modeled atmospheric conditions.
- Extract the atmospheric induced vertical velocity of balloon launches and compare to model derived velocities on the evaporation intensity.
- Gauge the evaporation rates of different DSD schemes through modeled and real time atmospheric conditions.
- Assess the accuracy of methods and determine other influences that may need to be resolved in order to better model evaporation in the atmosphere.

With a multitude of tools available, the objective is to observe as completely as possible how drop distributions evolve through the atmosphere. In doing so, evaporation may be understood and modeled to solve numerous issues in forecasting error. Following the methods outlined from the previous bodies of work and creating new processes in this research, it is the expectation that the data presented will drive further exploration into understanding the nature of the atmosphere.

2. Methodology

2.1 The Evaporation Model

To determine evaporation in the atmosphere, measurable parameters must be identified that fully represent the change in the atmospheric water volume. This can be most thoroughly accomplished by evaluating the total change in liquid water content (LWC) through the change in drop diameter (Bongard 2019) . The loss of LWC can be directly related to evaporation in the lower levels of the atmosphere by quantifying the parameters controlling the change in mass of a single drop (Kinzer and Gunn 1951), and then summing the total change of the DSD from layer to layer throughout the column below the cloud base.

To begin building the evaporation model, it is necessary to first parameterize the atmosphere. For this research, the area of interest is below the cloud-base. The saturation vapor pressure (e_s) is an atmospheric parameter used in measuring the rate at which water molecules can escape a droplet of water, a process defined as diffusion. It is given by the equation:

$$e_s = 6.11 * e^{\frac{17.67*\bar{T}}{243.5+\bar{T}}} \tag{7}$$

where e_s is in hPa, $\bar{T}$ is the mean low-level temperature in Celsius taken from a defined layer of the atmosphere. An equation for the diffusion coefficient is then determined by other observable atmospheric parameters:

$$d = \left(\frac{D_0 * P_0}{\bar{P}}\right) * \left(\frac{\bar{T}}{T_0}\right)^{1.94} \tag{8}$$

where d is the diffusion coefficient in $m^2 s^{-1}$. D_0 is the constant diffusion coefficient $2.11*10^{-5}$ m^2 s^{-1}, P_0 is the standard sea level pressure constant, 1013 hPa, $\bar{P}$ is the average layer pressure in hPa, $\bar{T}$ is the average low-level temperature in Kelvin (K) and T_0 is the standard temperature of 273K. Equation 7 and equation 8 can then be combined to get a standard atmospheric water vapor diffusion term:

$$F_D = \left(\frac{\rho * R_v * \bar{T}}{d * e_s}\right) \tag{9}$$

where ρ is the density of water of 1000 kg m^{-3} and R_v is the gas constant for water vapor at 461.5 J kg^{-1} K^{-1}.

Another factor of quantification for the atmospheric condition is the flux of energy from evaporation and condensation. This is given by the equation:

$$F_K = \left(\frac{L}{R_v * \bar{T}} - 1\right) * \left(\frac{L * \rho}{k * \bar{T}}\right) \tag{10}$$

where F_K is the heat conduction term given by L, the latent heat of vaporization $2.26*10^6$ J kg^{-1}, and the thermal heat conduction term k in W m^{-1} K. This parameter will play a role in regulating energy flux due to evaporating water throughout the atmospheric column below the cloud base.

Factoring in residence time and considering air motions around a single drop, and how those air motions change from drop to drop depending on its size, are some of the more challenging quantifications for this research. This is the ventilation coefficient and is defined as:

$$F_v = 0.78 + 0.308 * \left(\frac{v}{d}\right)^{\frac{1}{3}} * \left(\frac{V_T * D}{v}\right)^{1/2} \tag{11}$$

where v is the kinematic viscosity of air and D is a raindrop's diameter in mm. The V_T parameter is representing the terminal velocity in meters per second (m s^{-1}). In the evaporation model, the Kinzer and Gunn (1951) equation (G&K) was used to quantify the V_T parameter as this is the most cited velocity model for evaporation. The G&K equation is very similar to Equations 3, 4, 5 and 6 with select modifications to account for the vertical motions below the cloud base:

$$V_t = 9.65 * \left(1 - e^{-.53*\left(\frac{D}{10}\right)}\right) - w \tag{12}$$

where D is the drop diameter in mm and w is the vertical wind speed in m s^{-1} relative to the surface. Determining the value of w will be discussed more in section 2.5 in the methodology.

The last step in the evaporation model is to quantify the changing DSD's through the lower layers of the atmosphere below the cloud base. By determining the diameter change for each drop in a layer over the height of each layer, a total quantification can be made. The model of diameter evaporation used in this study comes from Rogers and Yau (1996):

$$D_e(h+1) = (F_v * \frac{\frac{\Delta h}{V_{t(D)}}}{1000} * \frac{4S}{F_k + F_D} * D_h) + D_h) \tag{13}$$

where D_e is the change in diameter as a function of height due to evaporation in mm, F_v (eqn. 11) is the ventilation coefficient, h is the layer height, V_t (Equation 12) is the terminal velocity, S is the average saturation computed by the relative humidity (RH) for the that layer, F_k is the heat conduction term (Equation 10) and F_D is the water vapor diffusion term (Equation 9).

To demonstrate the functionality of the model, a theoretical dry layer can be displayed using a model driven thermodynamic profile. Varying drop sizes can be input into the model to see the response to the evaporation in diameter change over the height of the column given the model parameters. An analysis of using modeled sounding data will be conducted in this research.

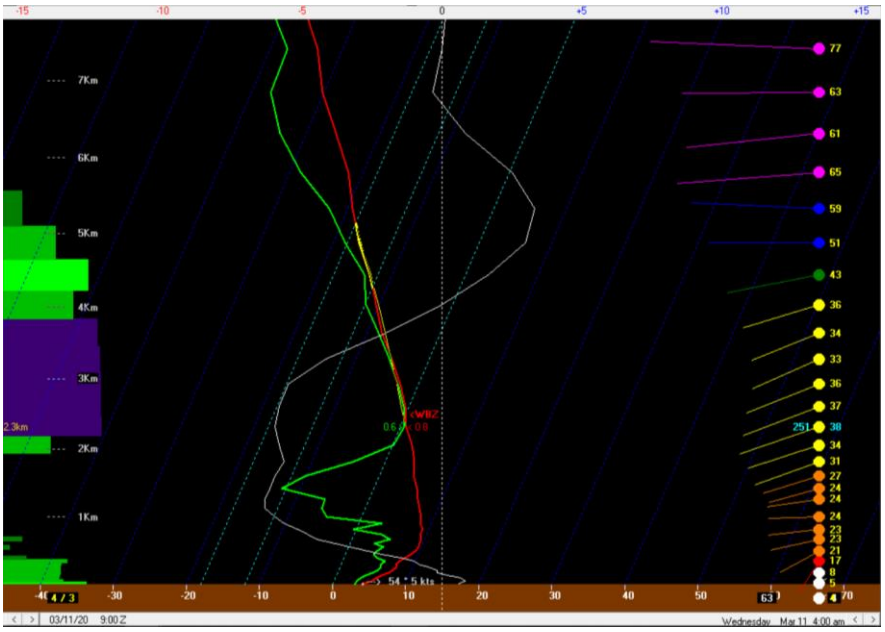

Figure 3 – A model derived atmospheric dry layer from the 12Z NAM forecast model from Columbia, MO on March 11th at 09Z. The red line displays the temperature profile (°C) with height, the green line represents the dewpoint profile (°C) and the white line shows the omega (vertical motion) in pascals per second Pa s^{-1}. The left side of the graph displays the Relative Humidity (RH%) at a specific level in kilometers (km) where green is >70% and purple is >90%.

Choosing the appropriate height is important for the model to work properly. Melting and sublimation are not parameterized in the evaporation calculation but should be subject to future study. For the example case of the model profile sounding in Figure 3, and future cases, cloud bases are considered to be at the 90% RH threshold, signified by the purple highlighted areas over the height to the left of the profile. In Bongard

(2019), the layer considered the cloud base is the lifted condensation level (LCL). Taking into consideration that cloud bases may be above or below this level, such as the case in Figure 3 where the LCL is near the surface, the method of distinguishing cloud bases at >90% RH was used as the determining factor. Using heights above the cloud base, as pointed out by Pallardy and Fox (2018), would not dramatically change the evaporation quantification considering that in-cloud is a saturated environment, precluding any significant evaporation to occur. However, such as in the case of Figure 3, the melting layer is only slightly above the cloud base and would affect the model's calculations of evaporation. It is important to capture the full area of the dry layer to accurately account for total evaporation. This is covered in further detail in section 2.4.

As shown in Equation 12, the vertical motion of the atmosphere has an impact in the evaporation quantification. Model guidance gives vertical motion values in the pressure coordinates of ω (Pa s^{-1}). This requires a conversion as the evaporation model uses vertical motions in Cartesian coordinates w (m s^{-1}). The following transformation was used:

$$w(P,T) = -\frac{\omega * 100}{(\frac{P}{R*T} * g)} \tag{14}$$

where w is the vertical motion in Cartesian coordinates in m s^{-1} as a function of the pressure and temperature, ω is vertical motion in pressure coordinates and is in Pa s^{-1} , P is the atmospheric pressure in hPa at a specific height, R is the gas constant 287 J kg^{-1} K^{-1} , T is the temperature in K and g is the acceleration of gravity m s^{-2}. Figure 3 displays the vertical motions of w at the center of the display as the 0-line depicted by a dashed white line and the measurement as a solid white line. A scale is present at the top of the profile

to show the magnitude of the vertical motion in Pa s^{-1}. The red negative values on the scale represent upward vertical motions and the blue positive numbers represent downward motions.

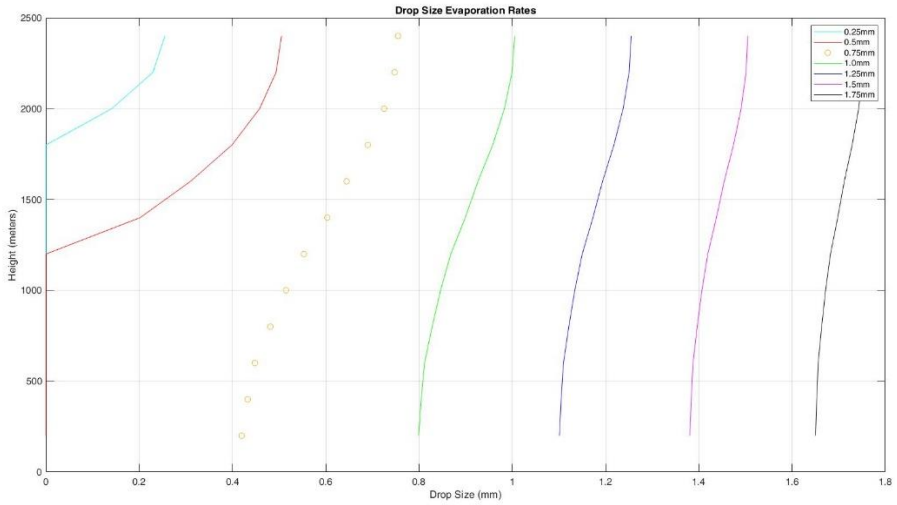

Figure 4 – Example of how the model evaporation rates of single raindrops given the environment of Figure 3. The Y-axis is the height in meters. The X-axis is the drop size in mm.

In Figure 4, the extinction rate decreases as the drop size increases. This is a result of the evaporation rate being faster for the smaller drops than the bigger drops. There are several reasons for this. The first is that the residence time is longer for smaller drops. Since air resistance is a buoyant force, smaller, lighter drops will fall slower than larger drops increasing the residence time, or time spent in the dry layer. Residence time is directly proportional to evaporation in the dry layer. The second factor is a result of the surface tension of a droplet. Larger drops have greater surface tension dispelling water vapor at a slower rate than smaller drops. The smaller drops have a greater surface curvature so due to the Kelvin effect, require a higher vapor pressure to maintain size and drop growth. Dry air inherently has lower vapor pressure than that around a droplet. This

allows water vapor molecules to escape the drop when not in a super-saturated environment and is exacerbated with higher curvature (smaller diameter). This is directly proportional to higher evaporation rates. Figure 4 shows 0.25 mm and 0.5 mm droplets evaporating completely before reaching the surface. Furthermore, the 0.5 mm drop undergoes complete extinction roughly 1000 m lower than the 0.25 mm drop. When comparing 0.75 mm to 1.0 mm, the 0.75 mm loses nearly 0.35 mm of diameter before reaching the surface, while the 1.0 mm drop only loses roughly 0.2 mm of diameter.

By knowing how much a single drop diameter changes, one can calculate the total mass change in LWC of a single drop:

$$\Delta LWC = \rho * \frac{\pi}{6} * \Delta D \qquad (15)$$

Considering there are hundreds to thousands of droplets that vary in size over a single observational minute, an accurate way to quantify DSD's is needed to run in the model. In order to display accurate distributions, they must first be modeled correctly. Correctly modeling DSD's as well as determining if the model truly represents the real atmosphere requires precise measurements from specialized instrumentation.

2.2 The Laser Disdrometer

Quantifying evaporation relies heavily on being able to accurately observe the DSD at the initial, developing and final conditions as they evolve beneath the cloud base. While placing a disdrometer at the base of a cloud is virtually impossible, disdrometers at the surface have been a reliable method of observing the final state of the DSD evolution. The progression of DSD observations has improved with advancing technology (Tokay et al. 2001). From Marshall and Palmer (1948) method of counting and measuring DSD on

filter paper, to the latest technology using laser disdrometers (used in this study), advancement in the field continues to orchestrate the progress of research.

The laser disdrometer used in this study is the OTT Parsivel^2 Laser Weather Sensor (Figure 5). This laser disdrometer emits a laser through a laser diode at a wavelength of 650 nm and has a peak power output of 0.2 mW. The receiver is an optical sensor located 180 mm from the laser output. The total measuring surface area that precipitation falls through is 54 cm^2. The sensor can detect liquid precipitation from 0.2-8 mm and solid precipitation up to 25 mm as well as fall velocities from 0.2-20 m s^{-1}. The software in the system classifies precipitation in 32 size and 32 velocity classes with an accuracy of ± 1 for size classes below 2 mm and ± 0.5 sizes greater than 2 mm. The laser disdrometer will also observe eight precipitation types including drizzle, drizzle/rain, rain, mixed rain/snow, snow, snow grains, sleet, and hail.

Figure 5 - The instruments used in this study. Located at Bradford Research Farm in Columbia, Missouri, the instrument on the left is the Micro Rain Radar, and the instrument on the right is the OTT Parsivel² laser disdrometer.

This specific disdrometer was chosen to most accurately observe the drop size distribution and develop an accurate DSD model at the surface. A study in Warsaw, Poland used the OTT Parsivel^2 disdrometer to observe rainfall at the temporal resolution of every 10 s to examine varying DSD sets and the associated rain rates and reflectivity values (Licznar and Krajewski 2016). With this data Licznar and Krajewski (2016) were able to conclude that Z-R relationships to DSD were well represented and modeled in Warsaw's climate. However, they also showed discrepancies in the Z-R relationship with frozen precipitation types like sleet, snow and hail, calling for an introduction of hail and snow specific Z-R relationships in Poland.

There are some potential drawbacks and inaccuracies to the OTT Parsivel^2 and laser disdrometers. Any two or more drops falling through the plane of the observing window at the exact same time sufficiently close together may be recorded as a single drop. However, this resolution of two drops into one may be discarded if the size to fall velocity is outside of the G&K classification curve. Figure 6 shows the G&K curve over real time observations of distributions with the drop diameter as function of fall velocities noted by Equation 3.

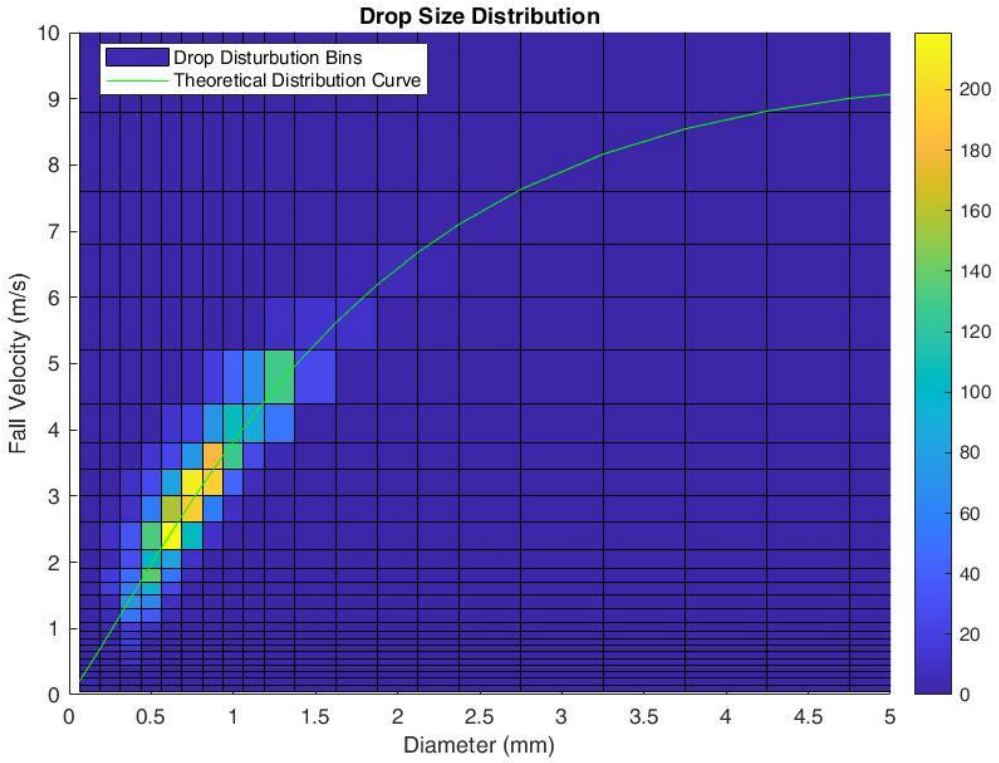

Figure 6 - Measurement from the disdrometer taken on August 30th, 2019 at 1900Z. This shows a 1-minute averaged observation from the number of drops counted in each bin of the diameter in millimeters (mm) and fall velocity in meters per second (m s^{-1}).

Splash back and simultaneous drop measurements would be counted in bins outside of the distribution curve as they would not express the appropriate velocity to diameter and can be discarded as erroneous if the falling precipitation is assumed to be rain. This method also contributes to precipitation type identification, where snow, mist and other hydrometeors have different velocity to diameter profiles.

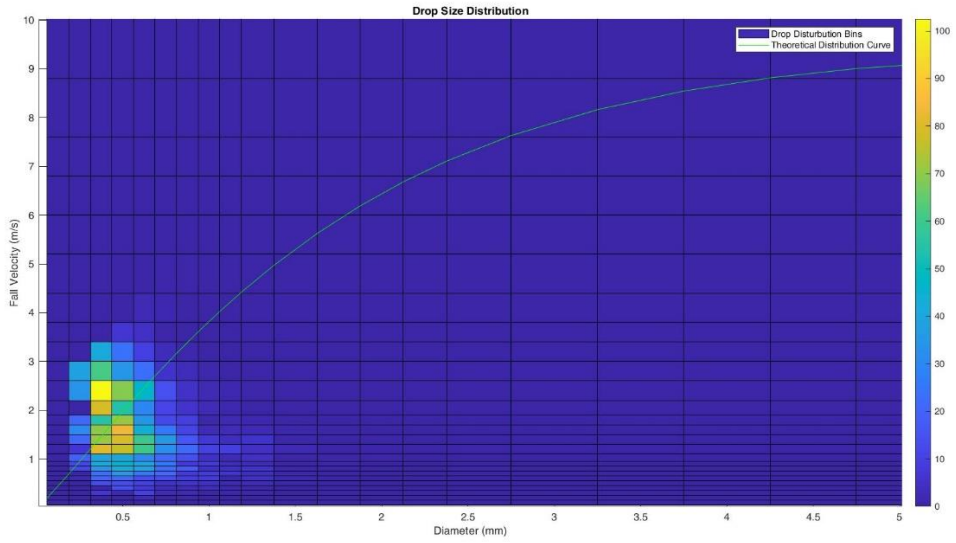

Figure 7 – Observation converted to a DSD with the G&K line plotted taken from the laser disdrometer on January 11th ,2020 at 23Z displaying the velocity to drop diameter expression of snow and mist.

Figure 7 shows how a drop distribution would look under snow and mist conditions. Many of the observed hydrometeors are concentrated under low fall velocities and diameters at or under 0.5 mm. This is consistent with mist. Some slightly elevated concentrations can be seen extending to 1.5 mm in diameter well under the G&K curve, which is consistent with snow. This corresponds with snow and mist observations taken from the Columbia Regional Airport automated surface observing system (ASOS) 8.5 km south of Bradford Research Center (**METAR KCOU 112254Z 33007KT 2SM -SN BR FEW018 OVC030 M04/M06 A2999 RMK AO2 SLP163 P0002 T10391056=**). Observations taken from this ASOS were used to verify the height of the cloud bases and precipitation types for cases in this study.

Another potential drawback with the laser disdrometer is in the method of counting the drop distributions in the 32x32 bins. This method is used to account for the innumerable range of sizes that drops may possibly exhibit. Table 1 shows the drop sizes,

corresponding bin-widths and velocities for the 32 bins. The purpose of the bin-widths is to adjust the area where drops are being observed for a smoother distribution.

Dropsize (mm)	0.062	0.187	0.312	0.437	0.562	0.687	0.812	0.937
Binwidth (mm)	0.125	0.125	0.125	0.125	0.125	0.125	0.125	0.125
Velocity (m/s)	0.05	0.15	0.25	0.35	0.45	0.55	0.65	0.75
Dropsize (mm)	1.062	1.187	1.375	1.625	1.875	2.125	2.375	2.75
Binwidth (mm)	0.125	0.125	0.25	0.25	0.25	0.25	0.25	0.5
Velocity (m/s)	0.85	0.95	1.1	1.3	1.5	1.7	1.9	2.2
Dropsize (mm)	3.25	3.75	4.25	4.75	5.5	6.5	7.5	8.5
Binwidth (mm)	0.5	0.5	0.5	0.5	1	1	1	1
Velocity (m/s)	2.6	3	3.4	3.8	4.4	5.2	6	6.8
Dropsize (mm)	9.5	11	13	15	17	19	21.5	24.5
Binwidth (mm)	1	2	2	2	2	2	3	3
Velocity (m/s)	7.6	8.8	10.4	12	13.6	15.2	17.6	20.8

Table 1 - The observational bins the Disdrometer software uses to place each drop in its respective area based on the drop size (mm), bin-width (mm) and the drop velocity (m s^{-1}). The highlighted area display's where we find a potentially erroneous elevated concentration area.

However, the changing bin sizes could be responsible for what could be an erroneous "hump" when observing the drops in between 1.187 mm and 1.375 mm bin. Figure 8 illustrates how this phenomenon presents itself from a drop size to drop concentration perspective and Figure 9 demonstrates a contoured version of Figure 6, highlighting the slight increase in concentrations for that bin.

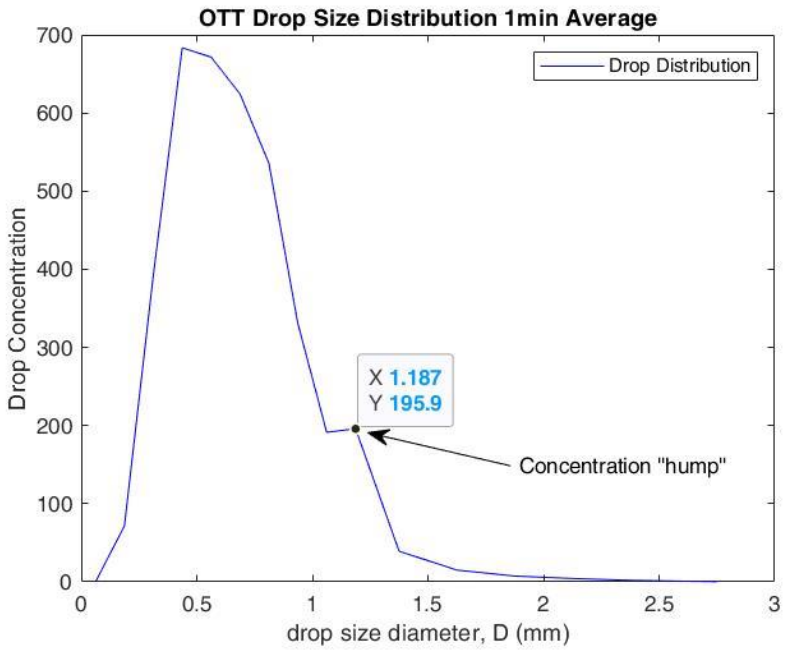

Figure 8 - Concentration "hump" from a drop concentration to drop diameter perspective.

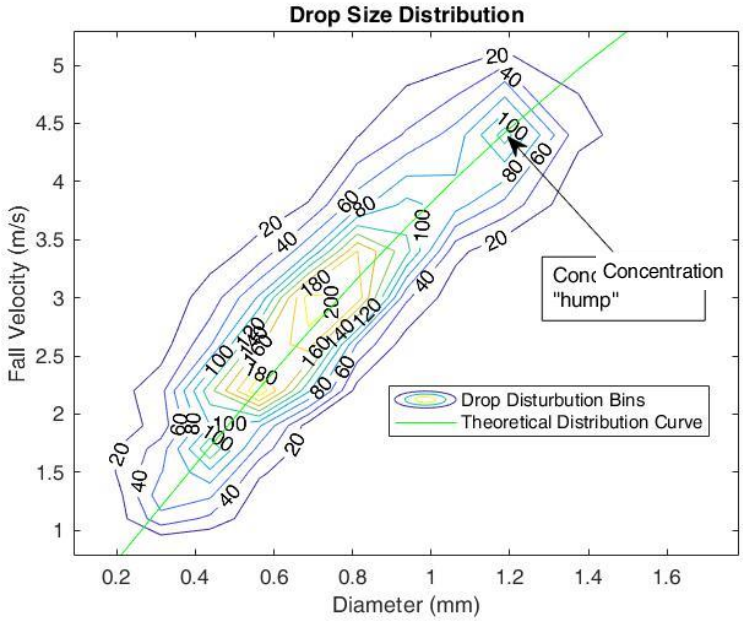

Figure 9 – The DSD in a contoured format where the elevated concentrations are highlighted by the arrow.

This hump presents itself consistently through many different observations. It is not yet clear if this is a natural phenomenon or due to the increase in bin size at that diameter. Further exploration will need to be conducted in order to determine the validity of the phenomenon in future studies. It did not present a significant issue in this study and was largely ignored moving forward.

2.3 The Micro Rain Radar (MRR)

Observations on DSD change with evaporation from the cloud base to the surface is the critical step in modeling the microphysical processes involved. In previous studies, using dual polarization radar and the Z-R relationship was used to make these observations (Moisseev and Chandrasekar 2007; Pallardy and Fox 2018). However, the angled beam height sampling inherent to a Doppler radar can skew the accuracy of this data. By observing the atmosphere vertically, sampling volumes of distributions can be taken at higher temporal and spatial resolutions.

The MRR, shown in Figure 5, is a compact K Band system operating at 24.230 GHz. The system functions by propagating electromagnetic radiation vertically into the atmosphere. A certain portion of this radiation will then scatter back to the receiving antenna once it's reached an object of sufficient size. The power received is determined by how large the scatterer is, with larger objects returning more power to the receiver. In most cases, this will be hydrometeors such as rain and snow. The radar will also observe fall velocities based on the frequency shift between the transmitted and the received signal. This is referred to as Doppler frequency. Given that rain of different sizes falls at different speeds, the Doppler frequency can build a profile of the DSD based on this principle. The observation rate of the MRR is every 10 s providing a much higher

temporal resolution then a traditional horizontal observing radar. With further averaging of the received data, rain rates (mm hr^{-1}) and liquid water content (g m^{-3}) can also be derived from the received signal. The R(Z) relationship the MRR uses is:

$$R = \frac{Z^{0.0707}}{300} \tag{7}$$

where R is the rainfall rate (mm hr^{-1}) and Z is the reflectivity based on the drop concentration distribution from a specific height in decibels (dB).

The MRR software arranges the DSD into 64 spectral bins based on the spectral reflectivity gathered by the receiver. The MRR observes the volume of the atmosphere as 32 gated height layers. The conversion of raw spectral power received by the radar to a drop distribution is calculated at every observable height (gate) and doppler spectrum. The following equation represents how the concentration density is derived:

$$\eta(D,i) = \eta(v,i) * 6.18 * e^{-0.6*D} * \partial v(i * \Delta h) \tag{8}$$

where $\eta(D,i)$ is the spectral density (m^{-1} mm^{-1}) as a function of the 64 drop diameters (D) ranging from 0.109 mm to 6 mm and the 32 height gates (i). $\eta(v,i)$ represents the spectral density as a function of the G&K fall velocity (v) in m s^{-1} given in Equation 6 and the gates (i). The change in v is then a function of the specific gate (i) and the change in height (Δh) in m^{-1}. To calculate the number of drops per volume the following equation is applied:

$$N(D,i) = \frac{\eta(D,i)}{\sigma(D)} \tag{9}$$

where $\sigma(D)$ is the Mie scattering approximation for each drop size. The averaged spectral drop density product from the MRR (Figure 10) shows the averaged drop densities over a

selected time on a logarithmic scale for each drop size bin given by Equation 8. This product allows for a graphical interpretation of changing drop concentrations and will be compared with the modeled evaporation results from a drop concentration perspective.

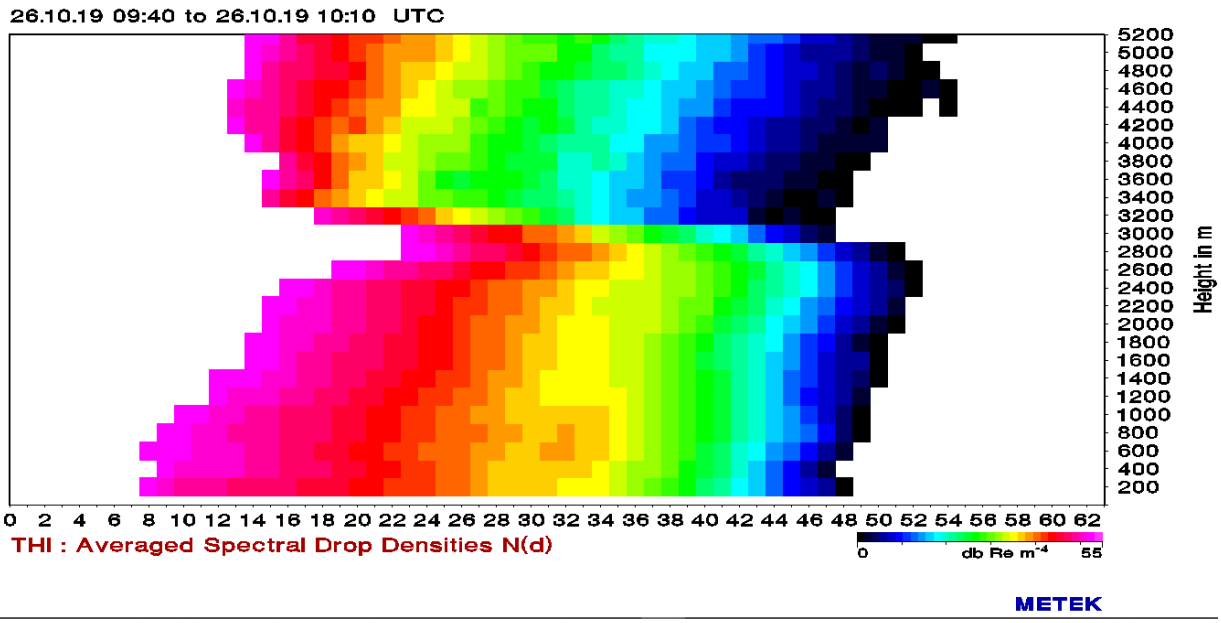

Figure 10 - Taken from Oct 26th, 2019 the 30 minute averaged spectral drop densities shows how the drop concentrations of each drop size bin (x-axis) varies over the height of the atmospheric column (y-axis). The units are in decibels (dB) represented by the color bar in the bottom right corner. The warmer the color the higher the concentration of the hydrometers in its respective size bin where the concentrations are on a 10log(n) scale where n is the drop concentration. In this case, the concentration of smaller drops grows from 2.6km down while the number of larger drops becomes slightly smaller suggesting little evaporation and high drop breakup for this case.

For the purposes of this research, the MRR was set to display 1-minute averaged data. This would be more efficient computationally than 10 second observations, and allow for a larger sampling size. The data being used starts at 200 m above the surface. The location of the MRR necessitates a high base gate because non-hydrological contamination may be an issue at lower levels. Dust particles from nearby farm activity and high bird populations attracted to plant seeds in the area make this necessary to avoid contamination, especially considering a dry lower level environment. Other considerations include setting the observational beam height. The MRR can observe

every 200 m from the surface to 6200 m at 32 gates. The observational height for this study will not typically require observations higher than 600 hPa. The purpose of this study was to observe evaporation below the cloud base, which rarely exceeds 4000 m from the surface climatologically in central Missouri when considering precipitation. Thus, observational heights for this study remain below 4000 m or roughly 600 hPa. Calculations of evaporation were made every 200 m, thus the data collected was set at these height intervals (gates). This was also done for computational efficiency.

One important issue with the MRR, and radar meteorology in general, is attenuation. This occurs when the size of the object being observed exceeds the wavelength being transmitted and blocks any further propagation of the energy to be received. Figure 11 displays how attenuation presents itself in the MRR. There are two areas of note in Figure 11 (top image). Between 1700Z and 1745Z values of 40 dBZ-50 dBZ are depicted through a column from the surface to 2000 m. Above this area, no reflectivity values are displayed. The other area occurs from 1815Z-1900Z where lighter returns between 30 dBZ-40 dBZ are attenuated higher in the column from 2600 m – 4600 m at the base. Figure 12 displays the radar reflectivity corrected for attenuation. The techniques for attenuation correction for the MRR was adopted from Peters et al. (2010). It is important that attenuation is recognized and accounted for in order to get accurate DSDs below the cloud base.

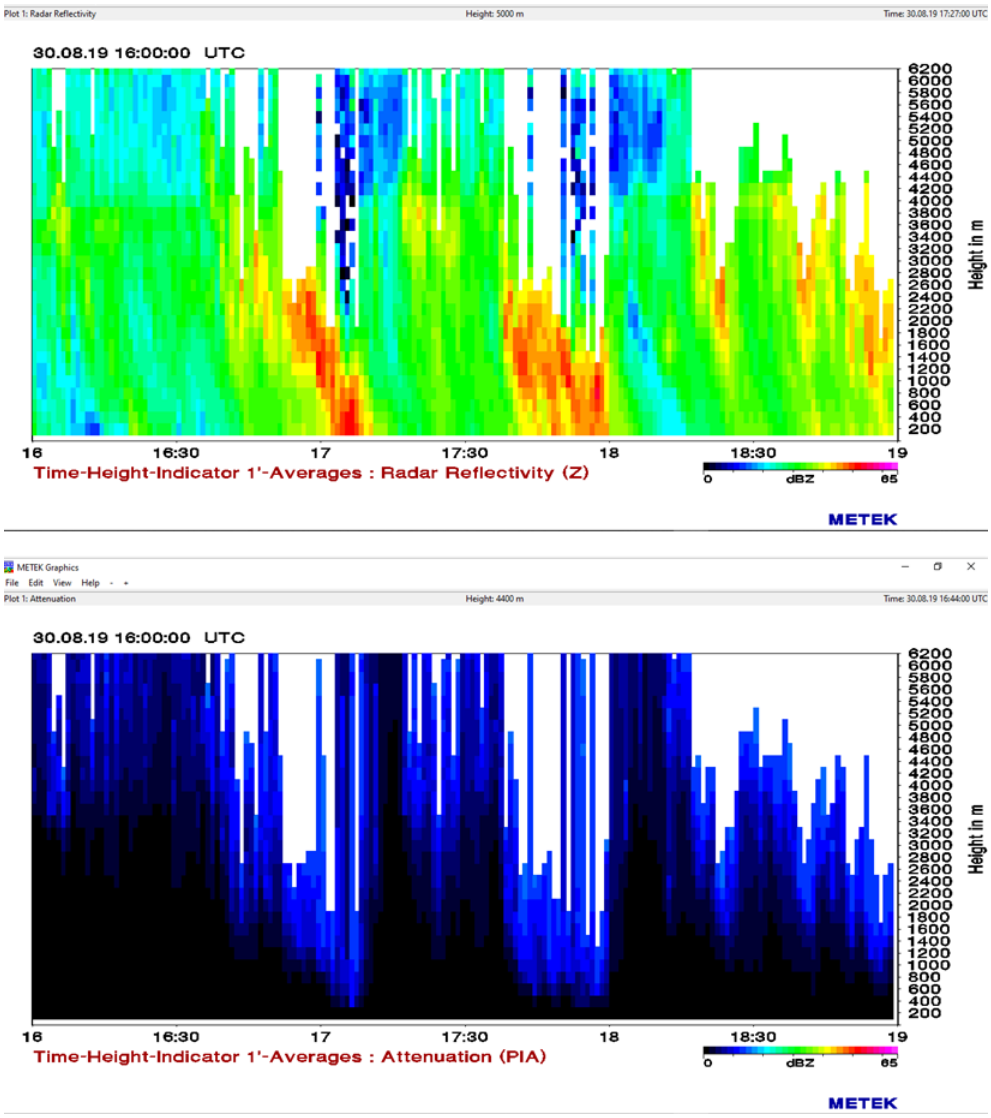

Figure 11 - An example of attenuation taken on August 30th, 2019. Top panel displays Radar reflectivity in decibels (dBZ) from a time-height profile. Bottom panel shows the path-integrated rain attenuation used in the attenuation correction.

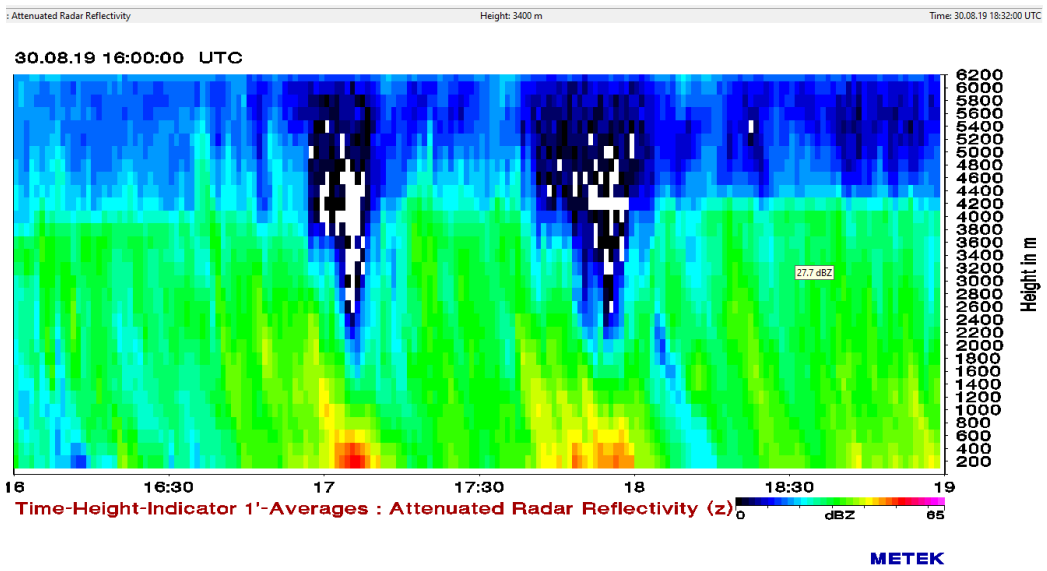

Figure 12 - The MRR correction for attenuation from the August 30th observation shown in Figure 11.

Another important quantification for this study is the height of the melting layer. The evaporation model relies on fall velocities to make calculations (Equation 12). Hydrometeors in the form of solid ice or snow will fall at different rates and skew the quantification. Forecasting the height of the melting layer by looking at thermodynamic profiles (Figure 13) will ensure that when data is collected, all hydrometeors will be in the form of rain below the cloud base.

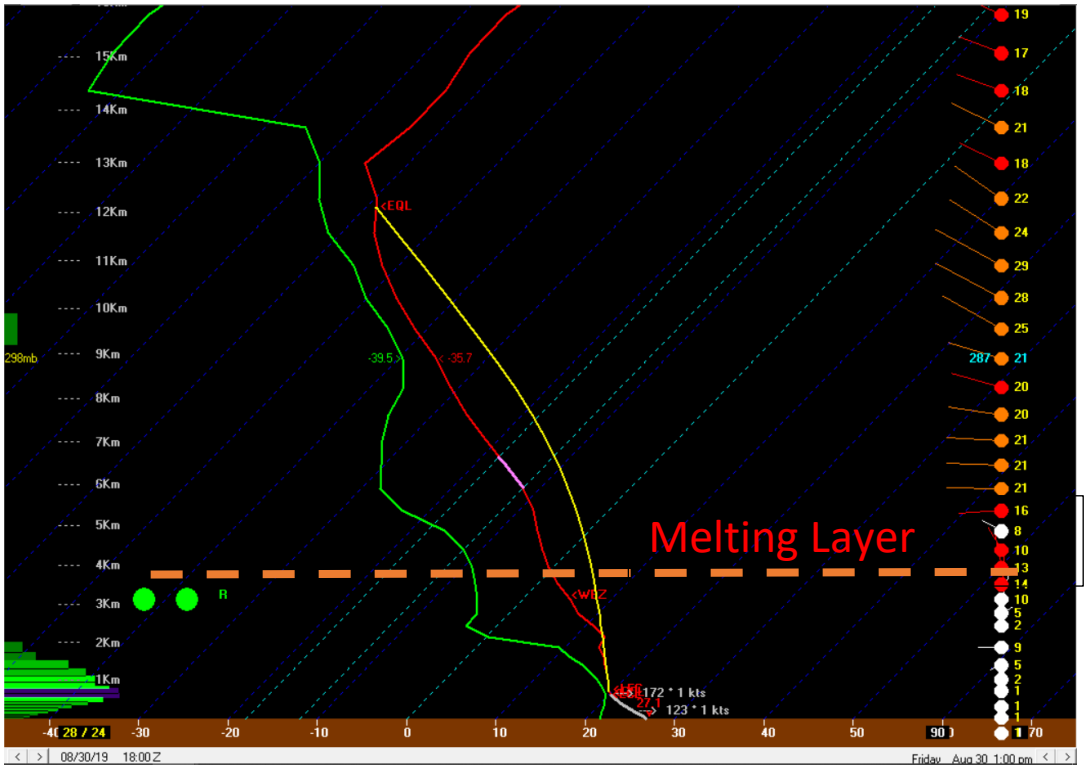

Figure 13 - Forecast sounding from the Aug 26 00Z GFS highlighting the height of the melting layer to determine a viable case study.

Using the MRR fall velocities product (Figure 14) will help determine, after the fact, if the data collected is consistent with hydrometeor type and if the forecast sounding is verifying correctly for melting layer height.

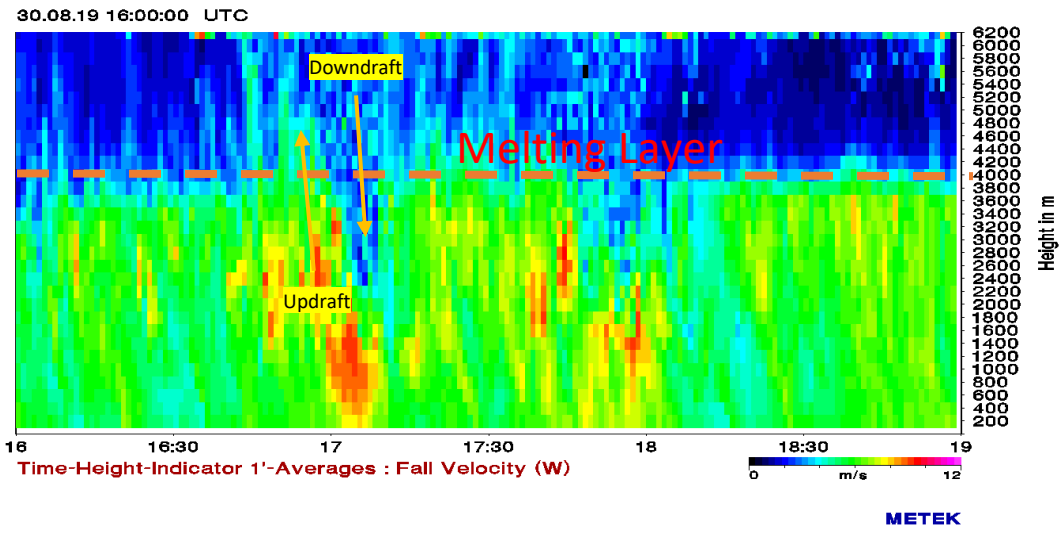

Figure 14 - 3-hour time height profile of MRR derived fall velocities. The melting layer is highlighted where velocities increase with height, indicative of a switch from frozen to liquid precipitation. The melting layer averages at 4km consistent with the forecast sounding data. Updrafts and downdrafts can be observed with faster averaged velocities extending up past the melting layer, and slower velocities extending downward.

When comparing the Figure 13 forecast GFS sounding to the MRR fall velocity data in Figure 14, we can also determine that the model verified well with the real time data given a melting layer at 4km on both products, allowing for conditionally accurate evaporation testing.

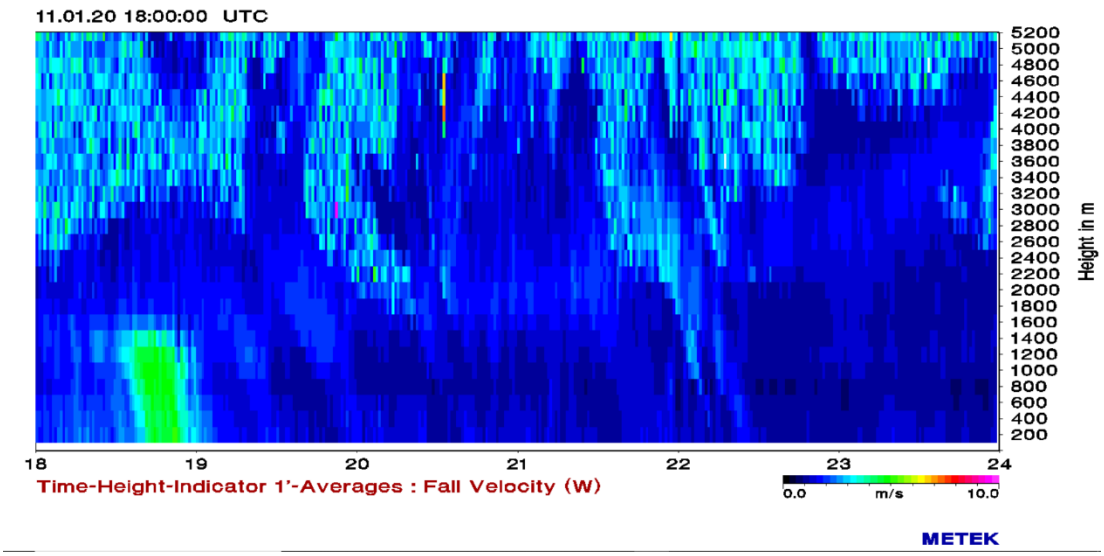

Figure 15 – A snow profile on January 11th, 2019 from a fall velocity perspective. The velocities observed are consistently under 2 m s^{-1}. Using the MRR 's velocity product will help to identify precipitation type for this study.

Another important observation from the MRR fall velocity product is strong convection. Strong updrafts and downdrafts can be observed by the MRR with fall velocity data as higher fall velocities extend above the melting layer and lower fall velocities extend below. This is observed at 1700Z in Figure 14 and corresponds with higher reflectivity values seen in Figure 13. Factoring in strong convection with the evaporation model would be essential given that strong updrafts and downdrafts would rapidly change the DSD. It may seem counter intuitive to think of higher fall velocities with the updraft and lower velocities with the downdraft, but at the melting layer, ice crystals are forced down with the downdraft and rain is forced up at the updraft. Although the vertical motions of the updraft/downdraft counteract the mean vertical motion, the resulting data still displays an averaged value over a minute, smoothing the strong response of the updraft/downdraft perturbations into the mean, and mostly resulting in the fall velocity response based on the fall velocities of the hydrometeor type. Increased or decreased residence time and the number of collisions with amplified atmospheric mixing

are some of the factors that significantly alter the DSD. The issue of quantifying how strong convection plays a role with changing DSDs was addressed numerically by including vertical motion values in the calculations, as well as statistically, with the method of moments and linear regression tools. But identifying these regions using the MRR allows assessment of any discrepancies in the data.

2.4 Radiosonde Data

Determining the state of the atmosphere using model sounding data has been the traditional way to calculate evaporation (Pallardy and Fox 2018). However, Bongard (2019) incorporated real sounding data in tandem with the MRR observations in the evaporation model. This allowed for a more accurate assessment of how the evaporation model was performing. This study will take that method a step further in comparing the output for model soundings solutions to real time data from the observation soundings, while also comparing calculations at the surface to the laser disdrometer.

The sounding system used in the case studies presented was the iMET 1 and iMET 2 radiosonde systems. The entire set up for launches consisted of 200 g and 300 g helium balloons, a parachute, de-reeler and the radiosonde. Before being launched, the system locks onto GPS satellites which transmits data back to the computer in text documents, which can then be used for the evaporation analysis. The radiosonde collects a variety of data including pressure in hectopascals (hPa), height in meters (m), temperature and dewpoint in degrees Celsius (°C), wind speed in knots (kts), wind direction in degrees (°) and relative humidity in percentages (%). Also included in this iMET data suite, which was previously unused from Bongard (2019), was the ascension

rate of the balloon. This information was utilized to help theoretically determine real time vertical motions (Section 2.5).

Because launching weather balloons is limited by the resources available, choosing good case study days is pertinent. A team of graduate and undergraduate forecasters was assembled to forecast and launch balloons when conditions were ideal for case studies. These conditions stipulated that a reasonable chance of precipitation (>60%) would occur and that a dry layer with a dewpoint depression (DPD) greater or equal to 8°C was below 700 hPa to maximize the evaporation observation. When these criteria were met over several days, confidence in a good case study would be high and the team would assemble at the launch site 4-5 hours before the onset of precipitation. This would allow time for 3-4 launches to capture the evolving state of the atmosphere as rain entered the area. To avoid contamination with previous launches and to conserve resources, balloons where launched every 1.5 – 2 hours until saturation was achieved. These launches were conducted at the MU South Farm Research Center, 6km west of the location of the MRR (Figure 16).

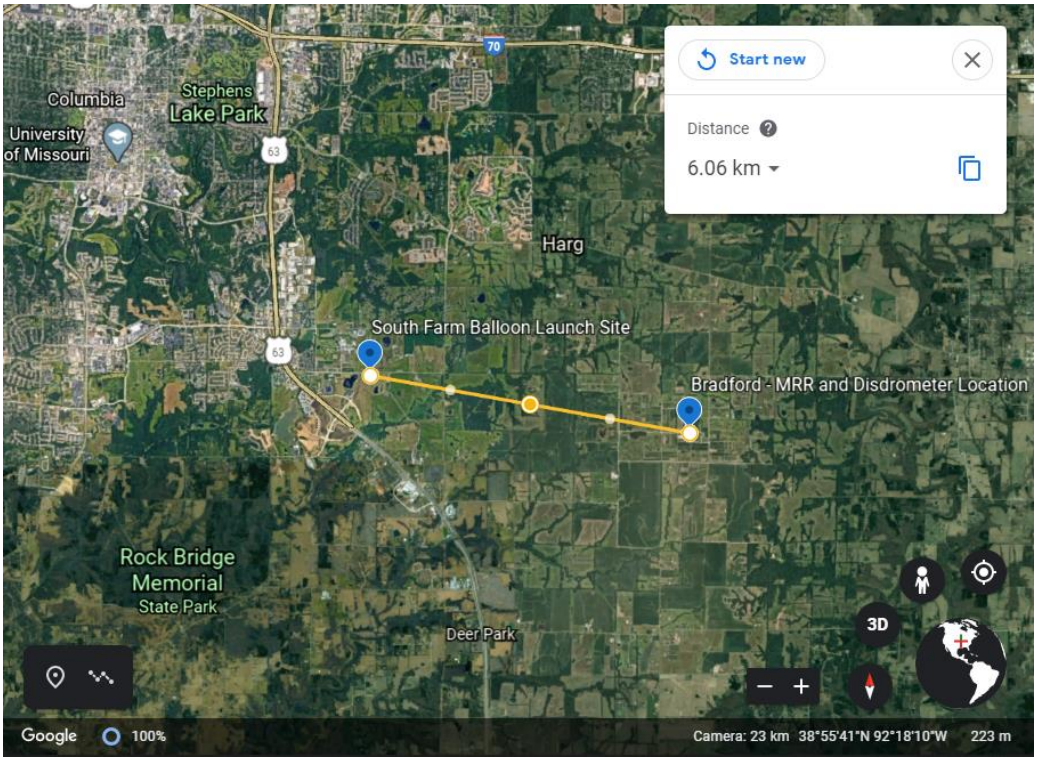

Figure 16 – Satellite image of the observing site and balloon launch site marking the distance linearly between the two points taken from Google Earth.

Although there was some separation in the observation sites, this distance is virtually negligible when considering that weather balloon may travel up to 200 km when transmitting upper air data. In some circumstances, this location may be the best site since common westerly winds drove the balloon toward the radar, capturing the lower atmosphere, which was the main area of interest in this research.

2.5 Finding Vertical Velocities from Balloon Ascension Rates

One of the major hurdles to quantifying evaporation in the atmosphere is observing and modeling vertical motions in the dry layer. Model output resolves this from an omega perspective and can be converted from pressure coordinates to Cartesian coordinates given the pressure and temperature outputs within the model itself (Equation 14). However, this quantification is done over a relatively large grid space compared to

the very fine temporal and spatial resolution of a solitary rainfall column. This can manifest in an averaged omega value that is orders of magnitude smaller compared to what may be observed over a convective or even non-convective rain-shaft. This becomes a crucial issue when trying to determine evaporation rates. Bongard (2019) showed that vertical motions play a very important role in rate of the evaporation quantification.

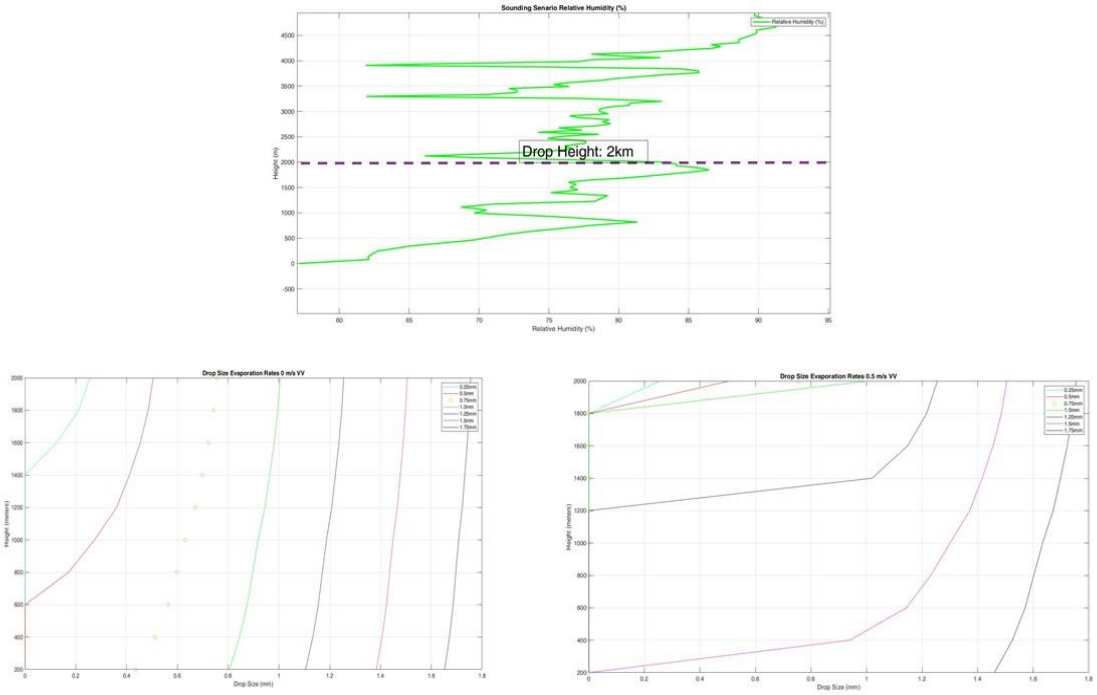

Figure 17 – Two scenarios where raindrop evolution was modeled from 2000 m in relatively dry atmosphere (top). The scenario with 0 m s^{-1} average upward vertical motions (bottom left) shows drops larger than 0.75 mm surviving to below 200 m. Given an atmosphere with an average 0.5 m s^{-1} upward vertical motion (bottom right), only drops larger than 1.75 mm survive below 200 m.

Figure 17 is an example of how important assessing the vertical motion is. An average vertical motion of 0.5 m s^{-1} in a relatively humid profile would eliminate all drops sizes under 1.5 mm in diameter, whereas compared to a 0 m s^{-1} motion, all drops above 0.75 mm survive with all other factors being the same. This would significantly

change an evaporation quantification when considering thousands of drops falling in a single minute.

In the case studies conducted, the radiosonde data included ascension rates on a time scale of 1 per second, unless the data was interrupted, providing a high temporal and spatial resolution for the information received. The height information received from the i-Met data packet is derived from the pressure change as the balloon rises and the GPS position. The derivation of atmospheric vertical motion comes from idea that the ascension of the balloon will remain relatively stable unless acted upon by outside vertical forces. From this idea, the atmosphere is separated into thirty, 200-meter layers and a linear regression is plotted in each layer representing the mean motion of the balloon's rise. The perturbations of the linear regression would then represent the theoretical atmospheric contribution of the vertical motion.

By assessing the adiabatic trends in the vertical profile, direction and the magnitude of the vertical motions observed using this method may resolve some sense of accuracy. These vertical motion profiles can then be compared to the model output of vertical motion to determine if some factored relationship can be assumed, and if certain models have a better vertical motion quantification then others. Given that balloon ascension rates are not readily available in most rain scenarios, using the modeled ascension will be a crucial factor for forecasting evaporation rates. One issue with the vertical motion derivation in balloon ascension is that heavy rain scenarios can significantly alter the calculations if force from falling rain inhibits the balloon ascension. These cases were examined in chapter X.

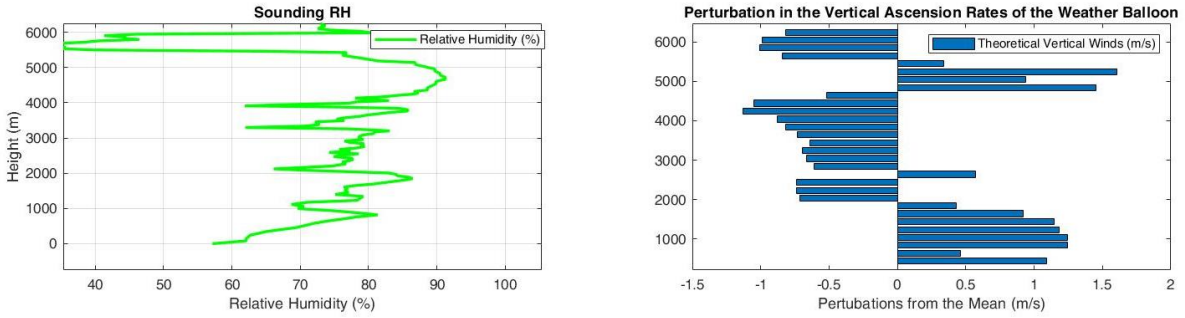

Figure 18 – Comparing the results of the derived vertical motions of the weather balloon (right) to the observed relative humidity (left) on October 5th at 20Z case study.

A close examination in comparing the vertical relative humidity profile to the profile of the perturbations from the mean balloon ascension rate for each layer demonstrates some very promising results. It is expected that as vertical motion upward increases, adiabatic cooling will cause the layer to saturate, increasing the relative humidity of the layer. The opposite is true for downward vertical motion where adiabatic warming occurs and the sinking motion of the air decreases RH in the column. Such is the case for most of the column in Figure 18. From the surface to 2000 m, the perturbations in the mean display upward velocities signifying adiabatic cooling where the column should respond by becoming more saturated. This is exactly the case as the relative humidity rises from 56% to 85% coinciding with an average upward motion of 0.75m s^{-1}. The column then begins to dry from 85% RH at 2000 m to 63% RH at 4000 m following an average downward velocity of -0.65 m s^{-1}. The trend then deviates slightly as the relative humidity dramatically increases at 4000 m, but the upward motion doesn't switch magnitude until 4600 m. The response then becomes more accurate as observed downward perturbations from the mean correspond with a rapid drying to 40% RH above 5500 m associated with a downward motion of -0.75 m s^{-1}.

Additional case studies will need to be evaluated to verify whether this adiabatic trend is consistent with the derived vertical winds. However, the preliminary results are very promising. There is possibility that a relationship can be made with these results equating a magnitude of vertical motion to the adiabatic response. This would be a subject for future study. Derived vertical motions were evaluated in each case study in the next chapter.

When comparing the 12Z NAM model output of vertical motions to the observed rate, the results are not as promising.

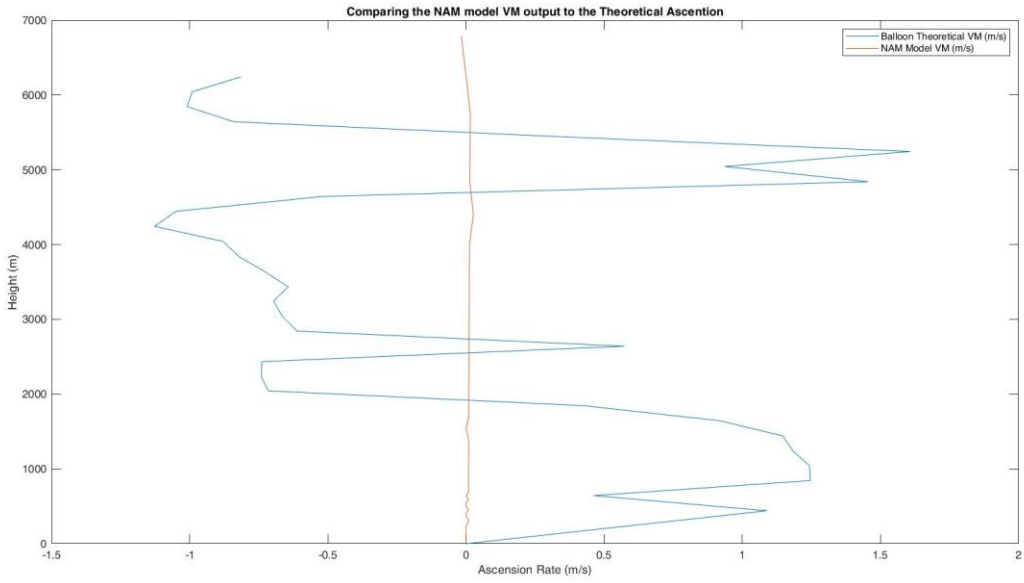

Figure 19 – Comparing the balloon derived vertical motions (blue line) to the 12Z 32 hour NAM model derived vertical motions (red line) on October 5th at 20Z case study.

Figure 19 reveals that there are orders of magnitude difference from the model-derived vertical motions compared to the calculated vertical motions derived from the balloon data.

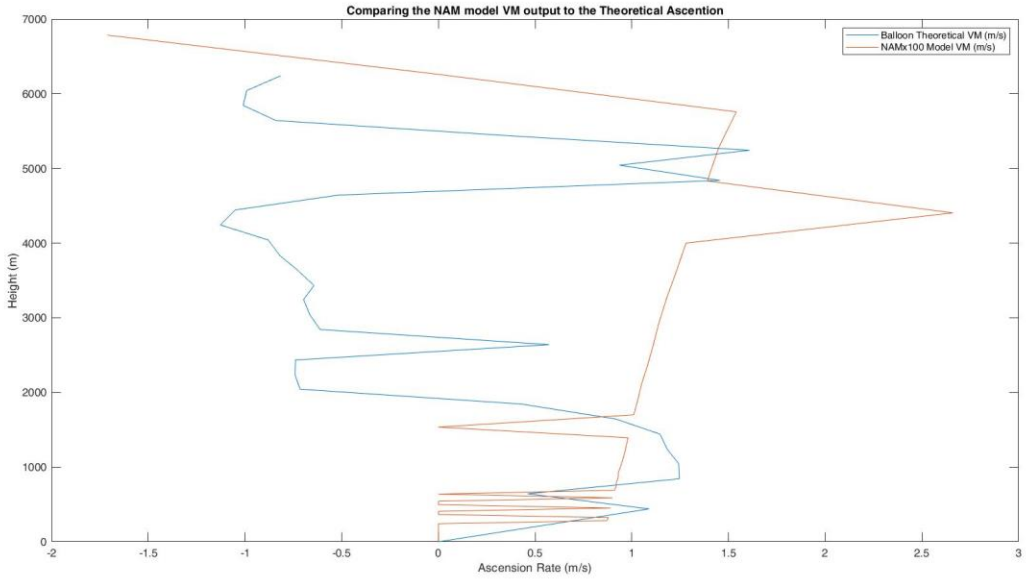

Figure 20 - Comparing the derived vertical wind (blue line) to the 12Z 32 hour NAM model derived vertical wind (red line) magnified by 100 on October 5th at 20Z case study.

By magnifying the model-derived vertical winds by 100, it can also be seen that the overall trend does not correctly match the derived vertical wind profile from the balloon data. But there are a few factors to consider. The model used was taken the day prior and with a coarse temporal and spatial resolution of 1-hour time steps from a 12 km model respectively. This could play a significant role in the accuracy of using model derived motions to put into the evaporation model. These methods were further examined with other model outputs in the case study section of this research.

2.6 Data Management in MATLAB and Data Correction Methods

Once data was collected from the soundings, the MRR and the laser disdrometer, it was processed in the data management program MATLAB. MATLAB provides a desktop environment to perform a multitude of analysis and design processes with a programming language that shows matrix and array mathematics directly. MATLAB code and statistical toolboxes are professionally built, well tested, and fully documented

to allow for a thorough investigation of pre-scripted functions used in this research. With the immense volume of data that was collected during this research, MATLAB made it possible to seamlessly analyze multiple times and areas of interest using iterative functions to decode and apply calculations necessary in the quantification of evaporation.

Data collected from the MRR and the laser disdrometer was averaged over 15-minute intervals in MATLAB. There are several advantages that necessitate this practice. During a balloon launch, the entirety of the dry layer of the environment is typically fully observed within the first 15 minutes of ascents. Thus, the 15-minute average of data is best suited for matching the observational period during the balloon launch to the observed MRR and disdrometer parameters. Furthermore, because fall rates vary with drop sizes, and evaporation can change that dynamic, capturing all the evolving DSDs in this environment through a 15-minute average gives a more complete picture than a one-minute snapshot. This happens as a result of smaller drops inherently falling slower than larger drops, and depending on how dry the environment is, the vertical motions in the atmosphere, the horizontal wind shear causing drop sorting and the height of the cloud base, smaller drops may not be observed in a single minute observation. This can change the quantification of evaporation significantly if not accounted for with a longer average.

Horizontal drift of rain from the cloud base also necessitates a 15-minute data average. The MRR sits at a fixed position observing only what crosses the radars path normal to the surface. This fixed perspective works in the cases where there isn't a significant amount of horizontal speed or directional shear. Such is the case from Figure 21 taken on September 21st, 2019 depicting near vertical columns of reflectivity values and a negligible 1km-5km steering flow of the 12Z NAM 67-hour forecast hodograph

and wind profile from the September 19th, 2019 run[1]. It is worth noting that an assessment of the model's vertical wind shear and the horizontal drift observed by the MRR is another way to verify the accuracy of the forecast soundings.

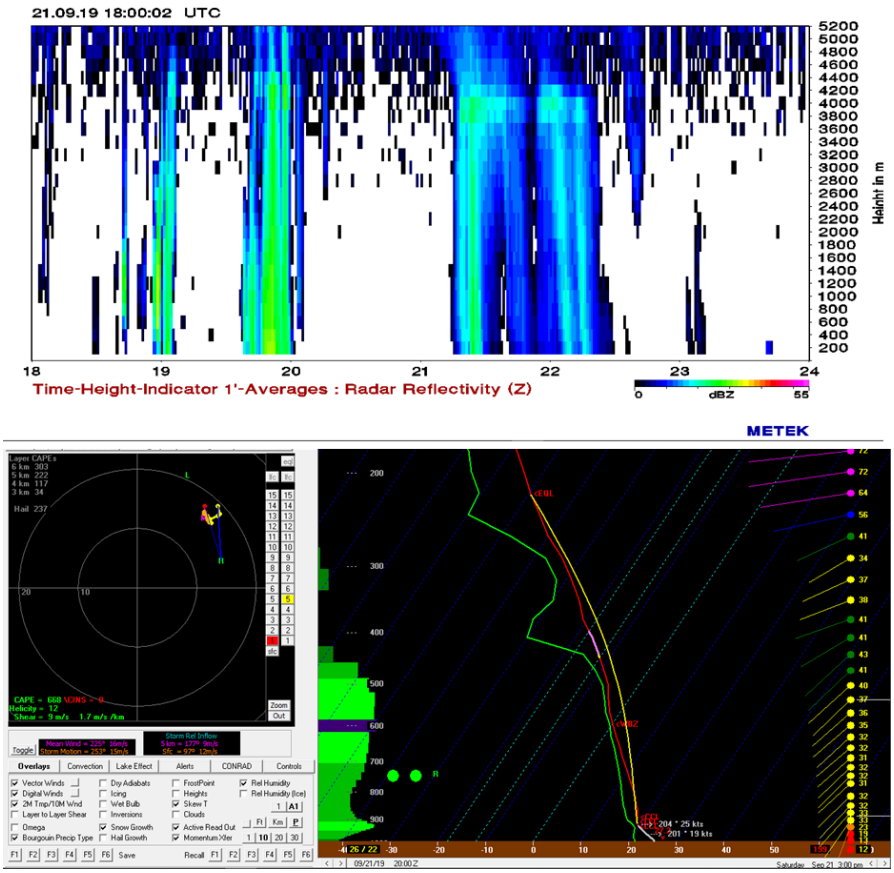

Figure 21 - The MRR image (top) depicts nearly vertical reflectivity values (dBZ) over the 6-hour period consistent with the little speed and directional shear on the 12Z NAM 67hr forecast 1km-5km hodograph and vertical wind depiction (bottom).

However, in cases where the vertical speed and directional wind shear is significant, vertical observations can become skewed, considering the observational method is a time-height profile. It is in these cases that a one-minute average would miss much of the

[1] Model data used is the earliest data available due to data access issues as a result of the global pandemic.

evolving drop distributions in a column significantly hindering the calculation of evaporation. Figure 22 is an example of how wind shear can cause this with relatively small drop sizes depicted by the lower reflectivity values at 25 dBZ and the 0 km-5 km shear at 33 m s^{-1}.

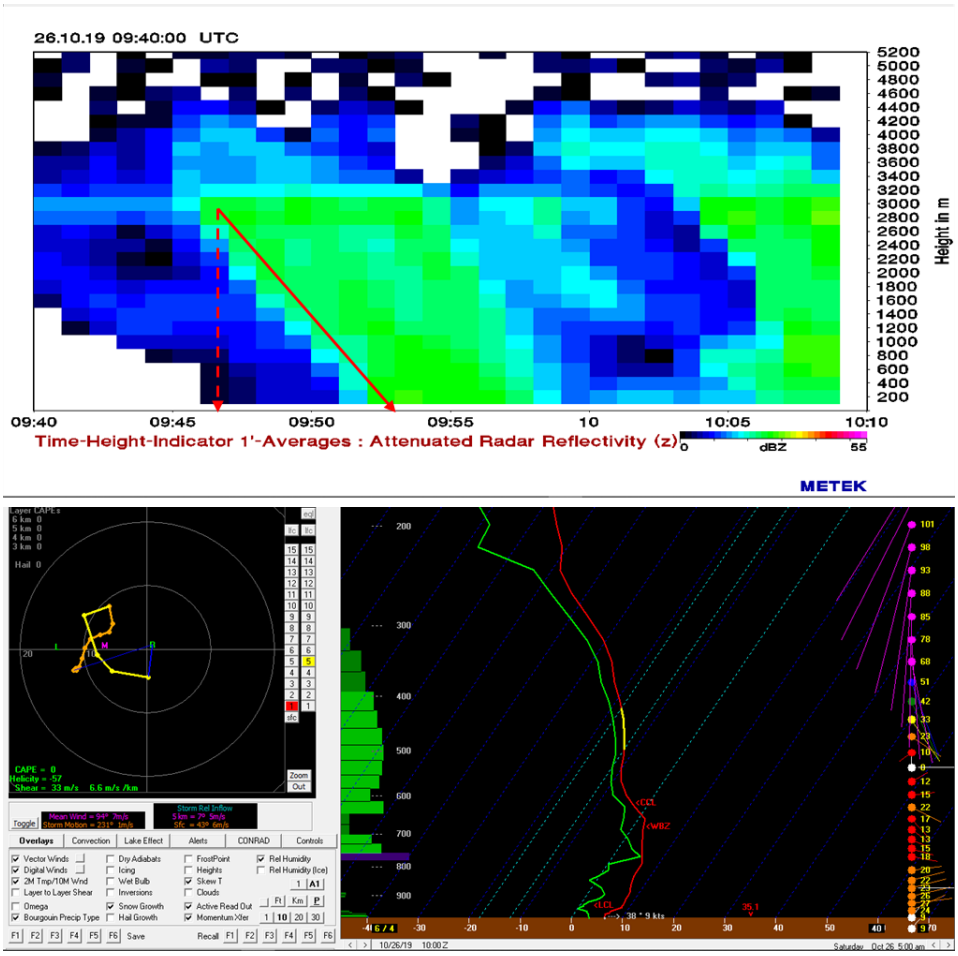

Figure 22 - MRR observation from October 26th (top) highlighting the radar reflectivity (dBZ) being affected by horizontal drift caused by speed and directional shear seen in the 12Z NAM 22hr forecast 1km-5km hodograph and low-level vertical wind profile.

The smaller the drop sizes and the more prevalent the wind shear, the more horizontal drift will be a factor in the MRR observations. For this reason, an assessment will need

to be made accounting for these factors when analyzing the evaporation cases. However, taking 15-minute averages of the data resolved this issue in the cases presented.

Calculations started from when rain was first being observed by the MRR at the height of the base of the cloud below the melting layer and include the point at which the rain fell to the lowest observable level of the MRR (200 m). Because the disdrometer data is measured for the same 15-minute interval as the MRR, this may have skewed observations of DSD's by including multiple minutes of little to no rainfall in the 15-minute average. Disdrometer observations are a negligible factor in the evaporation calculation but may be considered when observing and comparing a significantly lower count in DSD than the MRR presents at its lowest observable level (200 m). A comparison to a single minute observation with the laser disdrometer during the rainfall period would resolve the strong horizontal drift cases.

2.7 Methods for Modeling DSD's

Accurately modeling DSDs is a challenging endeavor given the many different environmental factors that can change the distribution. These factors create countless feedbacks, where elements such as relative humidity, horizontal wind shear and vertical velocities can control the rate at which DSDs change over the height of the column (Ulbrich 1983). The methods produced within this research demonstrate the traditional model of the gamma distribution developed by Ulbrich (1983) and the refined methods of weather radar rain profiling developed by Testud et al. (2000) using the analytical gamma distribution known as the method of moments (Willis 1984; Feingold et al. 1988; Willis and Tattelman 1989). A new model was proposed that adds terms of the Gaussian

distribution through a machine learning least of squares linear regression in order to quantify the many different shapes of DSDs for use in the evaporation quantification.

The gamma distribution (Equation 2) relates the varying drop sizes to the concentrations of those sizes. The method performed in Bongard (2019) to fit the observational data collected by the MRR into a quantifiable model to use in the evaporation equation is the method of moments (Carollo and Ferro 2015). This method takes the 3rd, 4th, and 6th moment of the gamma distribution to find the mu (μ) and lambda (λ) parameters which define the shape parameter and scale of the distribution respectively.

$$M_3 = \sum_{i=1} N_i(D_i) * \mathrm{D}^3 \quad (10)$$

$$M_4 = \sum_{i=1} N_i(D_i) * \mathrm{D}^4 \quad (11)$$

$$M_6 = \sum_{i=1} N_i(D_i) * \mathrm{D}^6 \quad (12)$$

Equations 10, 11 and 12 define the moments used to find the fitting parameters where $N_i(D_i)$ is the concentration as a function of the drop diameter D raised to the specific moment in layer i. This method aims at finding the gamma distributions median drop volume for fitting to the MRR observation with the equation:

$$\Gamma = \frac{M_4^3}{M_3^2 * M_6} \quad (13)$$

The μ and λ parameters are then found with the following:

$$\mu = \frac{((11*\Gamma-8)+(\Gamma*(\Gamma+8))^{0.5}}{2*(1-\Gamma)} \quad (14)$$

$$\lambda = \frac{(\mu+4)*M_3}{M_4} \quad (15)$$

where the μ and the λ parameters can be used in the Gamma distribution.

MATLAB provides a Gamma distribution fitting function that can also be used to find the μ and the λ parameters through a least of squares linear regression model. These scaling parameters are determined from built-in machine learning algorithms for a best fit distribution. The Gamma distribution function in MATLAB is defined by the following equation:

$$f(D|\mu,\lambda) = \int_{D_o}^{D_{max}} \frac{1}{\lambda^{\mu}\Gamma(\mu)} D^{\mu-1} * e^{\frac{-D}{\lambda}} dD \quad (16)$$

where the drop concentration $f(D|\mu,\lambda)$ is a function of the drop sizes for the 64 bins in the MRR or the 32 bins from the laser disdrometer and given by the shape parameter, μ, and the scaling parameter, λ. The gamma distribution closely approximates a normal distribution with the advantage that the gamma has density only for positive real numbers, and in the case of drop distributions gives weight to the higher concentrations of the smaller drops. The values of μ and λ are then used to display a best fit curve into the Ulbrich (1983) Gamma distribution (Equation 2). Figure 23 shows the Gamma fit curve using MATLAB's Gamma fit function.

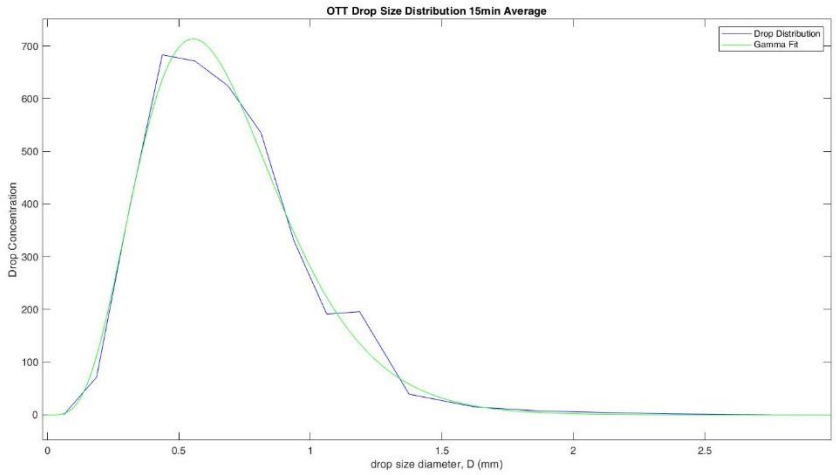

Figure 23 – The Gamma fitted DSD model compared to the 15-minute averaged observation of the laser disdrometer at 19Z on August 30th2019.

The Gamma distribution in Figure 23 by the "eye test" is a well-fitting curve to the laser disdrometer observation set. But another advantage of using the MATLAB function for fitting a curve distribution is the ability to obtain instantaneous curve fit statistics. For the case in Figure 23, R-square (R^2) and adjusted R-square (aR^2) are both parameters that can be used to assess the fitting of the curve. For Gamma fit in Figure 23 the R^2 and aR^2 are both greater than 0.98 which represents a good fit considering 1 would be a perfect match.

To date, a Gaussian function representing DSD's has not been explored. The Gaussian (Normal) function is a symmetrical, continuous bell curve given by:

$$f_g(D) = \int_{D_0}^{Dmax} \frac{1}{\sqrt{2\pi\sigma^2}} * \mathrm{e}^{-\frac{(D-\alpha)^2}{2\sigma^2}} \mathrm{dD} \qquad (17)$$

where variable $f_g(D)$ represents the modeled DSD, D is the drop diameter (mm), σ is the standard deviation, and α is the mean of the distribution. σ and α are similar to the shaping parameter μ and the scaling parameter λ of the gamma distribution respectively.

By itself, the Gaussian distribution does not model a true drop size distribution well, as seen in Figure 24.

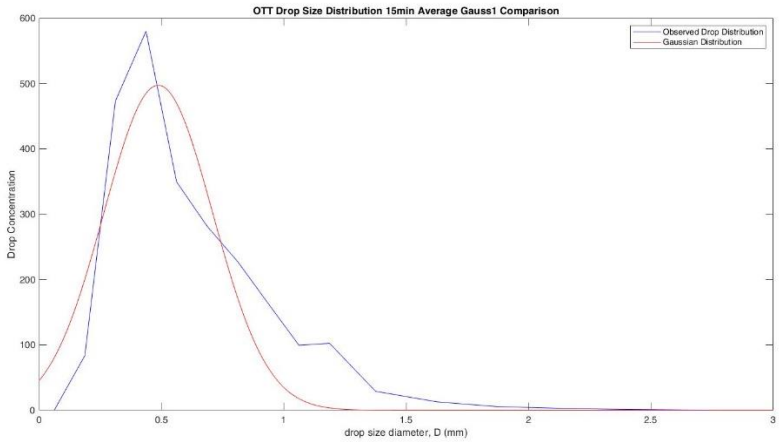

Figure 24 – 15-minute convective rain average captured by the OTT disdrometer on September 8, 2019 at 1215Z. The Y-axis is the drop concentration and the X-axis is the Drop diameter in mm. The blue curve is the averaged observed rain DSD and the red curve is the Gaussian distribution given by Eqn. 17

The Gaussian distribution does not accurately match the true distribution as it underestimates the peak of the DSD and significantly underestimates the smaller concentrations of larger drops (tail). The inaccuracy of a single Gaussian distribution also holds true with the fit statistics giving an R^2 of 0.87 and an aR^2 of 0.86. However, multiple iterations of the Gaussian distribution can be summed together using the linear regression algorithm that more closely represents the real distribution. The DSD of any instance of falling rain can have several spikes in concentrations and differ with atmospheric conditions at various times. This method of machine-driven regression modeling acts to resolve this fractal nature of rainfall much like the method of moments. Using two iterations of the Gaussian function produces a better fit, and as explained later, using three iterations is the best method.

$$f_{g_3}(D) = \int_{D0}^{Dmax} A_1\left(\exp\left[\frac{-(D-\alpha_1)^2}{{\sigma_1}^2}\right]\right) + A_2\left(\exp\left[\frac{-(D-\alpha_2)^2}{{\sigma_2}^2}\right]\right) + A_3\left(\exp\left[\frac{-(D-\alpha_3)^2}{{\sigma_3}^2}\right]\right) dD \quad (18)$$

Eqn. 18 is the summation of three iterations of the Gaussian distribution (Gauss3) where the coefficients A_1, A_2 and A_3 are given by $\frac{1}{\sqrt{2\pi\sigma_*{}^2}}$ where σ_* varies with each iteration determined by the regression algorithm. D is the drop diameter, σ is the standard deviation and α is the mean of the distribution.

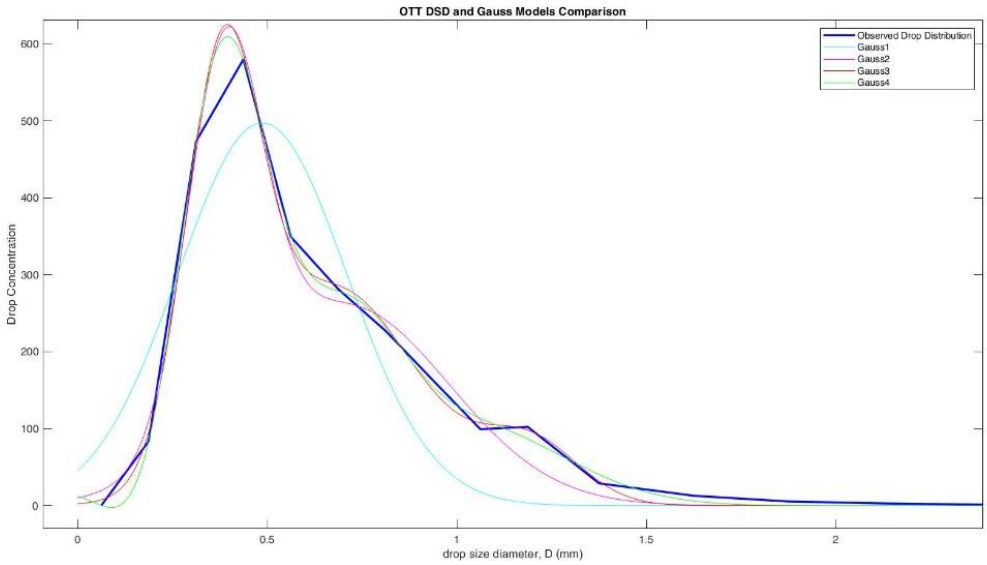

Figure 25 –Comparison between multiple cumulative iterations of the Gaussian Function and the real-time rain observation from September 8, 2019 at 1215Z.

Figure 25 demonstrates the comparison between the different Gaussian iterations. Gauss1 is clearly missing most of the curve, however Gauss2-Gauss4 all seem to be representing the curve accurately. An examination of the fit statistics bears out that Gauss4 had the best fit statistics of the four for this case.

Gaussian Statistics Table for Single Case	Gauss1	Gauss2	Gauss3	Gauss4
SSE	8.82E+04	5.20E+03	4.69E+03	7.60E+02
R^2	0.8715	0.9924166	0.9931602	0.9988932
AdjR^2	0.8626	0.9909582	0.9907811	0.9982845
DFE	29	26	23	20
RMSE	55.1567	14.148593	14.286499	6.1628141

Table 2 – Fit statistics of the different iterations of the Gaussian fit for the September 8, 2019 at 1215Z observation of DSDs. SSE is the sum of squares where lower values signify better fits. DFE is the degrees of freedom in the error, and RMSE is the root mean squared error where values closer to 0 signify better predictability.

However, the method of using the iterative Gaussian distributions has a significant limitation. If the number of Gaussian iterations exceeds the number of curves in the data set, the line will "blow up". Namely, the last unresolved iteration will proceed exponentially away from the values of the real dataset erroneously. This happens more frequently with more iterations of the Gaussian after Gauss3. Despite Gauss4 having a better fit in the case of September 8th at 1215Z, it is an unreliable measure to use exclusively. Gauss3 on the other hand thoroughly models most cases of DSDs, while the instances of blow up are seldom observed. This is demonstrated in the Gauss4 model in Figure 26. A more thorough statistical comparison between the Gauss3 and the Gamma distribution was made in the next section.

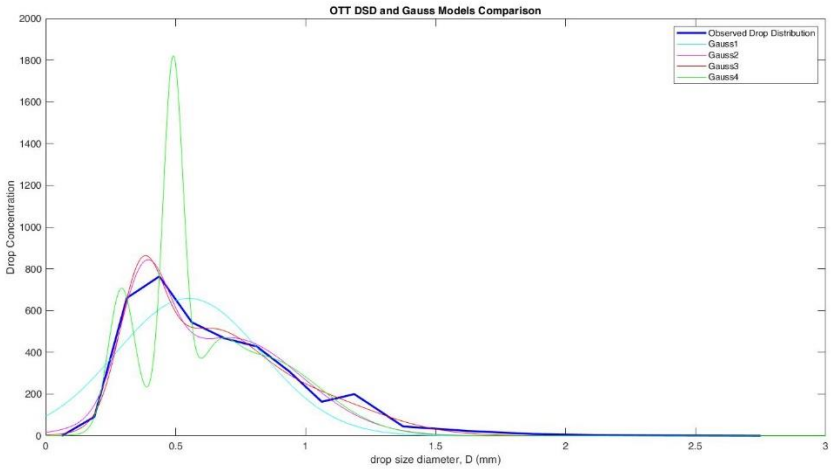

Figure 26 – An example of using too many iterations of the Gaussian distribution mixture such as seen in the Gauss4 (green line), the model can 'blow up' and not accurately represent the real DSD curve (thicker blue line).

The MRR DSDs can be compared and modeled similarly to the laser disdrometer. These modeled distributions will ultimately be used in the evaporation model to compare the rates of evaporation. The MRR provides a DSD for each 200 m level, as explained in section 2.2. This distribution is then displayed and compared on a logarithmic scale to the disdrometer output.

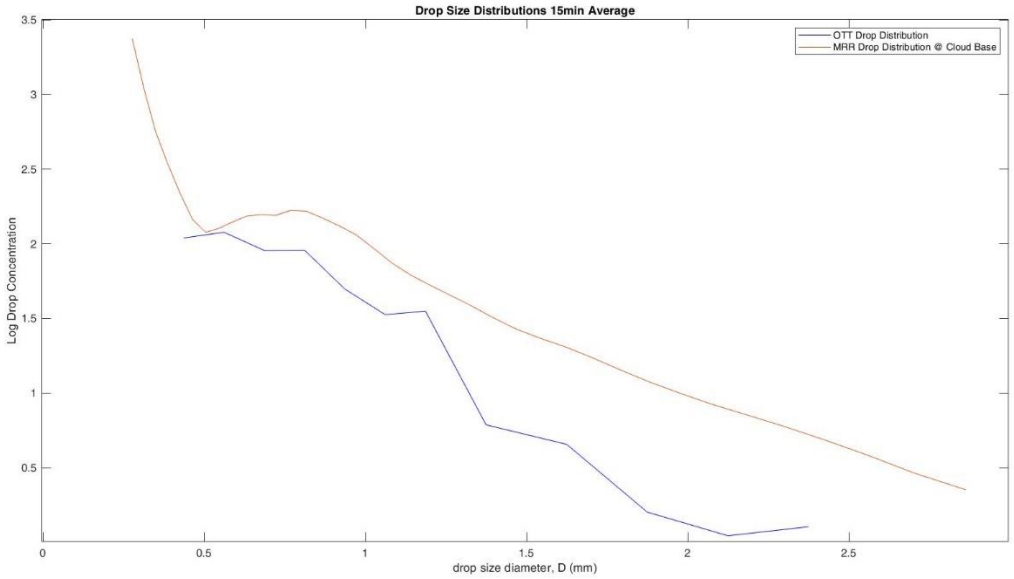

Figure 27 – Comparison of the drop size distribution from the MRR below the cloud base to the laser disdrometer at the surface.

In Figure 27, the general trend of the drop distribution between the MRR and the laser disdrometer is similar with much higher drop concentrations of smaller diameters falling toward lower concentrations of larger diameters. The overarching goal is to take the distribution derived from the bottom of the cloud base by the MRR and match a similar distribution to the laser disdrometer at the surface. If modeled correctly, the change in the distribution will also give LWC output at the surface that matches the observation. In order to solve these quantities, we must first model the DSD of the MRR correctly. Using the same methods used for the disdrometer DSD model, a Gamma and

Gauss3 derived DSD can be applied to the evaporation equation.

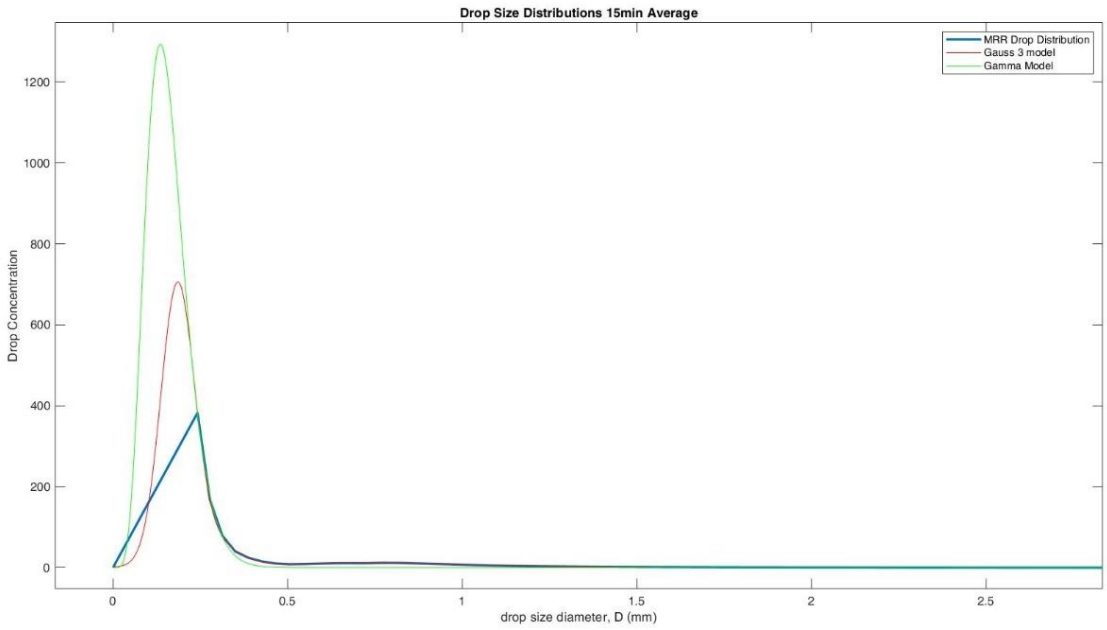

Figure 28 – Least of squares linear regression output for the MRR DSD taken from the base of the cloud for the Gauss3 (red line) and the Gamma (green line) models. Although both models overestimate the smaller end of the DSD, these droplets are more represented as in-cloud and will stay suspended until they are sufficiently large and will not significantly affect the evaporation model. Both models do particularly well matching the distributions above 0.25 mm in diameter.

In Figure 28, the DSD is over-estimated by both models with diameters lower than 0.25 mm. This did not have a significant impact on the evaporation model considering drops below this threshold will stay suspended in-cloud or will grow into bigger drops as they undergo collision and coalescence. Both models do well representing the distributions above 0.25 mm, with the Gamma model producing an R^2 of 0.98 and the Gauss3 producing an R^2 of 0.99. It can be seen in Figure 28 that the Gamma model (green line) underestimates the tail of the curve after 0.4 mm while the Gauss3 model (red line) coincides with the observation over the duration of the drop sizes. A more in-depth look comparing the model outputs through a thorough statistical analysis was examined in the next section.

2.8 Comparing Gauss3 and Gamma Model Outputs

Rain concentrations fall exponentially toward larger drop diameters observed by DSD's in the environment (Best 1950). However, not representing all sizes in the DSDs, especially larger drop diameter concentrations in a model can have implications for accurately calculating evaporation as well as other parameters like liquid water content (LWC), kinetic energy (KE), reflectivity (Z) and rain rates (RR). The following computations wer used with the 15-minute averaged DSD's observed from the laser disdrometer and referred to as the Raw Calculations, to compare the modeled Gamma and Gauss3 distribution output:

$$KE = \frac{\pi}{12}\rho * \sum_{D_0}^{D_{max}} N(D)D^3Vt(D)^2 \quad (19)$$

$$RR = \frac{\pi}{6} * \sum_{D_0}^{D_{max}} N(D)D^3Vt(D) \quad (20)$$

$$Z = 10 * log_{10}(\frac{\pi}{6} * \sum_{D_0}^{D_{max}} N(D)D^6) \quad (21)$$

$$LWC = \frac{\pi}{6}\rho * \sum_{D_0}^{D_{max}} N(D)D^3 \quad (22)$$

where ρ is the density of water, N(D) is the concentration, D is the diameter and Vt(D) is the fall velocity given in Equation 5. The units for KE are J m^{-2} hr^{-1}, mm hr^{-1} for RR, decibels (dBZ) for Z, and g m^{-3} for the LWC. By using these relationships and integrating the Gamma and Gauss3 functions, calculations of these parameters based on the model solution can be made:

$$RR_{gamma} = \frac{\pi}{6} * \int_{D0}^{Dmax} Nt * (D^{\mu}\exp[-\Lambda D])\, D^3\, Vt(D)\, dD \quad (23)$$

$$KE_{gamma} = \frac{\pi}{12} * \rho \int_{D0}^{Dmax} Nt * (D^{\mu}\exp[-\Lambda D])D^3Vt(D)^2 dD \quad (24)$$

$$Z_{gamma} = 10 * \log_{10}\left(\frac{\pi}{6} * \int_{D0}^{Dmax} Nt * (D^{\mu} \exp[-\Lambda D]) D^{6} \mathrm{dD}\right) \quad (25)$$

$$LWC_{gamma} = \frac{\pi}{6} * \rho \int_{D0}^{Dmax} Nt * (D^{\mu} \exp[-\Lambda D]) D^{3} \mathrm{dD} \quad (26)$$

where the integrations above are those of the Gamma distribution. The moment used for these calculations was the third as this is the most reliable for accurate LWC. Nt is the concentration parameter where m is the moment being expressed based on the parameter being calculated:

$$Nt = \frac{\int N(D) D^{m} dD}{\int D^{\mu+m} \exp[-\Lambda D] \mathrm{dD}} \quad (27)$$

This study will use the third moment (m=3) exclusively as it serves the purpose of evaluating evaporation through the change in LWC. More work will need to be accomplished to compare other methods of moments in the future studies. The Gauss3 parameters are found using following equations:

$$RR_{gauss3} = \int_{D0}^{Dmax} A_1 \left(\exp\left[\frac{-(D-\alpha_1)^2}{{\sigma_1}^2}\right]\right) + A_2 \left(\exp\left[\frac{-(D-\alpha_2)^2}{{\sigma_2}^2}\right]\right) + A_3 \left(\exp\left[\frac{-(D-\alpha_3)^2}{{\sigma_3}^2}\right]\right) \pi/6 \, D^3 \, Vt(D) dD \quad (28)$$

$$KE_{gauss3} = \frac{\pi}{12} \rho \int_{D0}^{Dmax} A_1 \left(\exp\left[\frac{-(D-\alpha_1)^2}{{\sigma_1}^2}\right]\right) + A_2 \left(\exp\left[\frac{-(D-\alpha_2)^2}{{\sigma_2}^2}\right]\right) + A_3 \left(\exp\left[\frac{-(D-\alpha_3)^2}{{\sigma_3}^2}\right]\right) D^3 Vt(D)^2 dD \quad (29)$$

$$Z_{gauss3} = 10 * log_{10}\left(\frac{\pi}{6} * \int_{D0}^{Dmax} A_1 \left(\exp\left[\frac{-(D-\alpha_1)^2}{{\sigma_1}^2}\right]\right) + A_2 \left(\exp\left[\frac{-(D-\alpha_2)^2}{{\sigma_2}^2}\right]\right) + A_3 \left(\exp\left[\frac{-(D-\alpha_3)^2}{{\sigma_3}^2}\right]\right) D^6 \, dD\right) \quad (30)$$

$$LWC_{gauss3} = \frac{\pi}{6}\rho \int_{D0}^{Dmax} A_1 \left(\exp\left[\frac{-(D-\alpha_1)^2}{{\sigma_1}^2}\right]\right) + A_2 \left(\exp\left[\frac{-(D-\alpha_2)^2}{{\sigma_2}^2}\right]\right) +$$

$$A_3 \left(\exp\left[\frac{-(D-\alpha_3)^2}{{\sigma_3}^2}\right]\right) D^3 \, dD \qquad (31)$$

where the units are the same as the units in Equations 19-22 and the coefficients match those in eqn. 18. While fitting the real time DSD curve with a model DSD is an important first step, slight deviations in diameter concentrations, especially in the higher diameters, can have profound impacts in the accuracy for calculated parameters.

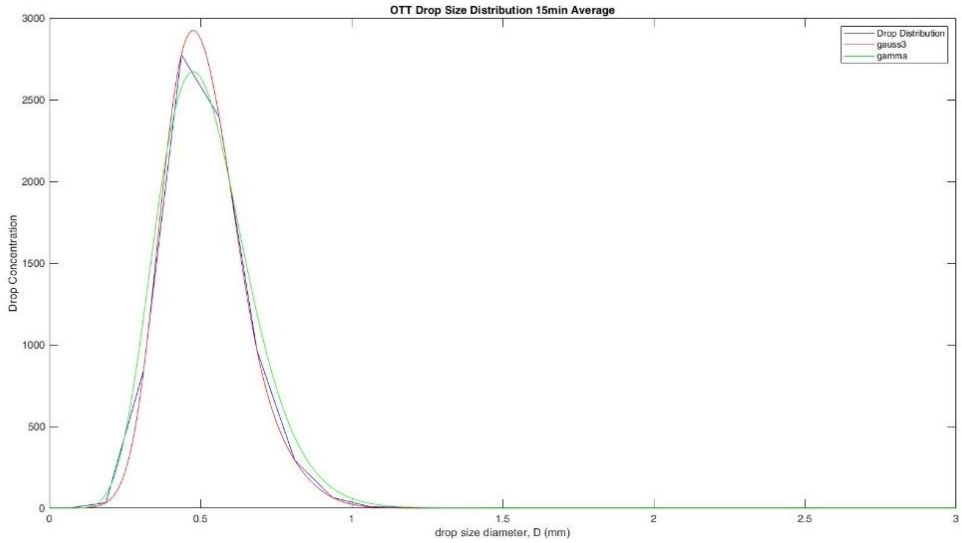

Figure 29 –DSD case from September 22nd ,2019 at 2000Z. This DSD will be used for the following figures to compare how the model calculations handle the DSD as it relates to the four practical parameters.

Figure 29 displays how the two models match up from a DSD perspective. This instance of rainfall is relatively uniform in its distribution and therefore should be well represented by both models. The integrations under the curve in Equations 19-31 finds the total drop size distribution and calculates the values contributed by each concentration into a final summation of each parameter.

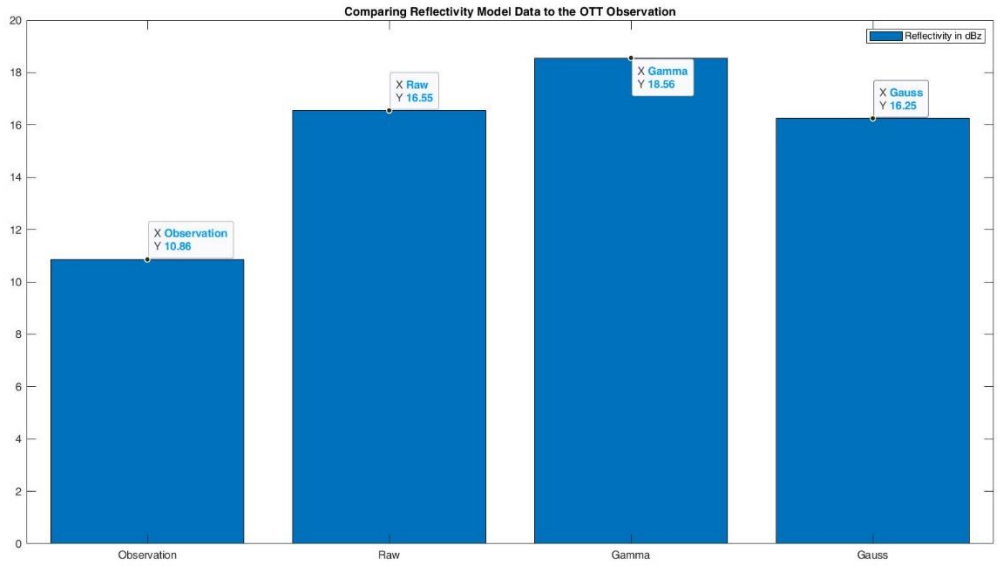

Figure 30 – Calculations made from the September 22nd 2019 case at 2000Z and compares the reflectivity calculation from Equation 21 (Raw) to the disdrometer's software calculation (Observations) to the Gamma (Equation 25) and Gauss3 (Equation 30) model calculations.

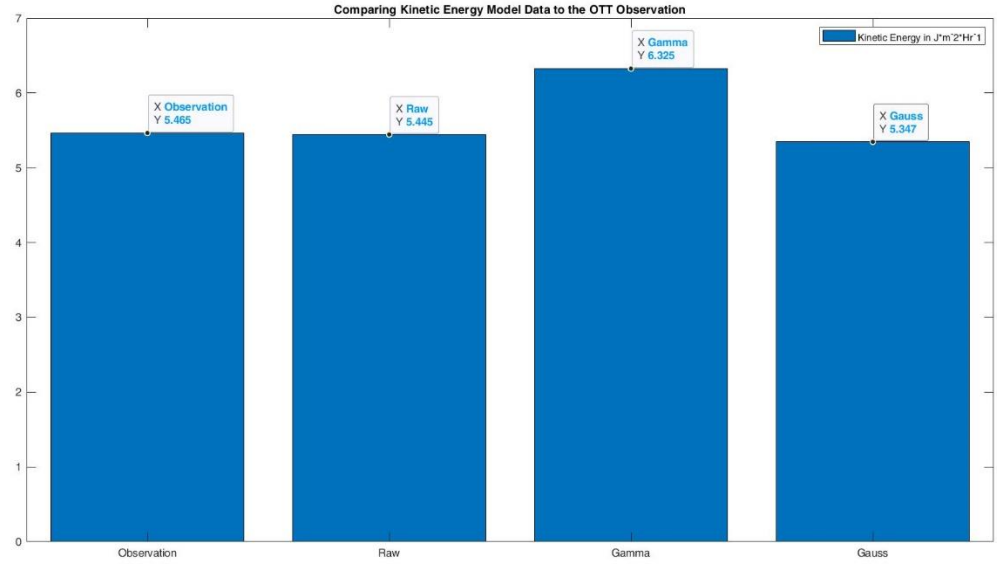

Figure 31- Calculations made from the September 22nd 2019 case at 2000Z and compares the kinetic energy calculation from Equation 19 (Raw) to the disdrometer's software (Observations) to the Gamma (Equation 24) and Gauss3 (Equation 29) model calculations.

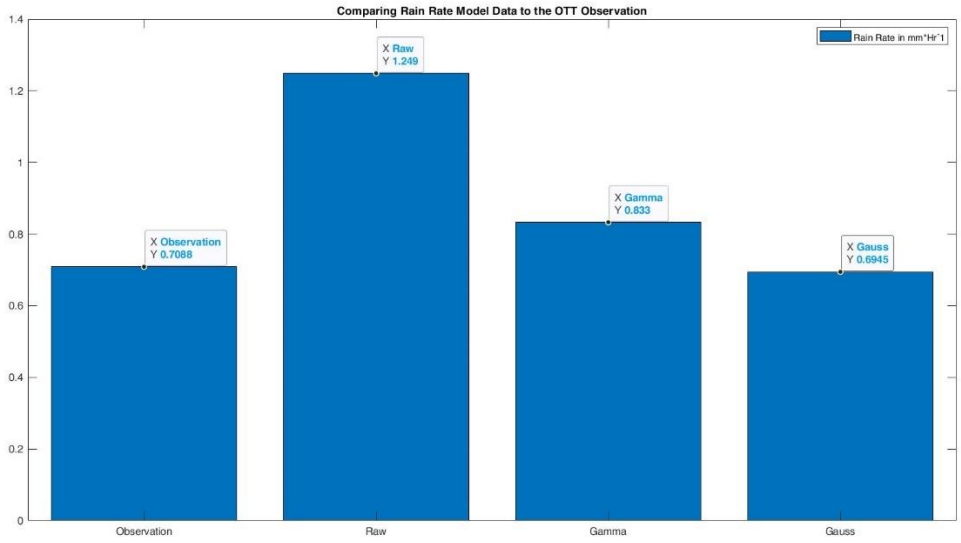

Figure 32 - Calculations made from the September 22nd 2019 case at 2000Z and compares the rain rate calculation from Equation 20 (Raw) to the Disdrometers software (Observations) to the Gamma (Equation 23) and Gauss3 (Equation 28) model calculations.

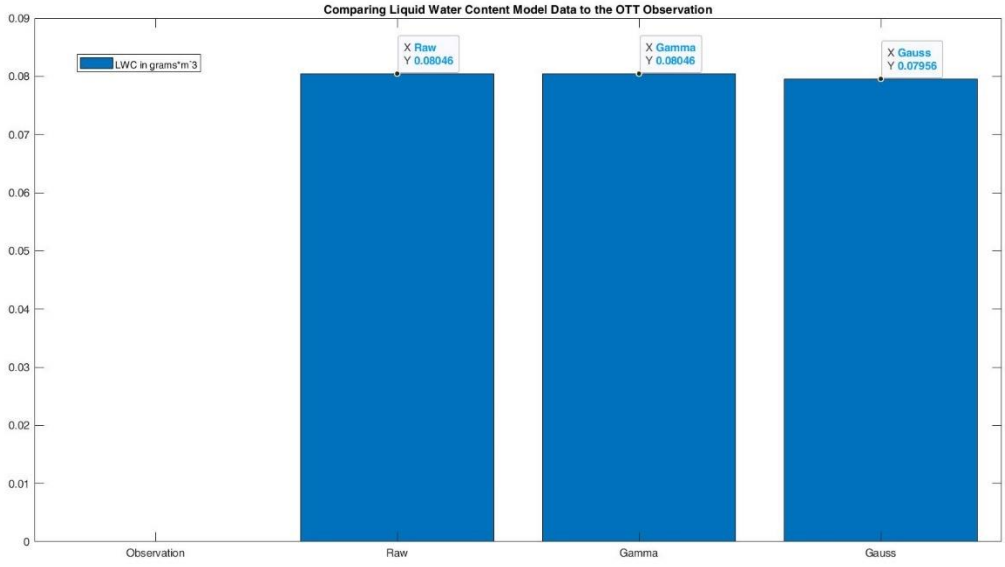

Figure 33 - Displays the calculations made from the September 22nd 2019 case at 2000Z and compares the LWC calculation from Equation 22 (Raw) to the Gamma (Equation 26) and Gauss3 (Equation 31) model calculations. For this parameter the instrument software does not generate a value.

Figures 30-33 display how the Gaussian and Gamma DSD models compare to the real-time observations for a single, 15-minute period on September 22, 2019. The laser disdrometers' software does not include LWC, labeled as observation in Figure 33, as a measured parameter. The raw calculation will suffice as a comparative tool in the case of LWC. It is also noted that the equations the laser disdrometer uses are not known, but will still be considered an accurate measurement of the calculated parameters. From a glance, both calculated parameters match up relatively well to the observed.

Statistics Comparison Table for Single Case	Gauss3	Gamma
SSE	36.543	235944.42
R^2	0.9999973	0.982479602
AdjR^2	0.9999963	0.981271299
DFE	23	29
RMSE	1.2604941	90.19985801

Table 3 – Fit statistics for the Gauss3 and the Gamma model from the DSD case on September 22nd, 2019 at 2000Z.

When examining the fit statistics for the model output, the Gauss 3 model outperforms the Gamma in all categories with a nearly 100% accurate R^2 and aR^2. However, the Gamma model still performs exceptionally well by those measures. Even so, when examining the parameter outputs, slight differences still emerge.

In Figure 30, the Gauss3 model more closely represents the raw and observed Z values, while the Gamma model overestimates in both real measurements. In Figure 31, the Gauss3 model again outperformed the Gamma model in total KE for both the raw

calculation and the observation from the laser disdrometer. The RR in Figure 32 shows a much higher raw calculation than the observed with the Gamma model more closely representing that parameter, however the Gauss3 parameter does match the disdrometer observation much better where the Gamma once again overestimates. In the case of the LWC in Figure 33, arguably the most important parameter for this research, the Gamma calculation exactly matches the raw LWC calculation. This is because the Gamma distribution concentration calculation (Equation 27) made here represents the 3rd moment and is specifically designed to calculate accurate LWC. However, the Gauss3 is not far off a 100% accurate measurement and is arguably a better representation of all the calculated parameters for this one case. To make such a claim for all cases, multiple periods of rainfall would need to be analyzed and compared statistically using the best fit statistics and calculated parameters.

Statistical Comparison of Gamma and Gauss3 Distribution for 673 Rain Cases		
n = 673	Gauss3	Gamma
R^2 Mean	0.995284562	0.967288645
aR^2 Mean	0.99364441	0.965032689
SSE Mean	5966.348153	62932.38083
RMSE Mean	10.33756154	28.66404232
Max R^2	0.999999997	0.999889443
Min R^2	0.910141299	0.321984556
STD R^2	0.006575023	0.048305714

Table 4 – Statistical comparison of 673 15-minute averaged observations of the Gauss3 and Gamma curve fit statistics.

Table 4 shows how the fit statistics compare for the two models being run. The models were run through 673 15-minute periods of rain using the respective machine-driven linear regression algorithms to find a best fit for each DSD. These best fit models then produce fit statistics that were appended into an excel file for analysis. Like in the

single case scenario, the Gauss3 model outperforms the Gamma distribution model in all measurable parameters. Also like the single case, the statistics for both models are within a tolerable range for reliable DSD quantifications. Comparisons can also be drawn from the calculations made from equations 19-31 and the observations of the laser disdrometer.

In tables 5-8, the calculations of equations 19-31 are run for each of the 673 15-minute averaged rain observations made. Roughly 2% of the model runs resulted in blow up, where the calculated parameters were outside of a reasonable range. Those were identified and removed from the data set statistics but were still included in the total observation count (n). The Gauss3 model experienced this more (13 runs) than the Gamma model (2 runs) and mostly occurred in cases where very small and sporadic DSDs were observed. In these cases, the data sets from both models were removed to maintain continuity in the statistical analysis but retained in the total count to illustrate the model's overall effectiveness. It is also worth noting that the rain cases that experienced blow up were also mostly with distributions outside of the G&K velocity distribution curve. The method applied to compare the parameter calculation of the real distributions to the calculated parameters of the Gauss3 and Gamma model distributions was to find the absolute value of the difference between the raw and observed values to the modeled values. This is important when looking at DSD's because although a distribution may have a better fit overall, it may not translate to better calculated parameters if certain areas of the DSD curve are missed. A thorough statistical analysis will help establish if the modeled distributions are covering the range of drop sizes that significantly impact the measurements of the calculated parameters. The accuracy of

these parameters is important as they are then included into forecast models and used in the case of LWC in the evaporation model.

Statistical Difference Comparison of the Kinetic Energy (J m^{-2} hr^{-1}) for 673 Rain Observations

n=673	Gamma	Gauss3	% Gamma Observations	% Gauss3 Observations
Mean Difference observation	24.418	25.750	97.9	97.9
Max Difference observation	911.848	993.645	97.9	97.9
Min Difference observation	0.002	0.001	97.9	97.9
STD Difference observation	68.088	74.153	97.9	97.9
Mean Difference Raw Calc	1.358	3.496	97.9	97.9
Max Difference Raw Calc	105.779	82.081	97.9	97.9
Min Difference Raw Calc	0.001	0.000	97.9	97.9
STD Difference Raw Calc	5.448	8.515	97.9	97.9
Mean & % Diff <10 observation	2.516	2.819	60.2	63.0
Mean & % Diff <10 Raw Calc	0.912	1.644	98.6	92.4
Mean & % Diff <5 observation	1.296	1.512	48.1	48.7
Mean & % Diff <5 Raw Calc	0.852	0.951	97.6	82.4
Mean & % Diff <1 observation	0.235	0.256	27.5	25.9
Mean & % Diff <1 Raw Calc	0.028	0.024	65.9	56.1

Table 5 – The statistical analysis of the difference between the laser disdrometer observed and raw calculations (Equation 19) of kinetic energy, from the Gauss3 and Gamma model derived kinetic energy calculations from Equations 29 and 24 respectively.

Table 5 compares the KE calculations by taking the difference of the raw calculated and observed values by the laser disdrometer from both the Gamma and Gauss3 models. Table 5 also shows the difference from the values calculated by the raw DSD curve in equations 19-22. The mean difference represents the average of how far the model is from the observation and raw calculations. The first thing to note in the KE calculations is that both models matched poorly with the laser disdrometer observation but did relatively well with the raw calculations. Differences less than 10 J m^{-2} hr^{-1} improved the mean difference but only represented 60%-63% of the model observations while the raw calculations of differences less than 10 J m^{-2} hr^{-1} were 92%-98%. By knowing how the laser disdrometer calculates its parameters, more could be deduced

from this information. When comparing the two model outputs, the Gamma has the edge in the statistical comparison. It has a lower mean difference and a smaller standard deviation difference for the raw calculation. The Gauss3 does have smaller range, however in percent of observation and mean differences less than 10, 5 and 1, the Gamma increasingly has the edge over the Gauss3 for KE.

Statistical Difference Comparison of the Reflectivity (dBZ) for 638 Rain Observations

n = 638	Gamma	Gauss3	% Gamma Observations	% Gauss3 Observations
Mean Difference observation	6.090	6.594	97.5	97.5
Max Difference observation	53.621	51.496	97.5	97.5
Min Difference observation	0.003	0.003	97.5	97.5
STD Difference observation	9.176	4.711	97.5	97.5
Mean Difference Raw Calc	2.825	5.539	97.5	97.5
Max Difference Raw Calc	11.943	56.936	97.5	97.5
Min Difference Raw Calc	0.010	0.002	97.5	97.5
STD Difference Raw Calc	1.259	6.478	97.5	97.5
Mean & % Diff <10 observation	2.213	5.022	79.3	83.3
Mean & % Diff <10 Raw Calc	2.770	3.271	99.5	84.2
Mean & % Diff <5 observation	1.178	3.034	65.6	42.0
Mean & % Diff <5 Raw Calc	2.625	1.945	96.0	62.1
Mean & % Diff <1 observation	0.498	0.477	37.5	5.0
Mean & % Diff <1 Raw Calc	0.033	0.034	2.9	21.7

Table 6 – The statistical analysis of the difference between the laser disdrometer observed and raw calculations (Equation 21) of reflectivity, from the Gauss3 and Gamma model derived reflectivity calculations from equations 30 and 25 respectively.

Table 6 shows the reflectivity and compares to Table 5 in much the same way. A few cases with very small DSDs were excluded from the data as they caused unrealistic calculations bringing n to 638. Both models do not compare well to the observations made by the laser disdrometer, nevertheless both do well with the raw calculations with Gamma and the Gauss3 mean difference being 2 dBZ and 5 dBZ respectively for all observations. Just looking at the comparison for the raw calculations moving forward, Gamma has a smaller standard deviation, smaller mean, higher percentage of

observations with a difference less than 10 dBZ at 99.5% and a higher percentage of observations with a difference less than 5 dBZ at 96%. The Gauss3 does have the edge with a higher percentage of observations with a difference less than 1 dBZ at 21.7% of the total observations while the Gamma's performance is an abysmal 2.9%. Both models' mean differences below 10, 5 and 1 dBZ did exceptionally well despite the Gamma performing better in most instances.

Statistical Comparison of the Liquid Water Content (g m^{-1}) for 673 Rain Observations

n = 673	Gamma	Gauss3	% Gamma Observations	% Gauss Observations
Mean Difference Raw Calc	0.01805	0.03731	97.92	97.92
Max Difference Raw Calc	3.41421	1.18563	97.92	97.92
Min Difference Raw Calc	0.00000	0.00000	97.92	97.92
STD Difference Raw Calc	0.17596	0.10280	97.92	97.92
Mean & % Diff <0.1 Raw Calc	0.00220	0.01497	99.85	91.81
Mean & % Diff <0.01 Raw Calc	0.00021	0.00242	94.69	58.27
Mean & % Diff <0.001 Raw Calc	0.00003	0.00022	91.20	27.31

Table 7 – The statistical analysis of the difference between the raw calculations of liquid water content (Equation 22) from the Gauss3 and Gamma model derived liquid water content of Equation 31 and 26 respectively .

Table 7 shows the LWC difference for the raw calculation made in Equation 22 to the Gauss3 and Gamma model. The clear winner is the Gamma model putting forth phenomenal LWC value accuracy. The Guass3 did not underperform in the calculations, turning in a max difference and standard deviation lower than the Gamma, however the percentage of observations with differences below 0.1, 0.01 and 0.001 g m^{-3} were far superior in the Gamma model with the observations for all three differences staying above the 90 percentile. As previously stated, the 3rd moment used for the LWC calculation proves to be a very accurate method of modeling LWC calculations, but Gauss3 can still be used as an accurate DSD quantification.

Statistical Difference Comparison of the Rain Rate (mm hr^{-1}) for 673 Rain Observations				
n = 673	Gamma	Gauss3	% Gamma Observations	% Gauss3 Observations
Mean Difference observation	0.993347807	0.95436727	97.8	97.8
Max Difference observation	117.8151747	36.61520786	97.8	97.8
Min Difference observation	0.000240052	6.16856E-06	97.8	97.8
STD Difference observation	6.149361381	2.783136091	97.8	97.8
Mean Difference Raw Calc	1.445341812	1.276084362	97.8	97.8
Max Difference Raw Calc	157.0964872	37.07871304	97.8	97.8
Min Difference Raw Calc	0.001412773	0.000557719	97.8	97.8
STD Difference Raw Calc	8.199686821	2.893502363	97.8	97.8
Mean <5 observation diff	0.380260106	0.486368941	97.0	95.4
Mean <5 Raw Calc diff	0.51783671	0.786241489	95.6	95.4
Mean <1 observation diff	0.215982631	0.177506113	87.8	80.5
Mean <1 Raw Calc diff	0.251481971	0.312911334	81.9	72.0
Mean <.1 observation diff	0.029089918	0.024184155	35.0	45.4
Mean <.1 Raw Calc diff	0.030374002	0.029889952	29.2	24.2

Table 8 - The statistical analysis of the difference between the laser disdrometer observed and raw calculations (Equation 20) of rain rate, from the Gauss3 and Gamma model derived rain rate calculations from equations 28 and 23 respectively.

The Gauss3 model outperformed the Gamma model with the rain rate calculation. In Table 8, unlike Tables 5 and 6, the laser disdrometer's observation closely matches the raw calculation numbers and so retains a sense a viability for this parameter. The Gauss3 has a lower mean difference, max difference, minimum difference and a smaller standard deviation for both the laser disdrometer observation and the raw calculations. The Gamma model does carry a higher percentage of observational difference below 5, 1 mm hr^{-1}, however the Gauss3 beats the Gamma by nearly 10% with the number of observation differences below 0.1 mm hr^{-1} in the laser disdrometer observation. The mean differences below 5, 1 and 0.1 mm hr^{-1} are very similar to both models, so there is no clear preference as the models perform equal as well.

Given the parameter calculation comparisons, the Gamma DSD performs better overall than the Gauss3 DSD model. A more thorough examination into the how each model compares with specific rain scenarios would provide more information as to which model performs better situationally. Namely, which model works better for convective and non-convective precipitation. Also, examining a multitude of locations would help to randomize the study. Moving forward to the evaporation model, both drop distributions were explored and compared for each case study.

3. Results

3.1 Case Study Setup

Three case studies using observed soundings were conducted during this research. Because of limited supplies available, case studies were performed under high confidence forecast parameters that indicated a significant dry layer was present to maximize the evaporation signal. These parameters included several days of high model confidence in which liquid precipitation would pass through a dewpoint depression (DPD) greater than 8°C, signifying a pronounced dry layer for evaporation to be observed. Another requirement was that the height of the melting layer resided above 1 km from the surface to avoid ice crystal contamination. Once these parameters were met, a group of graduate and undergraduate University of Missouri students and other professionals gathered to collect the environmental data to be used in the evaporation model.

In Bongard (2019) balloon data was collected up to the point precipitation began to be observed at the surface. This assumed that the atmospheric profile was saturated at the time that precipitation had started to reach the surface. The techniques in this research deviate from this method. A dry layer may still be present at the time precipitation begins to reach the surface. Balloon data in these cases was continued to be collected if a DPD of greater than 8°C was still observed in the dry layer, given enough supplies were available. This was done to observe the evolution of the DSD as they reached the surface and to compare to the laser disdrometer measurements. Additionally, three different quantifications of DSD were examined in the evaporation model. These are the least of squares linear regression fitted Gauss3 and Gamma fit DSD, as well as the Bongard (2019) method of moments (MOM). Furthermore, the derived vertical motions (VM)

from the balloon ascension was included and compared for all the case studies. Lastly, model derived soundings were tested to determine if they can be reliably used to accurately quantify evaporation.

The evaporation quantification of the column was determined by the rate of change of the LWC from the cloud base to the lowest observable level (LOL). The MRR LOL was 200m. Comparing the three DSD modeled evaporation rates to that of the observed MRR revealed how the differing methods handle evaporation through the dry layer. Taking an LWC perspective is a more practical method and an easier association to interpret as the distribution changes through the dry layer. LWC is calculated at the heights using the modeled DSD formulations. For the MRR there is a direct observation of the DSD separated into the 64 bins. The modeled DSDs are parameterized to provide a concentration of each drop size at the top of the dry layer. The different drop sizes are passed through the evaporation calculation to provide a new drop diameter at each proceeding layer. The new drop sizes are passed through layer by layer, while each evolution is calculating new concentrations of drop diameters due to evaporation until they reach the LOL. DSD are summed using Equation 32 to get an LWC at each layer height based on the new concentration.

$$LWC(DSD_m, h) = \sum \frac{\frac{\pi}{6} * DSD_m(h) * D_e(h)^3}{10} \tag{32}$$

The LWC calculation in equation 32 is the summation of the total LWC in each layer and is a function of the DSD method used (DSD_m) which is the concentration ($N(D_i)$) that changes with the method at the top of the dry layer (h). D_e is the new drop diameter from equation 13 for each proceeding layer.

3.2 October 5th, 2019 Case Study

On October 5th, 2019 a low-pressure system developed on the leeside of the northern Rockies and made a slow progression east as it ran into a strong blocking upper level ridge. Southwesterly gradient between the strong surface high pressure system over NE CONUS and the weakly dynamic low system over the Dakotas advected dry air into the lower levels of mid-Missouri with rain forecasted to occur along the approaching frontal boundary. An inverse ridge also helped to block significant low-level moist air advection along the Gulf states from advecting into the lower levels.

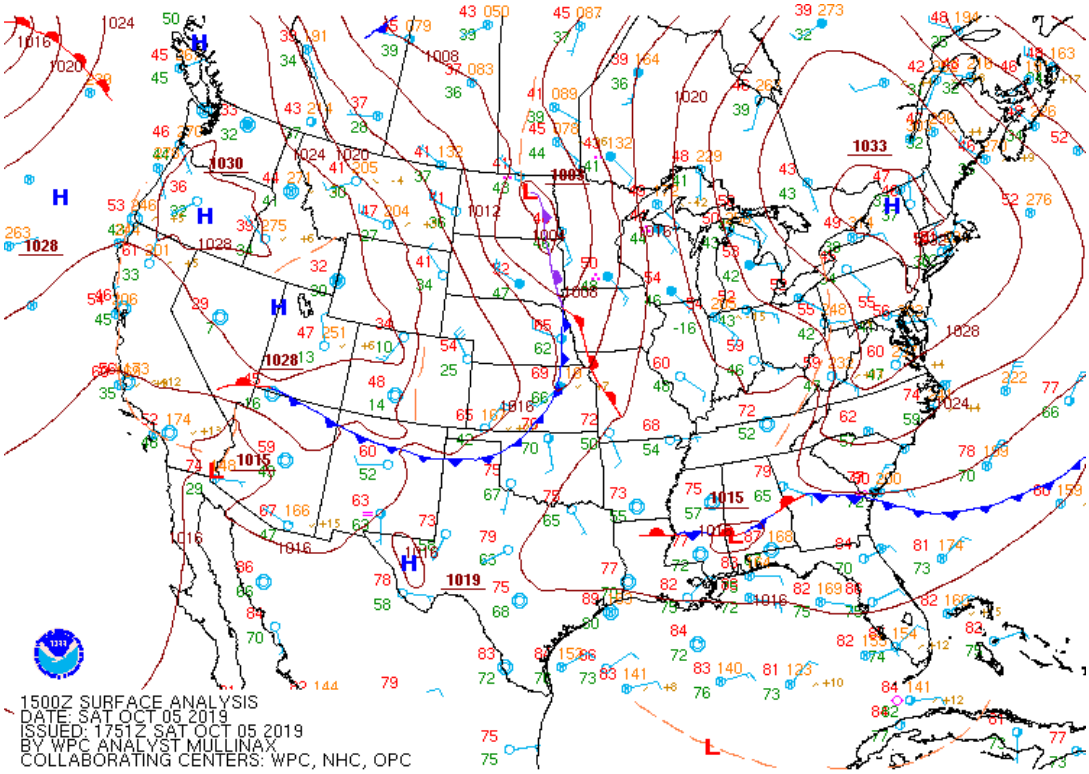

Figure 34 - The 15Z surface analysis from October 5th, 2019.

The 12Z observed surface sounding from Springfield, MO confirmed the presence of a strong dry layer, and the observed precipitation upstream signified a well-suited evaporation case study for balloon observations.

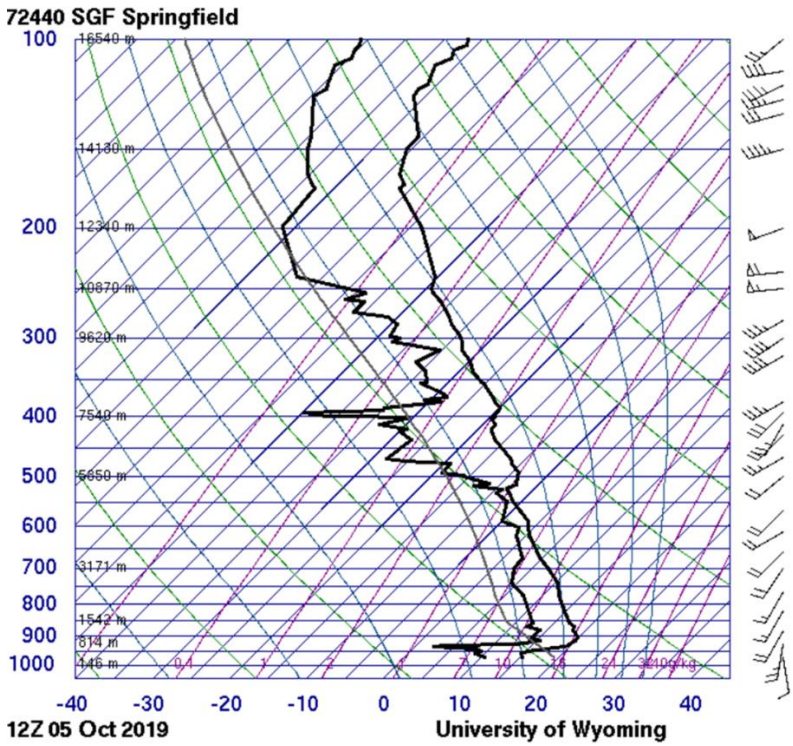

Figure 35 - Springfield Missouri observed sounding indicating a strong low-level dry layer and drying southwesterly flow in the lower levels.

Four weather balloons where launched during the observation period. The first balloon was launched at 1500Z, referred to as balloon A. Balloon B was in the air by 1630Z, balloon C was up at 1800Z and the last observation was Balloon D at 1930Z. Balloon C was a failed launch as it is believed the radiosonde became detached from the balloon shortly after takeoff.

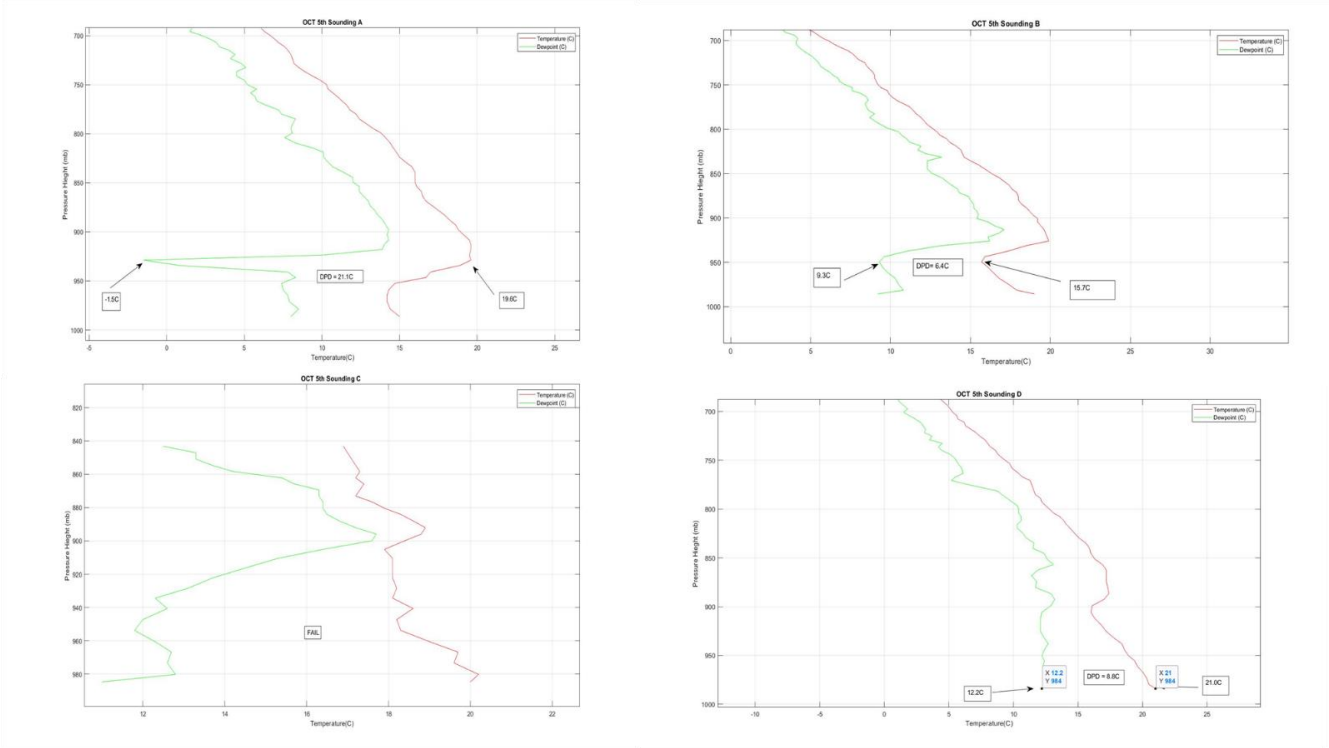

Figure 36 - Low-level profiles of each of the 4 balloon observations and the dew point depression of the observation for each sounding. Balloon sounding C was a failed launch.

3.2.1 October 5th, 2019 Balloon B Analysis

No precipitation was observed by the MRR or the disdrometer between the times of the 1st and the 3rd balloon observation period, so balloon A was not used in the any of the model simulations. At 1815Z radar from MZZU had indicated light precipitable returns on the order of 20 dBZ. This also matched with the observation from MRR. Because balloon C had failed, balloon B was used as a representative sounding to run the evaporation model.

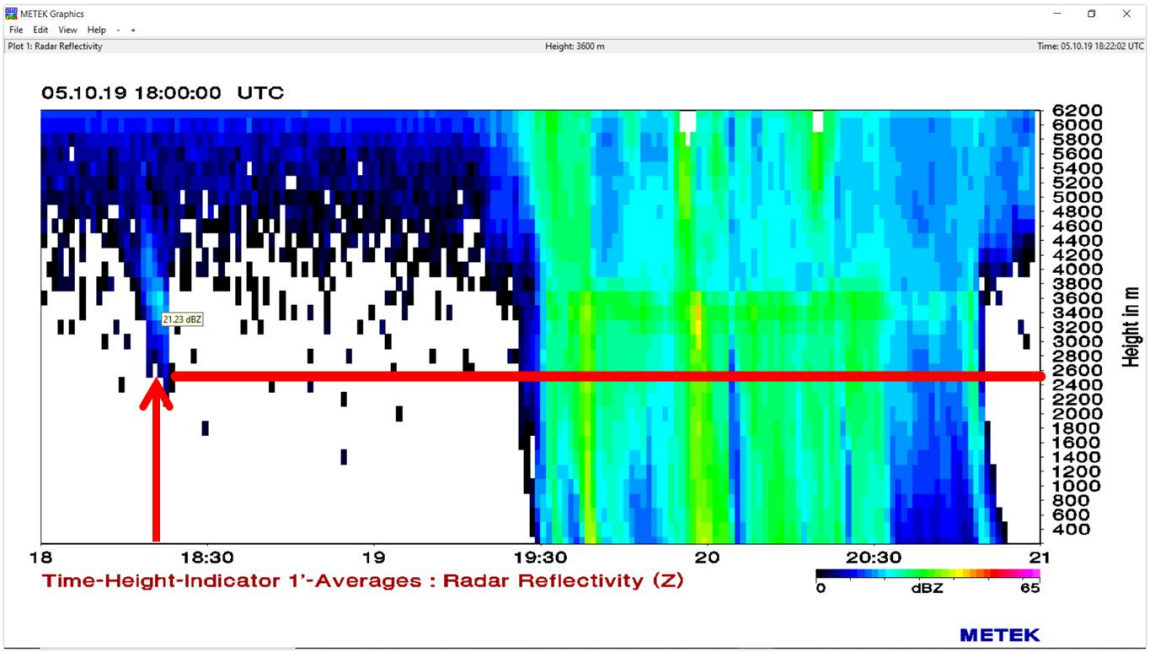

Figure 37 – The observation of rainfall from the MRR highlighting the diminishing reflectivity presumably due to evaporation below the cloud base at 1820Z.

The MRR indicates that all precipitation had been evaporated below 2.4 km and there was no observation of rain on the laser disdrometer. The modeled evaporation should also show this and will be an indication of its functionality. Running the evaporation model with simulated drop sizes demonstrates how the evaporation model is handling the scenario.

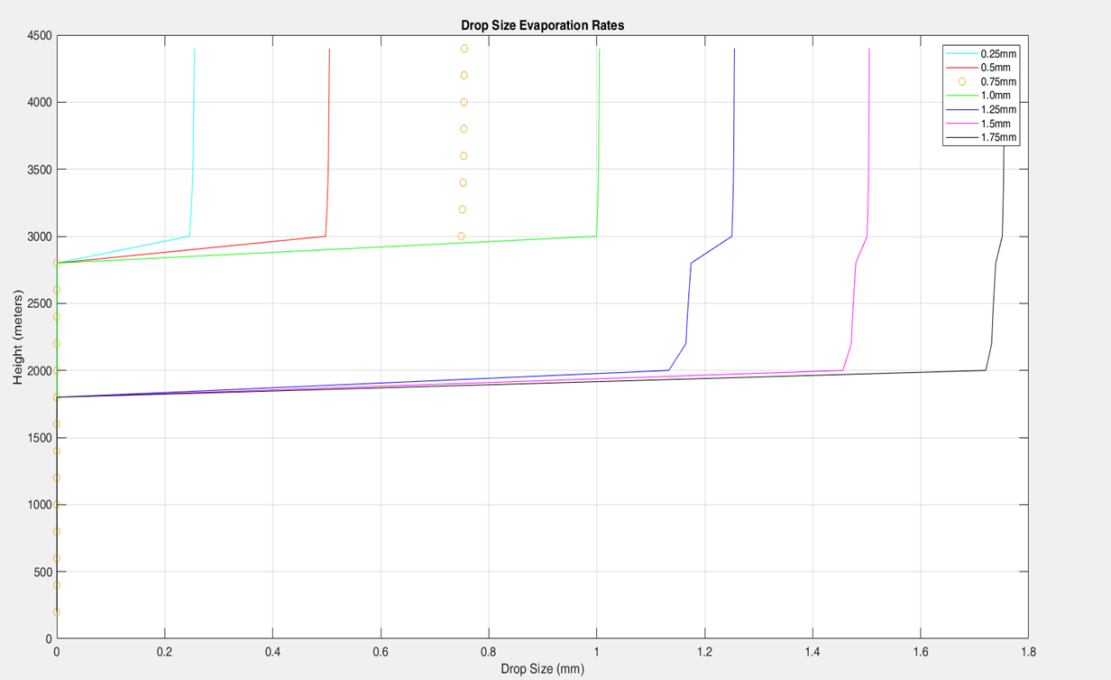

Figure 38 – Evaporation model simulation with the observed balloon B environment including the derived VM of balloon ascent with simulated rain drop sizes on October 05th 1820Z.

Figure 38 demonstrates with simulated rain drop sizes that all drops smaller than 1.75 mm will evaporate above 1.7 km. Also, of note is a clear distinction in the evaporation rates between the 1.0 mm and the 1.25 mm drop sizes. Figure 38 demonstrates that a decrease in the drop diameters greater than 1.25 mm substantially increases below 2 km. This is due to the considerable decrease in the relative humidity profile at that level causing all the drop sizes to evaporate fully and an increase of the observed upward VM produced by the convergence at the boundary layer. Running the model using simulated drop sizes can show how specific drop distributions respond given the detailed parameters of the observed sounding. In cases where drops reach the surface, they can be compared to the laser disdrometer distribution as a model accuracy tool.

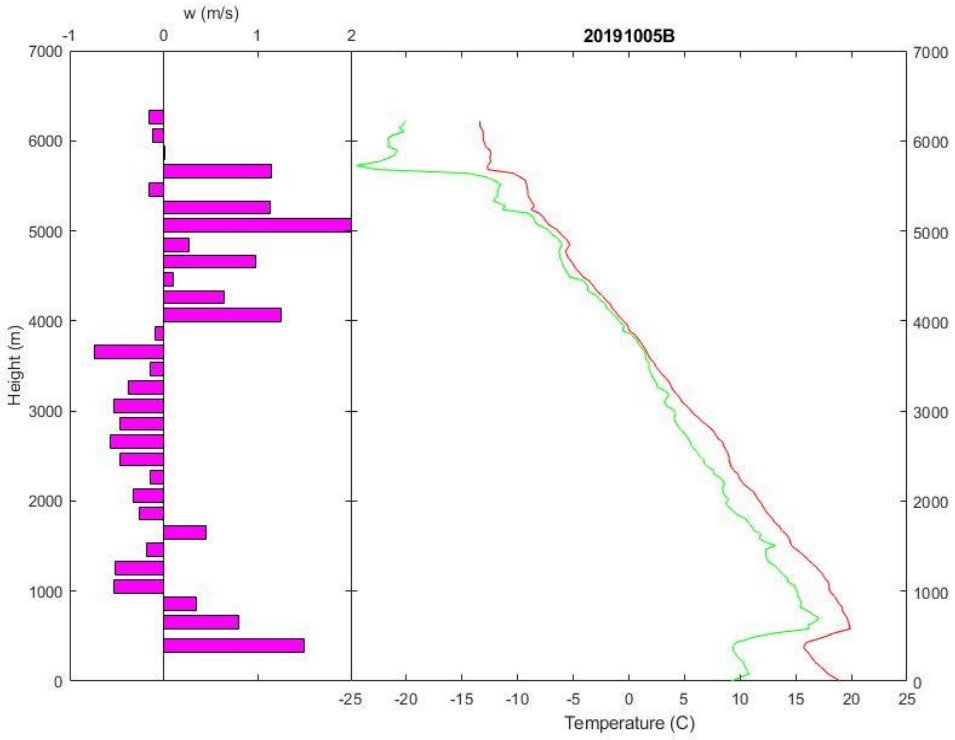

Figure 39 – Balloon derived VM (pink bars) next to the environmental temperature (red line) and dewpoint (green line) for balloon B.

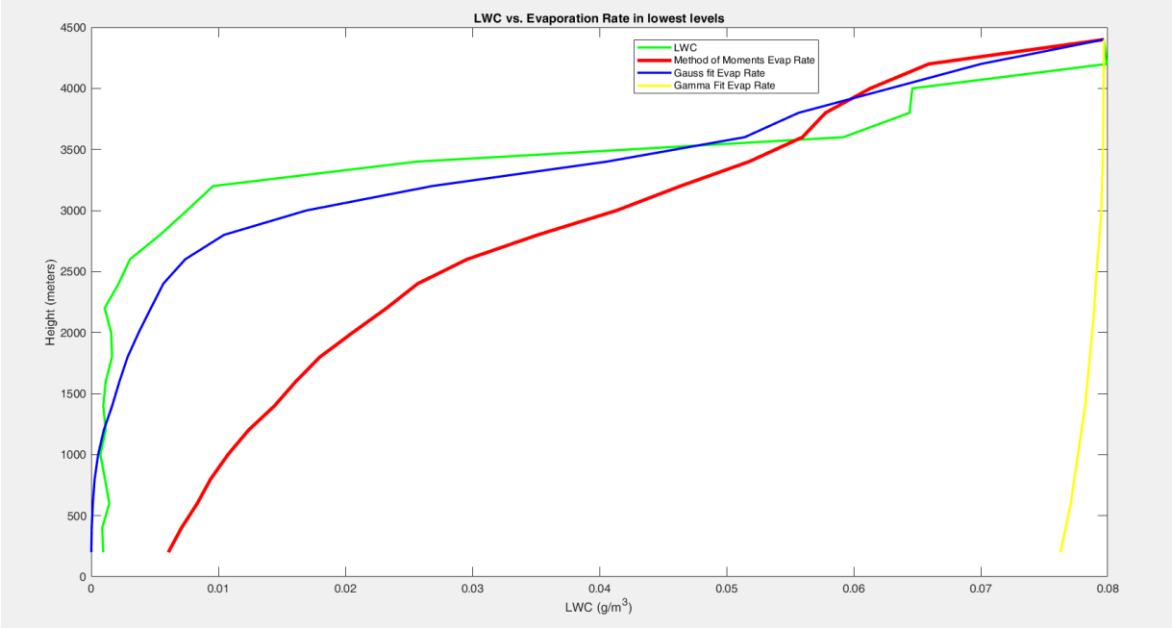

Figure 40 - The calculated LWC evaluated for the DSD methods over the height of the observed dry layer from balloon B. The observed LWC from the MRR is the green line, the Gamma DSD in yellow and the MOM DSD in red.

Figure 40 compares the modeled DSD evaporation rates in terms of the change in LWC to the LWC observed by the MRR. The closer the model is to the observed LWC the more accurate the evaporation quantification of the modeled distributions. The Gauss3 and the MOM in this case modeled the change in the LWC exceptionally well, slightly underestimating the rate of evaporation under 3 km and then slightly overestimating under 1 km. The Gamma distribution woefully underestimated the rate of evaporation through the height of the column. This is a result of the Gamma fitted data failing during the initial DSD quantification as shown in several instances in the following case studies.

3.1.2 October 5th, 2019 Balloon D Analysis

The next time of observed rainfall modeled is at 1930Z shown in Figure 37 as reflectivity values reaching the surface at 20dBZ-30dBZ. This coincides with the time that balloon D was launched and is used as the representative sounding in the next evaporation evaluation. The derived VM of the balloon was again included in the evaporation model and the base of cloud dropped slightly to 3.2 km. The evaporation model shows all drop diameters below 2.5 mm evaporating with the balloon derived VM. However, the laser disdrometer was in fact observing rain at the surface with diameters below 1.5 mm. This is a possibility as the drops between 2.5 mm and 3 mm decrease in diameter as they descend, however the concentration of those drops would be very small, and was not consistent with the concentrations observed at the surface.

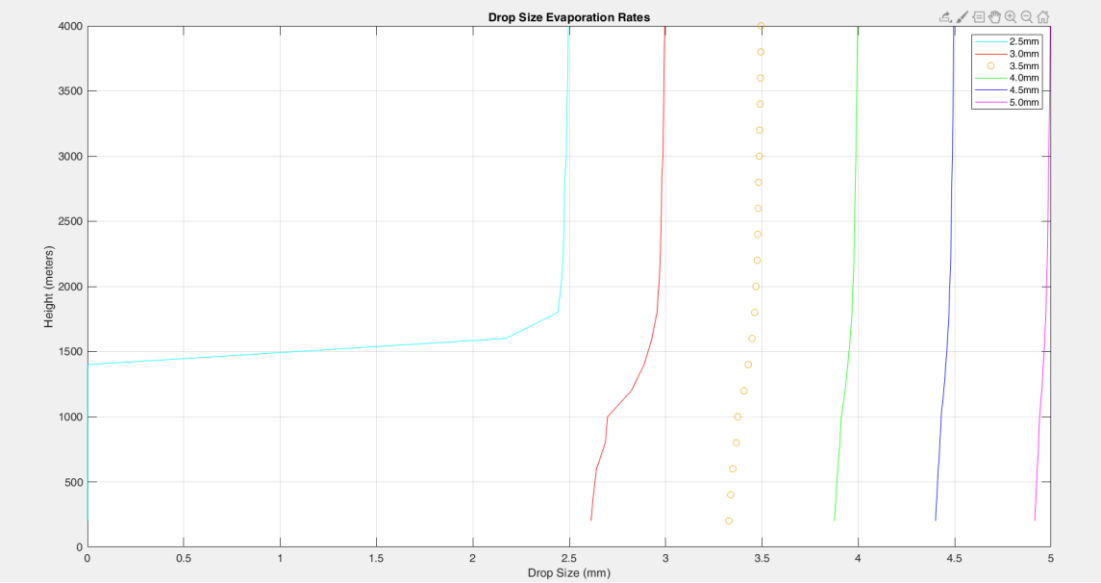

Figure 41 – The modeled evaporation rates of drop diameters given the balloon D environment including the balloon derived VM.

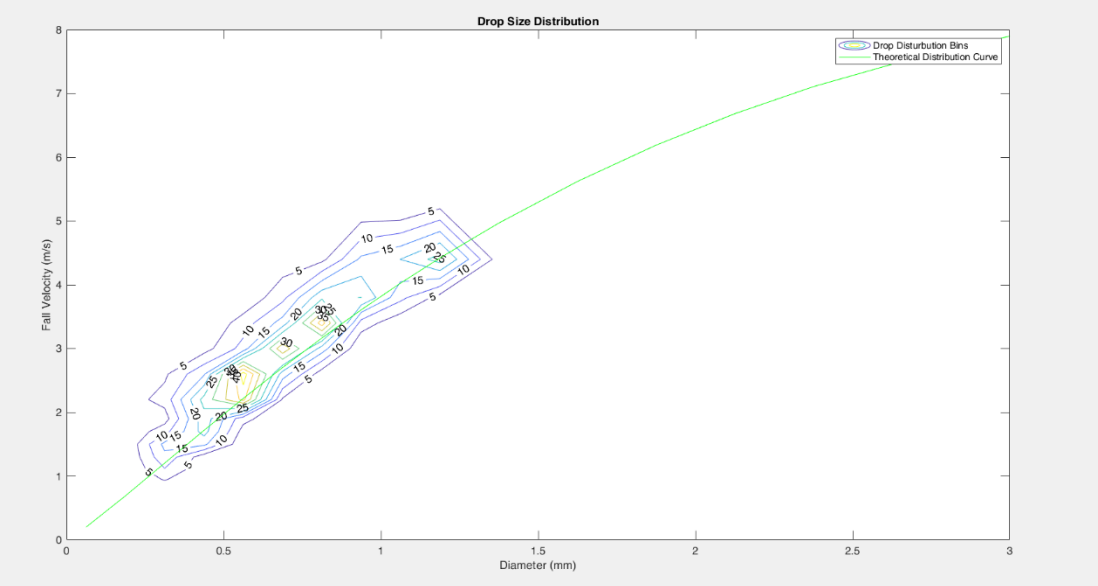

Figure 42 – Laser disdrometer observation of DSD at 1930Z for the October 5th, 2019 case study.

When the derived VM are taken out of the equation, the quantification becomes more representative of the observed distribution with drop diameters above the 1 mm surviving to the LOL reducing to just above 0.6 mm. It must be noted that drops between 0.75 mm and 1.0 mm will also survive to the LOL, but will change in diameter as they descend

from the cloud base, making the observed range of DSD's at the surface depend on the actual distribution from the fall height as demonstrated in Figure 43.

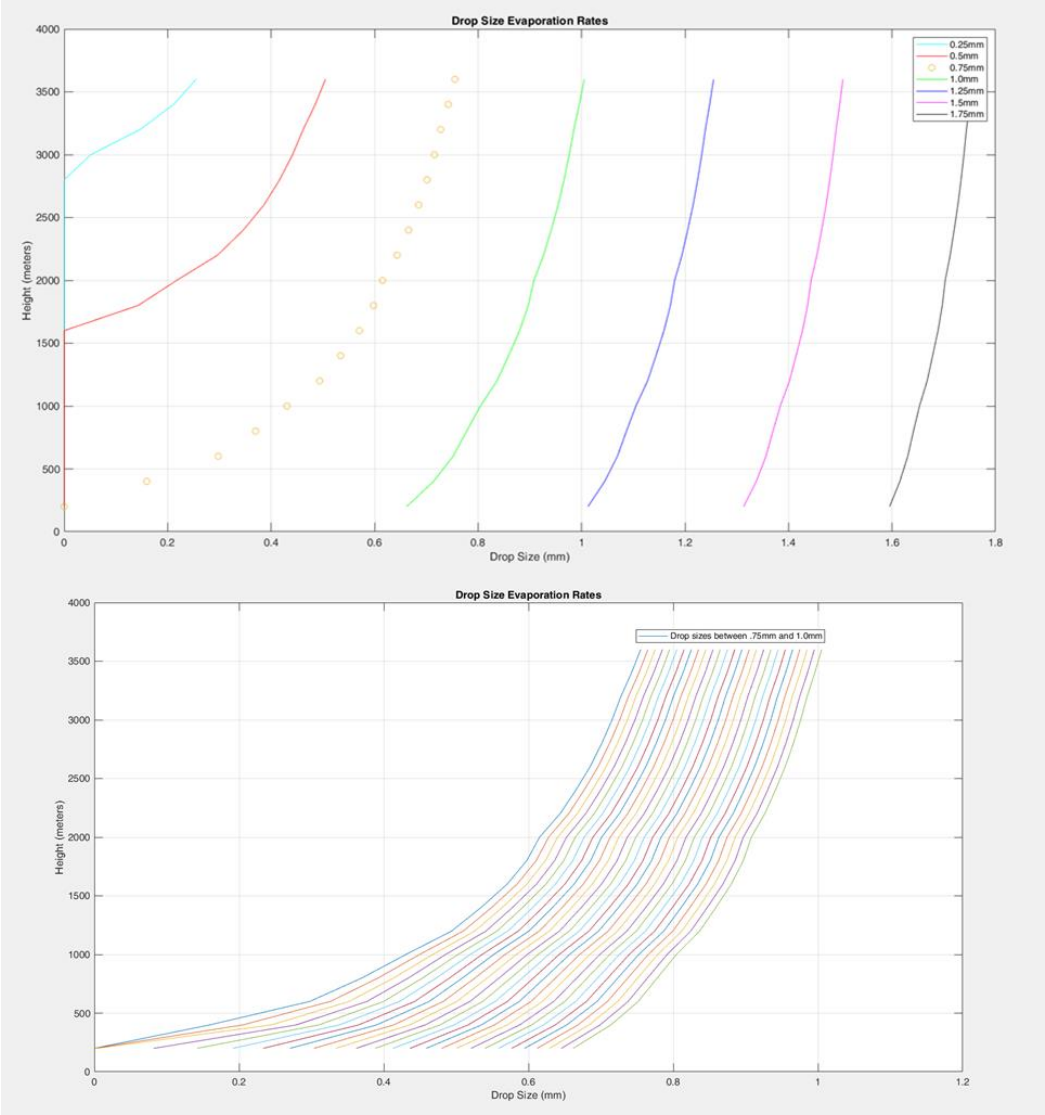

Figure 43 – The simulated drop evaporation with no VM for 1930Z balloon D sounding profile. The top chart displays the drop evaporation rate of drops in increments of 0.25 mm. The bottom displays the evaporation of drops in tenths from 0.75 to 1.0 mm. This is to demonstrate the range of possibilities for drops observed at the surface.

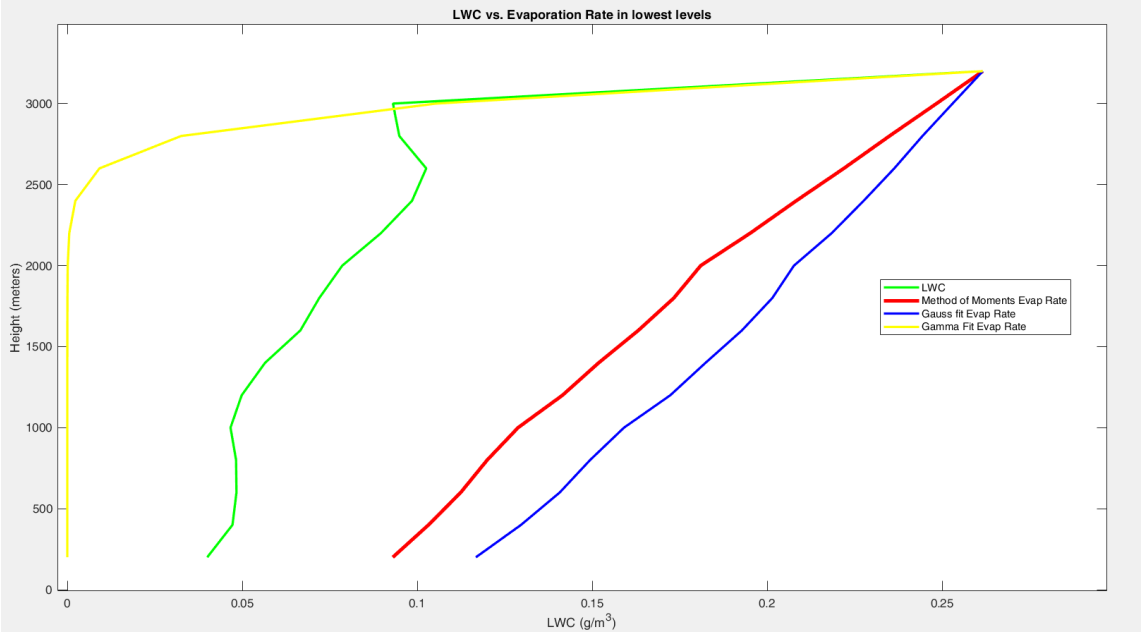

Figure 44 – The LWC calculations with modeled DSD using the balloon D sounding environment compared to the MRR observed LWC at 1930Z.

In Figure 44 the evaporation calculation of each modeled DSD is evaluated through the dry layer with no VM. The Gamma fit model overestimates the evaporation rate were the Gauss3 and the MOM underestimates the evaporation. The Gamma underperforms in this calculation as it poorly models the tail of larger drops observed by the MRR.

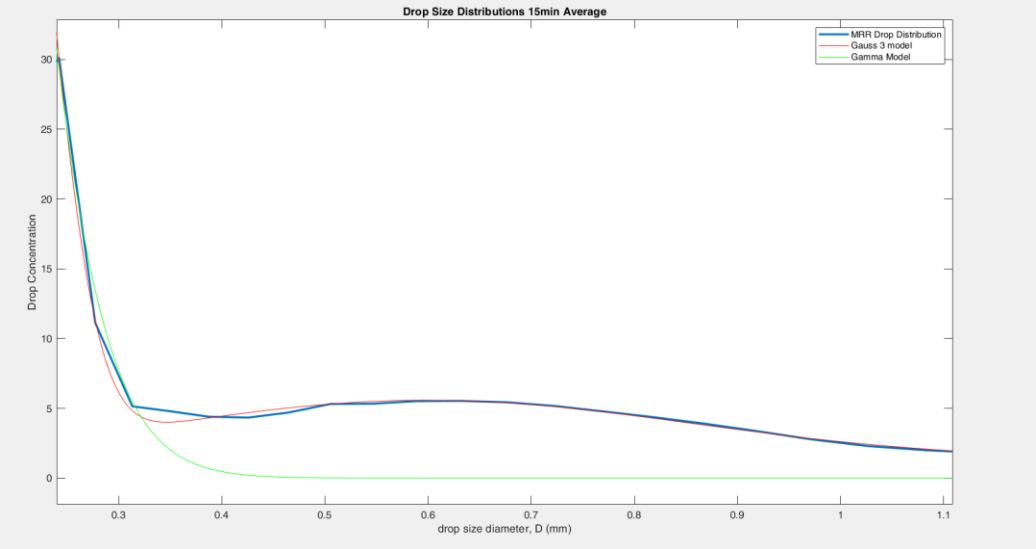

Figure 45 – Modeled and observed MRR drop concentrations for the Gauss3 and Gamma linear regression fit for 1930Z on October 5th.

The inaccuracy of the quantification can be described by several possible considerations. For the balloon derived VM, the convective environment with the onset of precipitation can affect VM due to different microphysical forcing. Factors such as surface convergence due to gust fronts and rain induced downdrafts and subsequent updrafts at differing areas of the balloon ascent within the layer can affect the perturbations of the balloon's ascension. Figure 44 assumes no VM with evaporation rates and as shown before, VM is a clear factor in the overall quantification. However, by further averaging the derived VM of the balloons, a much closer LWC can be observed for the Gauss3 and the MOM. The sounding derived VM were averaged over the dry layer to 0.21m s^{-1} upward ascent and put into the model. The cloud base was also lowered by 200 meters, based on the observation at KCOU.

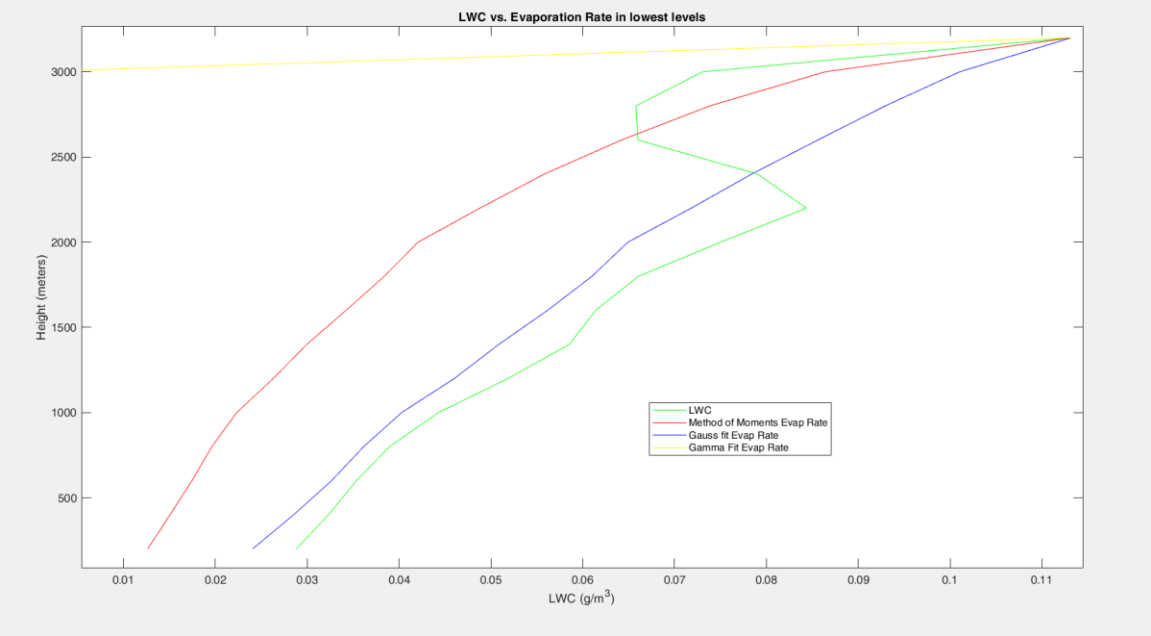

Figure 46 – Averaged total VM of 0.21m s^{-1} included for the evaporation quantification over the height of the dry layer at 1930Z.

The results show the Gauss3 distribution has now very closely matched the observed LWC of over the depth of the column. The MOM is overestimating the total evaporation quantification suggesting that the proportions of the DSD for the Gauss3 are better representative of the real atmosphere. The laser disdrometer raw calculation observed 0.025g m^{-3} corresponding with the observation at the LOL calculated by the Gauss3.

3.1.3 October 5th, 2019 Modeled Environment Analysis

Comparing the model derived environmental profile to the evaporation quantification of the observed sounding presents some issues for this case study. The most accurate model data available was the 31hr 12Z NAM forecast from October 4th, 2019[2]. In comparing the forecast sounding to the observed, the dry layer is significantly

[2] Newer model data would be a better representation for this analysis, however due to the global pandemic, access to gridded model data is limited to data saved in the local hard drive.

more pronounced immediately below the cloud base seen in Figure 47. This results in all drops under 3 mm completely evaporating before reaching the surface. For this purpose, a full analysis of the comparisons to several model outputs was examined in the next case study.

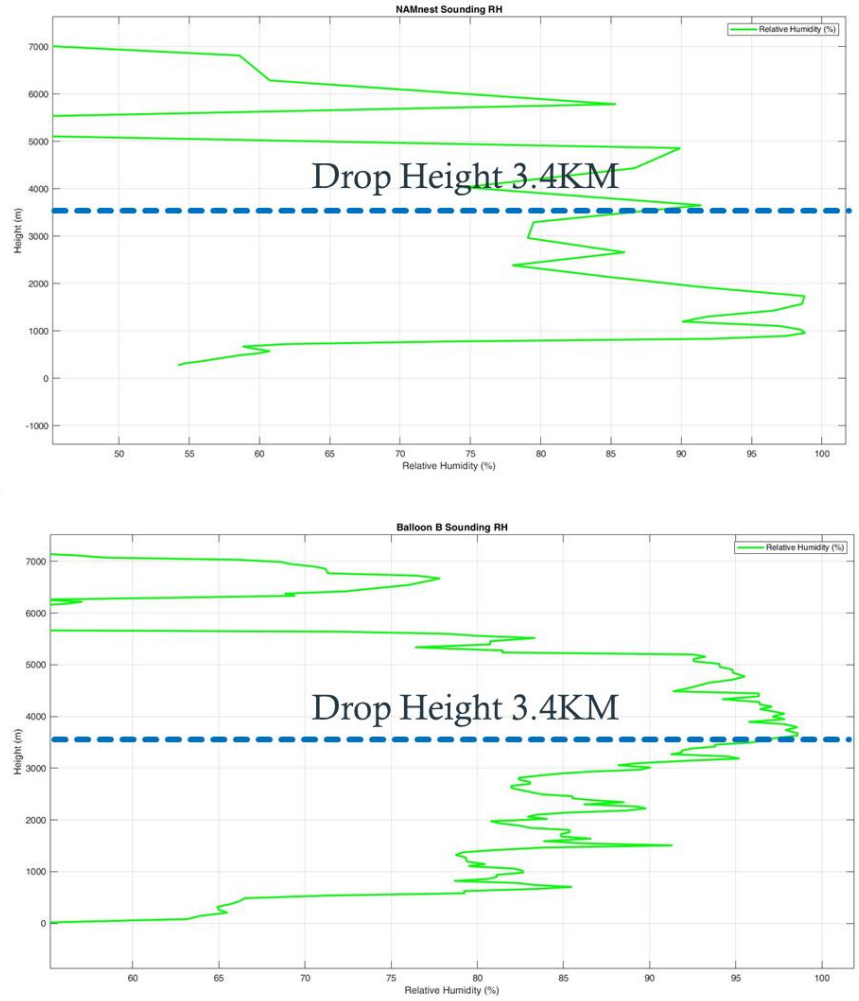

Figure 47 – Compares the relative humidity profile of the 31hr 12Z NAM forecast to the observed vertical profile of the balloon D launch.

3.2 November 21st, 2019 Case Study

On November 20th, southwestern gradient between a stagnant surface high pressure system centered over the Ohio River Valley and a maturing baroclinic low over

the Kansas/Nebraska border began to strengthen the advection of low-level dry air. Precipitation was anticipated ahead of the frontal passage as the low moved to the northeast, increasing the moist air advection as the surface high also shifted east and weakened. A deep dry layer extending up from the surface was observed on at KSGF 12Z sounding, with forecast models projecting a zipper like saturation of the layer as the precipitation evaporated from the top down and saturated the profile.

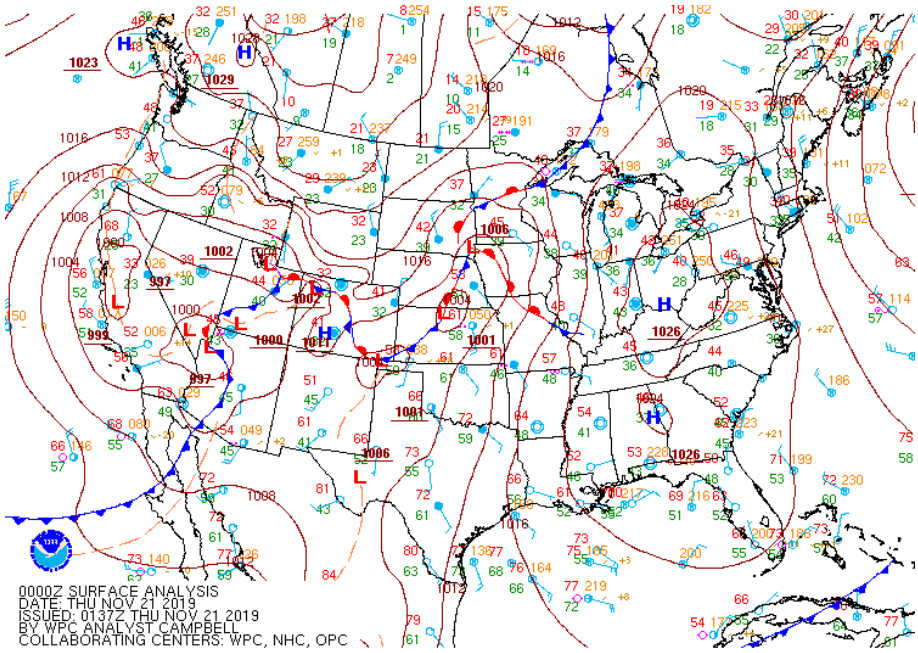

Figure 48 - Surface map analysis on November 21st at 00Z.

KLSX and MZZU observed precipitation returns falling into the dry layer above the Bradford Farm Research Center and the MRR observation showed precipitation with returns up to 20 dBZ falling into the layer and dissipating before they reached the ground from 00Z to around 01Z. Further examination of the MRR observation depicts fall velocities above 2.6 km at 1-2 m s^{-1} and then increasing to 4 m s^{-1} below this level. This

transition of fall speeds is consistent with the melting layer and will be the baseline for the evaporation calculation.

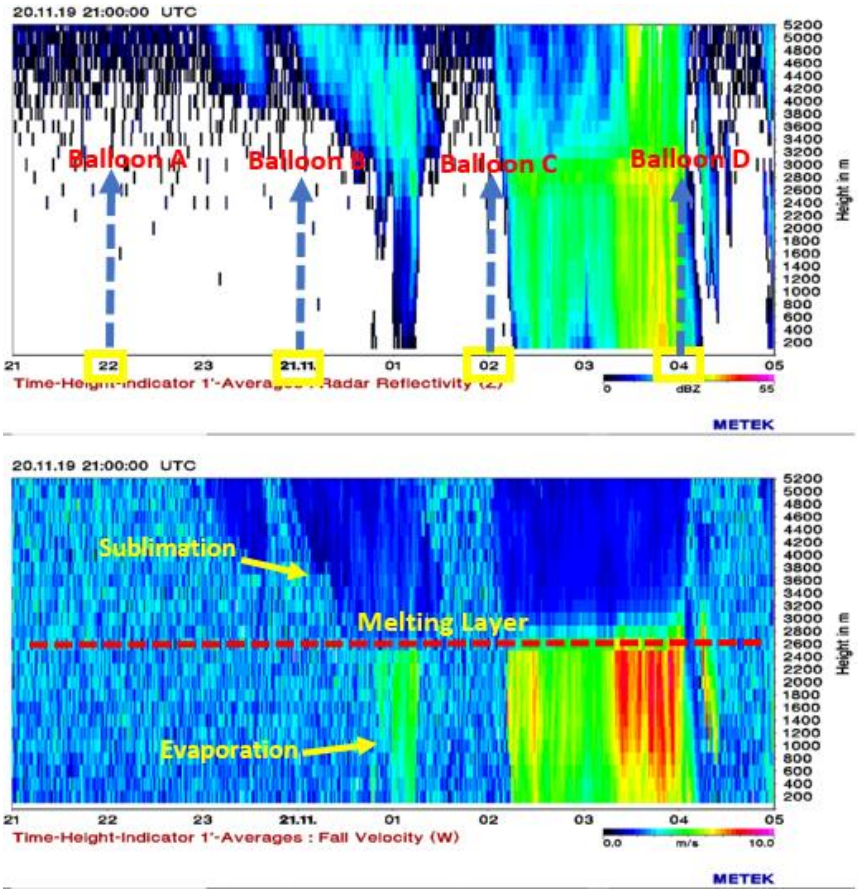

Figure 49 – Reflectivity (top) over a time height profile for November 21st, 2019 displaying the times observational soundings were taken. Fall velocity (bottom) over a time height profile at the same time highlighting the melting layer, areas of sublimation and areas of evaporation between 00Z and 01Z.

Given that the melting layer was below where most of the precipitation returns are fading in Figure 49 from 00Z to 0045Z, what is likely occurring is sublimation. Fall velocities consistent with rainfall were observed after 0045Z below the melting layer and remained as such for the rest of the duration of the observational period. Balloon A was not examined for the following case study as the rain periods were temporally closer to Balloon B. Sublimation was saturating the environment, the quantification of which would be an area for future study. Balloon B was used to examine the evaporation

occurring at 0100Z, Balloon C was used to examine the evolution of the drop distribution starting after 02Z and Balloon D was used for evaporation rates for precipitable returns between 04Z and 05Z. Model soundings were also used to compare how the evaporation quantification changes from a variety of different model resolutions. VM derived from balloon ascent rates were also assessed in the calculations.

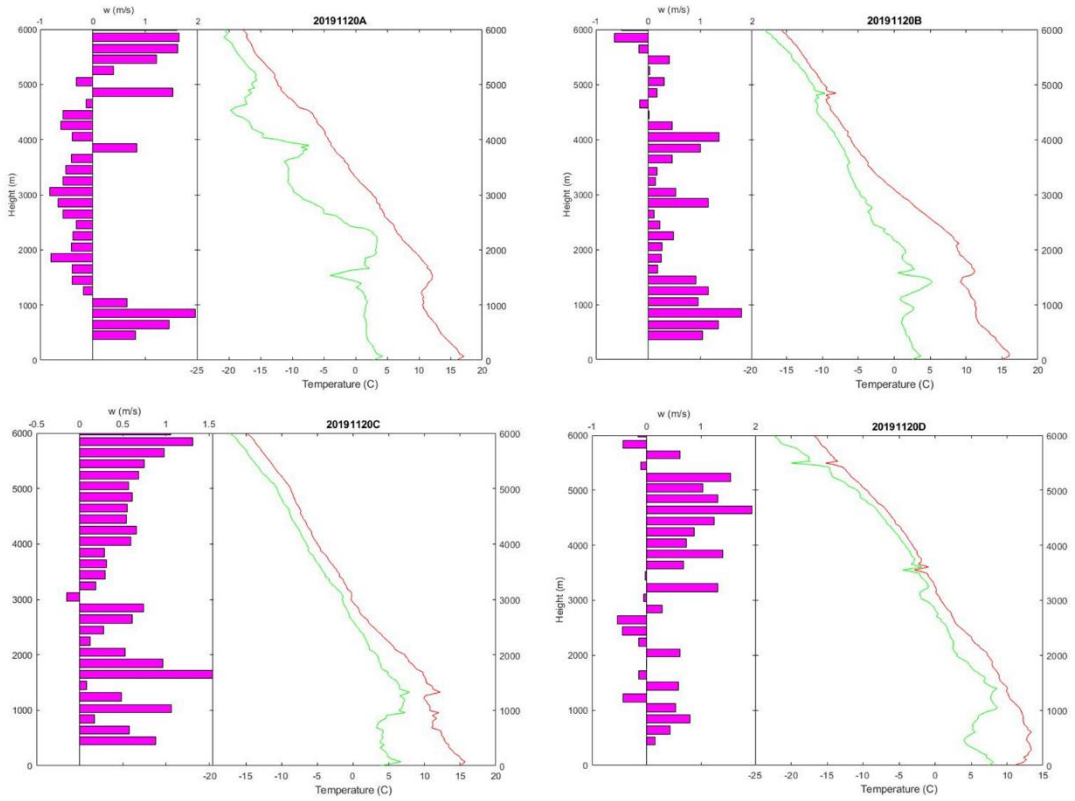

Figure 50 – The low-level atmosphere temperature and dewpoint profiles for the each of the 4 balloon observations as well as the derived VM for each layer. Balloon A was taken at 2200Z, Balloon B was taken at 00Z, Balloon C was taken at 02Z and Balloon D was taken at 04Z.

Figure 50 displays the atmospheric profiles of the four observations. They expressed the same trends that were observed with the forecast model guidance. A zipper like pattern emerged as the temperature profile came together with the dewpoint profile over times of the observation. VM trends relatively symbiotic with the adiabatic trends of the profile, as upward VM dominated the lower atmosphere and the profile increased in

saturation with height. Balloon D deviated slightly from the trend as downward motions were observed, likely as a result of precipitation.

3.2.1 November 21st, 2019 Balloon B Analysis

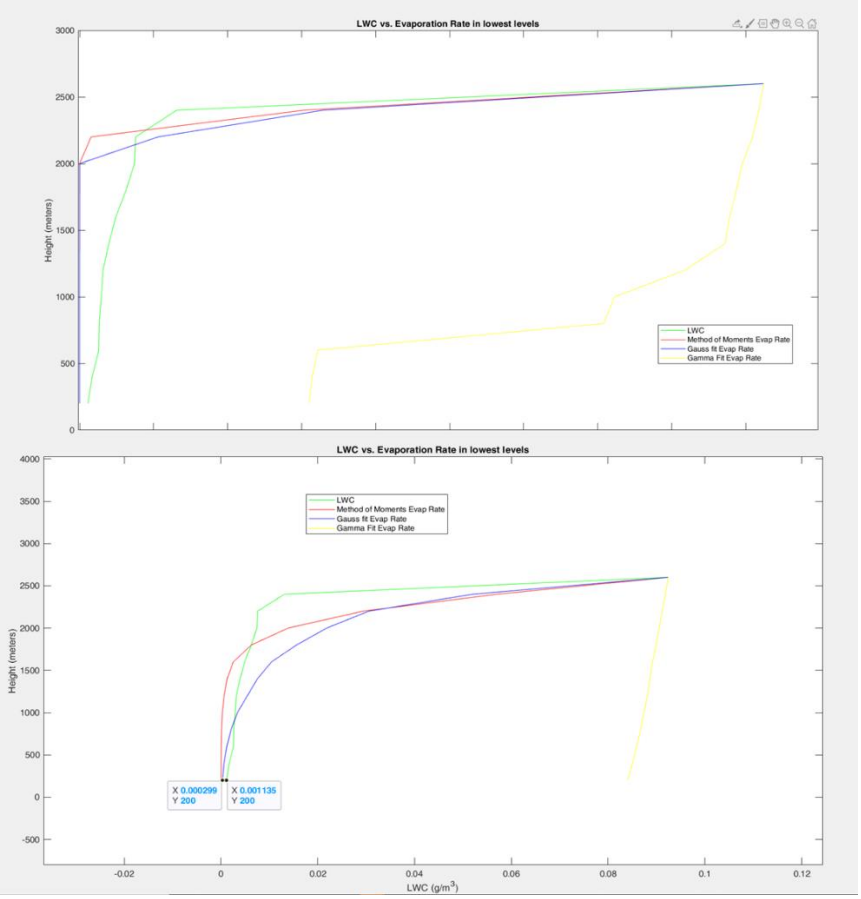

Figure 51 – (Top) The balloon derived evaporation quantification for the various DSD models. (Bottom) No VM assumed evaporation quantification.

Figure 51 shows the evaporation model with the derived vertical winds for the first case at 0100Z. The Gauss3 and MOM distributions closely represent the MRR evaporation, especially directly below the cloud base. The Gamma fit underestimates the evaporation rates giving 0.03 g m^{-3} of LWC at the LOL. After examining the modeled DSD of the Gamma MRR fit, the fitted model was flat, meaning the fit did not express drop distributions. This explains its poor performance in quantifying the evaporation

rates as there are no drops to differentiate the evaporation from the observation layer. Including VM the Gauss3 and MOM DSD models take the observed LWC to 0 g m^{-3} at around 2 km, closely matching the rate of evaporation above that level then overshooting the rate at that level accelerating to zero. The laser disdrometer observed DSD's with a calculated LWC of 0.002 g m^{-3}.

Changing the derived vertical wind profile to the average motion gives an upward velocity at 0.65m s^{-1}. This increases the Gamma LWC at the LOL and increases the height that the Gauss3 goes to 0 g m^{-3} at 2.4 km. With no VM in the calculation, the Gamma continues to overestimate the LWC at the LOL. The Gauss and MOM do not follow the evaporation rates observed above 2 km, however it closely represents the observed LWC below the 2 km, with the MOM going to 0 g m^{-3} at 1 km and the Gauss3 staying just above 0 g m^{-3} at the LOL. While this is not an exact match, the evaporation rates were well quantified.

In this evaporation account, the Gauss3 made the best estimations of the evaporation rate quantifications. With the VM, the Gauss3 evaporation rates matched better above 2 km but then overestimated the quantities. With no VM, the Gauss3 matched the observed better below 2 km and underestimated the rates above. The MOM did similarly well in its estimations. The Gamma fit DSD was flawed from the beginning overestimating the MRR DSD and so maintained underestimated evaporation rates. No VM included was better suited for this model in quantifying the overall rate of evaporation for the Gauss3 and MOM.

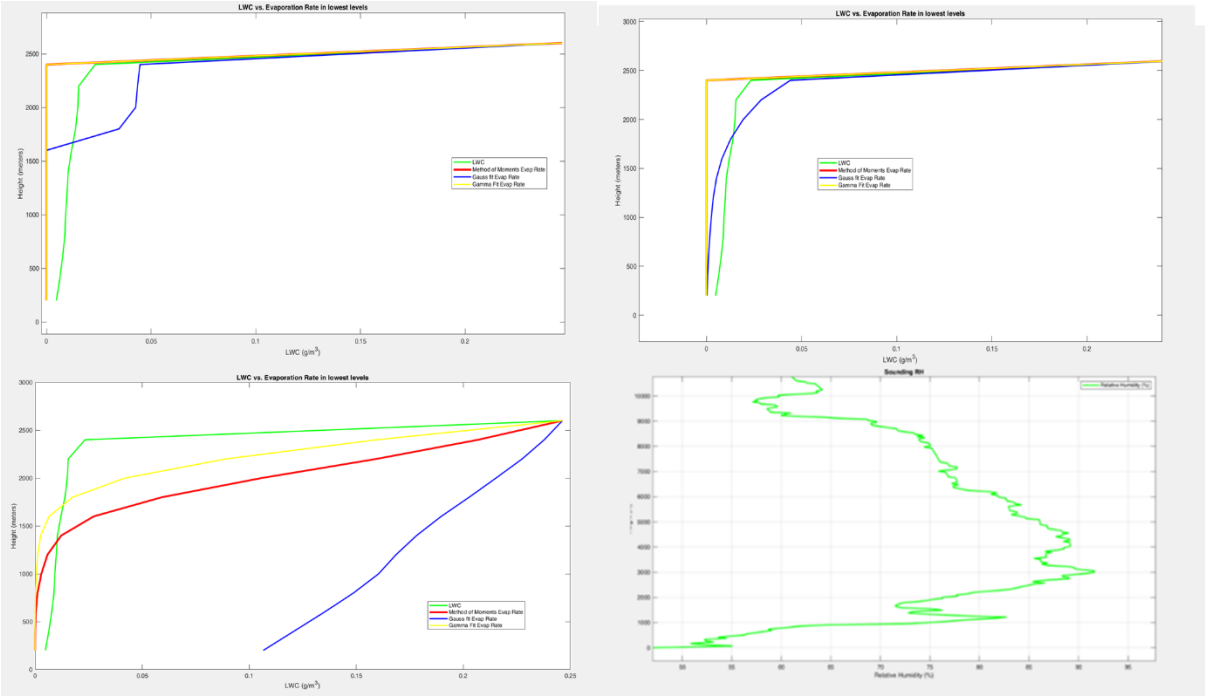

Figure 52 - Evaporation model evaluation from precipitation onset at 0210Z with balloon C sounding. Top left chart is evaporation with derived VM, top right is the average derived VM for the layer, and the bottom left is the evaporation quantification with no VM. The bottom right is the RH profile for balloon C.

3.2.2 November 21st, 2019 Balloon C Analysis

The next quantification was with the onset of the first large wave of precipitation at 0210Z (Figure 52). Balloon C was used in this case and was launched 20 minutes before the onset of precipitation. Adding the balloon derived VM resulted in an overestimation of evaporation for all the DSD models. Gauss3 had a lower evaporation rate in this instance, underestimating immediately below the cloud base, then overestimating above 1.5 km. Gamma and MOM match the evaporation rate immediately below the cloud base, but overestimate the total evaporation.

Using the average of the derived VM at 0.6 m s^{-1} gave better results for the Gauss3. This resulted in evaporation rates closely following the MRR observed throughout the dry layer. Gamma and MOM overestimate the LWC calculations rapidly

decreasing the quantification to 0 g m^{-3} at the same place as with non-averaged VM. Using no VM resulted in the Gamma and MOM having a more representative evaporation rates while Gauss3 underestimates the rate.

In evaluating the overall performance of the three models in this scenario, it is a bit less clear how the models performed given the inconsistencies in the vertical motion quantification. Given that there was at least some VM in the atmosphere at that time, it would appear Gauss3 had the better quantification. Average VMs were later adjusted in the model to find the best LOL quantification for each DSD model. The best VM for Gauss3 was 0.45 m s^{-1} where 0 m s^{-1} VM was the best quantity for the other two DSD models. This tactic was explored further in the next case studies to determine if any relationship can be made.

3.2.3 November 21st, 2019 Balloon D Analysis

Balloon D was evaluated for the rain occurring after 0400Z. The MRR depicts precipitation returns below the melting layer completely evaporating at 800m between 0410Z and 0425Z. The Laser disdrometer does show some drops making it to the surface with an LWC of virtually 0 g m^{-3}.

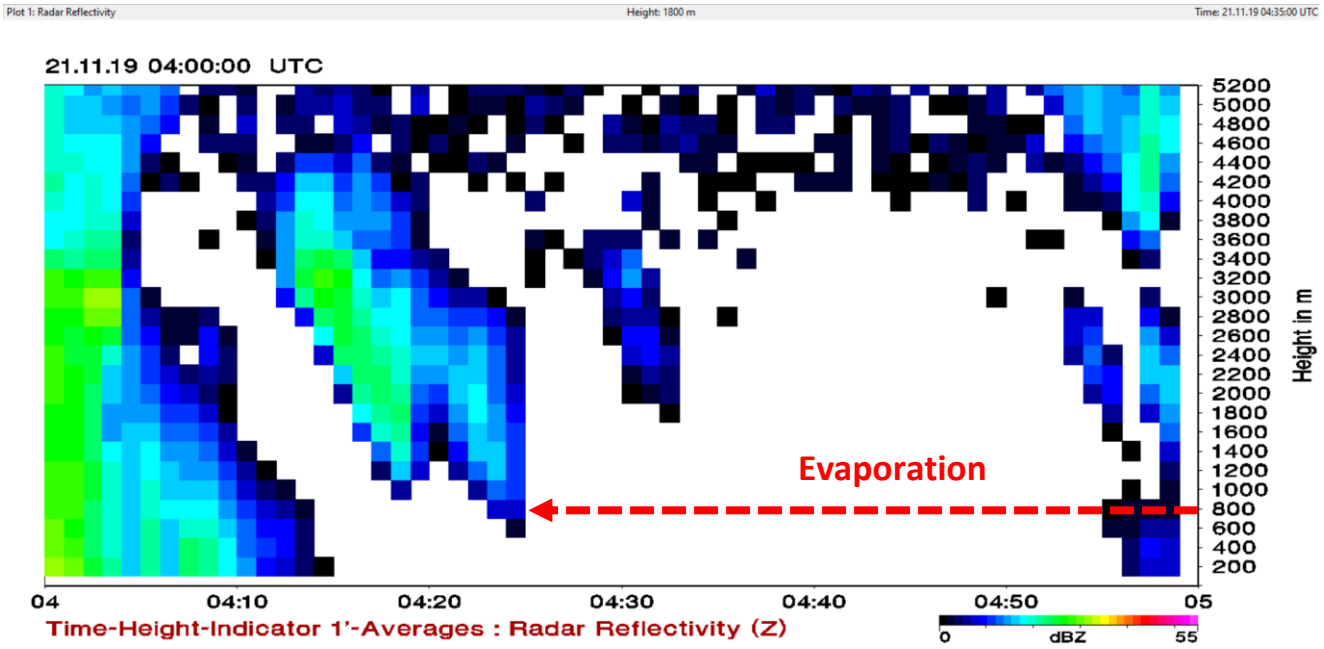

Figure 53 – MRR reflectivity with evaporation between 0410Z and 0420Z as seen by the precipitable returns dissipating above 800m.

The results depict two of the DSD models handling the evaporation well, while the Gamma fit model once again underestimates the rate due to another over quantification of the fitted MRR distribution. Both the Gauss3 and the MOM converge to zero on almost the same trajectory at 2 km with derived VM included and overestimate the evaporation rate for the entire column. With an averaged derived VM of 0.16 m s^{-1} the Gauss3 and MOM are more representative carrying LWC to just under 1 km, slightly overestimating the evaporation rates. With no VM, both MOM and Gauss3 underestimate the evaporation rate through the column until 0.75 km, then overestimate the evaporation rate. The Gauss3 and MOM both show a good correlation to the observed MRR LWC in the three VM quantities, but using no vertical motions was best suited.

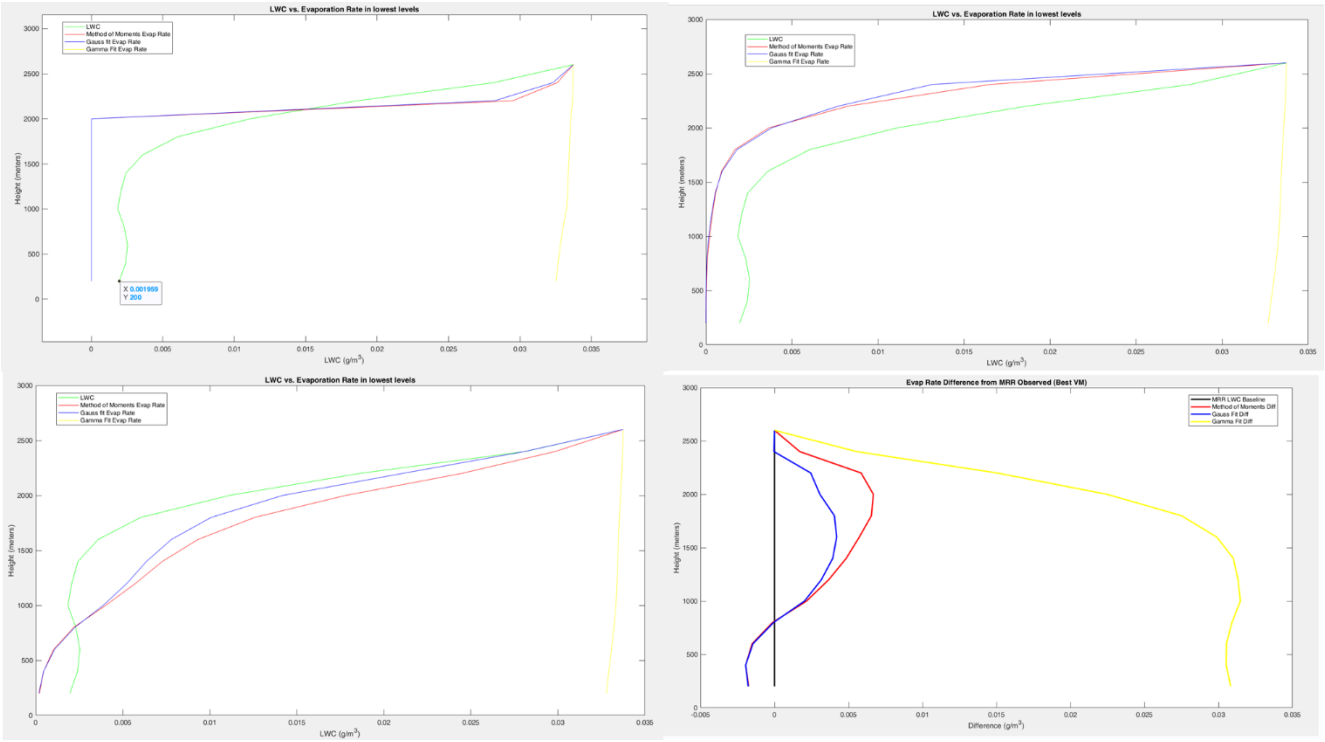

Figure 54 - Evaporation model evaluation from precipitation at 0415Z with balloon D sounding. Top left chart is evaporation with derived VM, top right is the average derived VM, and the bottom left is the evaporation quantification with no VM. The bottom right is the difference through the height of the dry layer of each DSD fit. The black line at zero represents the MRR evaporation rate, the Red line is the MOM difference, the blue is the Gauss3 difference and the yellow is the Gamma fit difference. If the DSD method is to the right it is underestimating evaporation rates, if it is to the left, it is overestimating. The closer to the zero a DSD fit is, the better it quantifies evaporation. This chart assumes the best VM estimation quantity at the LOL. In this case it was zero VM.

Since the Gauss3 and the MOM overestimate the evaporation rates and depict no LWC at the LOL with no vertical motions, finding the best VM was unnecessary in this case. The bottom right chart in Figure 54 shows that the Gauss3 best matches the observed evaporation given the best VM quantification, which in this case is none.

Assessing the overall performance for the three DSD models, the Gauss3 was the most representative. The Gamma fit DSD overestimated the number of drops in two of the three instances, creating poor correlations, and the MOM also performed equally as well as the Gauss3 in the scenarios where the MOM was calculated. Including derived VM often caused the models to overestimate the rate of evaporation, and not including

the derived VM caused an underestimation through most of the dry layer that would overcorrect closer to the LOL. Using an average VM brought the DSD fit quantities closer through the depth of the column.

3.2.4 November 21st, 2019 Modeled Environment Analysis

The next phase was to determine if model soundings can work as well as the observed soundings for evaporation quantification. In the case scenario from October 5th, 2019 the RH profile was the factor that had the most control of the evaporation rates throughout the dry layer. This suggests that the most representative low-level RH profile will have the best results in quantifying evaporation. For this case study, the DSD models worked best with the 0400Z balloon D sounding with no VM in quantifying the evaporation and was the best suited for the model sounding comparison. A variety of model sounding RH profiles were examined, and the closest modeled profiles to the balloon D was tested in the evaporation quantification.

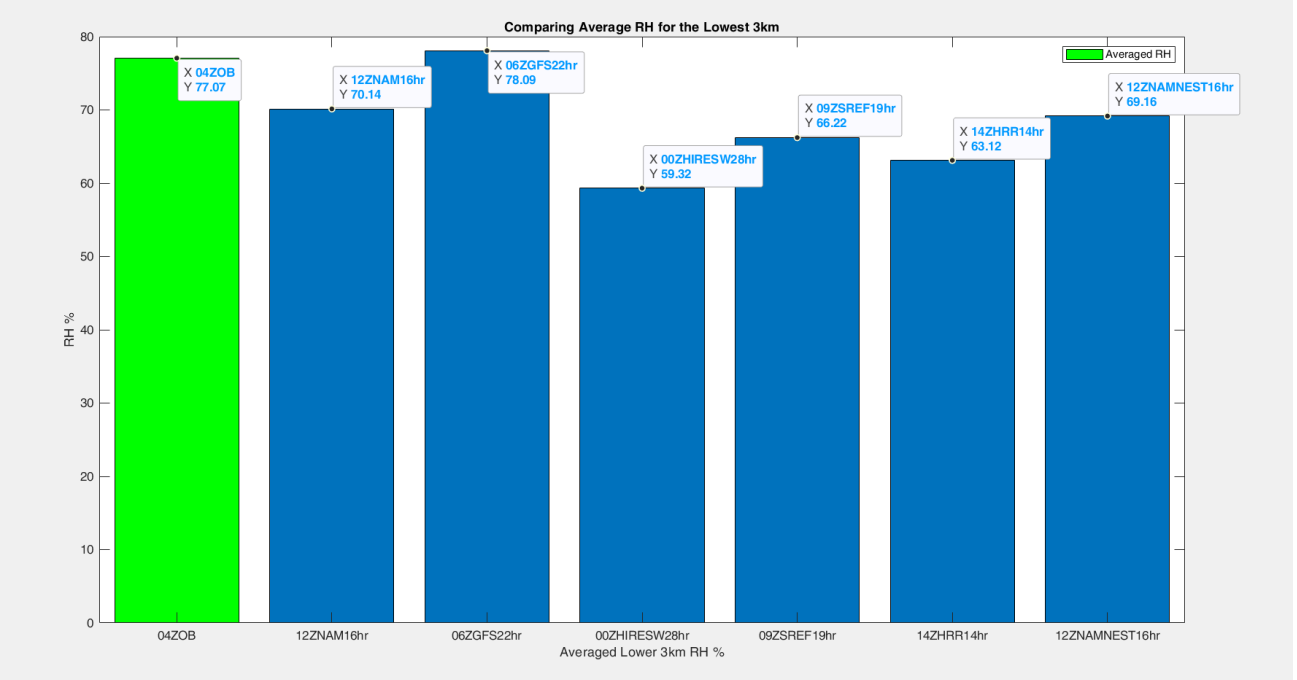

Figure 55 – Averaged lower 3 km RH comparison for 6 common model outputs used in precipitation forecasting taken at 0400Z. The closer the value to the balloon output, the better the perceived performance in the evaporation model as a representative atmosphere.

Six forecast sounding RH outputs were used to compare to balloon D. The soundings that were used were gathered at 14Z on November 20th and are the closest model outputs that are available at this time[3]. Figure 55 shows the average RH in the lower 3 km for all model outputs. The green bar is the observed sounding with an average lower 3 km of 77% RH. The two closest model outputs to the observed were the 06Z 22hr run of the GFS at 78% RH and the 12Z 16hr run of the NAM at 70% RH. The other models' RH averages were well below the observed sounding and when run through the simulation produced an overestimation of the evaporation quantification.

[3] These model runs were closer to the observed time than in case 1, but are still not ideal for evaluating the high-resolution model profiles with the evaporation quantification.

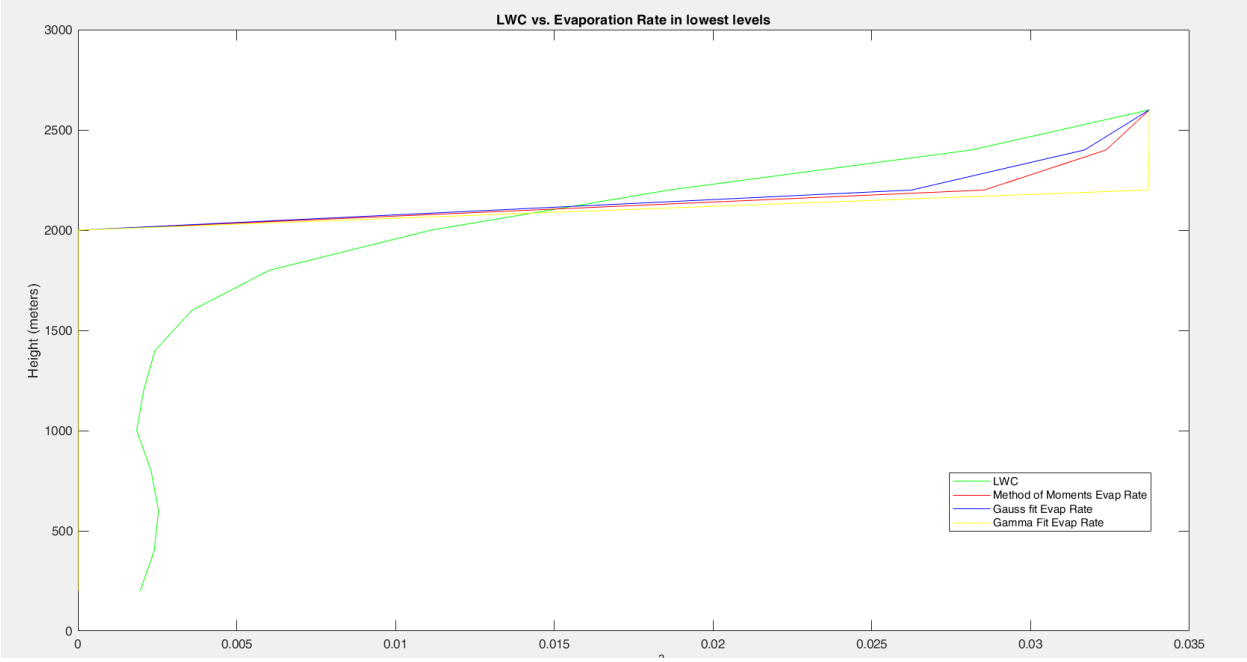

Figure 56 – Evaporation model with no VM through the 06Z 22 hour run of the GFS forecast sounding.

Figure 56 illustrates that the GFS overestimates the evaporation rates, converging to zero LWC at 2 km.

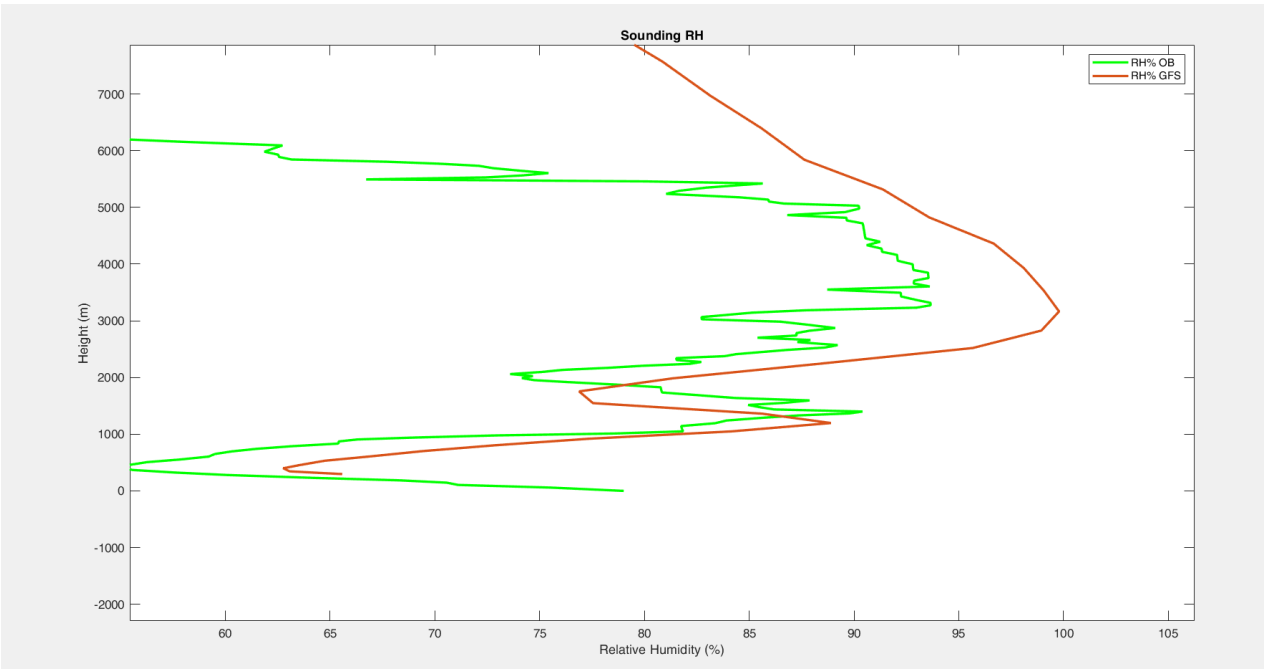

Figure 57 – The GFS sounding profile compared to the observational sounding.

Comparing the GFS sounding to the real time sounding depicts overall model agreement as Figure 55 indicates with the observed sounding RH in the lower levels. However, the slightly dryer air at 2 km significantly changes the evaporation rates in this quantification.

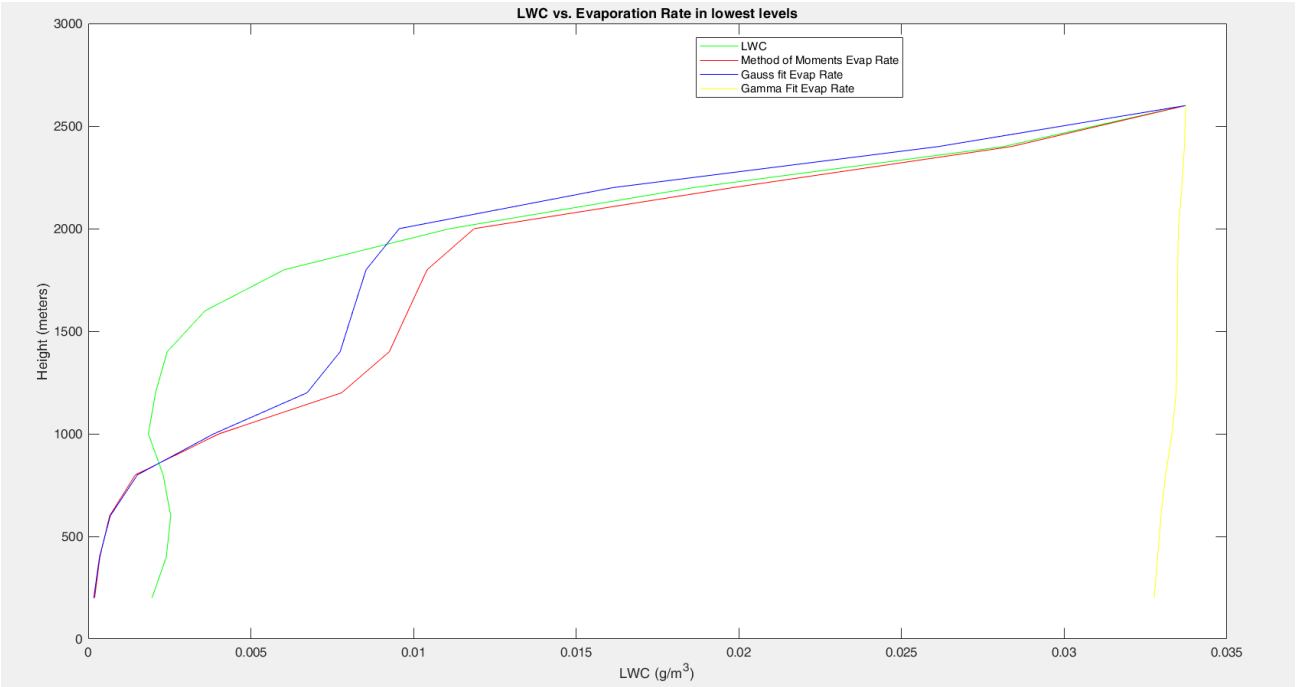

Figure 58 - Evaporation model with no VM through the 12Z 16 hour run of the NAM forecast sounding.

The 12Z NAM 16hr forecast environment was run through the evaporation model shown in Figure 58. This model environment quantified evaporation much better than the GFS forecast sounding, following the observed evaporation rate closely from the cloud base to the LOL.

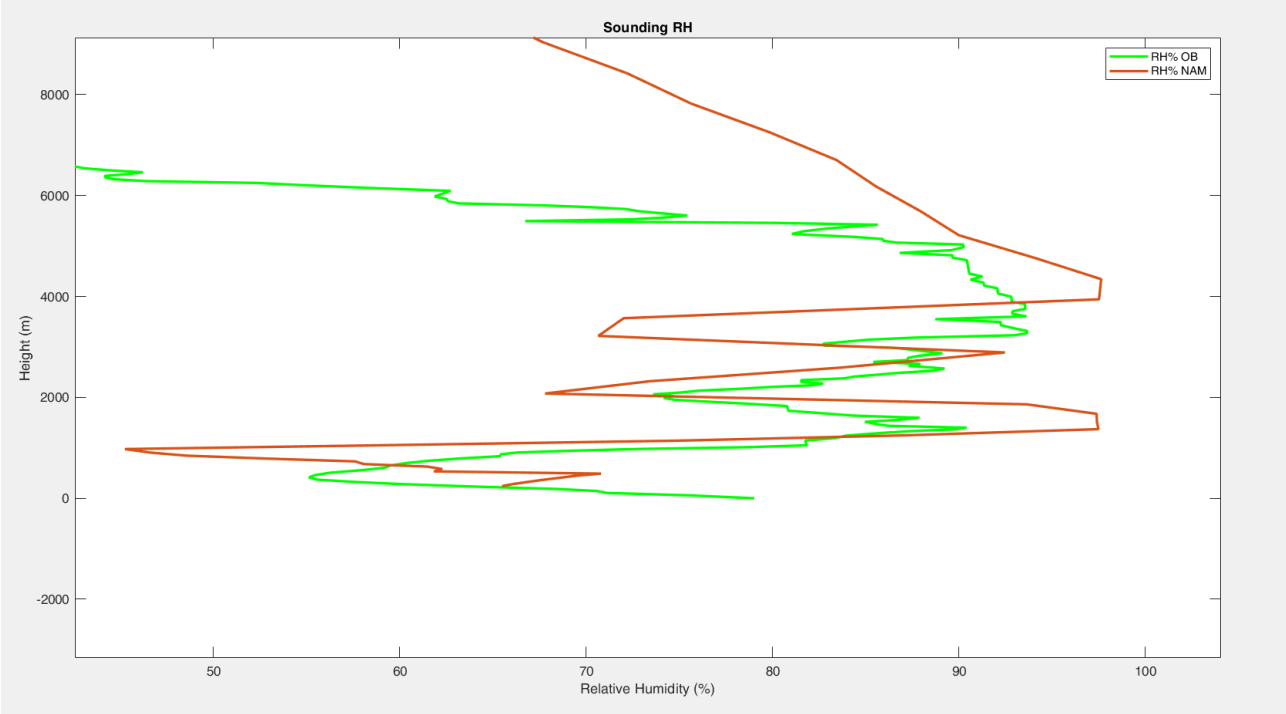

Figure 59 - The NAM sounding profile compared to the observational sounding.

The NAM sounding in Figure 59 as compared to the GFS in Figure 57 has a much higher resolution (more data points) and the RH profile aligns better with the trends of the observed sounding. Higher levels of saturated air below 2 km in the NAM create an under estimation of the evaporation rates observed in Figure 58, and drier air below 1 km creates a slight overestimation of evaporation. However, the NAM model best represented the quantification of all the six forecast soundings and had very similar results to the observed sounding in Figure 54. Although the average RH profile matched the GFS better, levels at which the air is saturated or unsaturated, the level and the depth of that saturation plays a large role in the overall quantification of evaporation. Models with higher resolution in the lower levels unsurprisingly work better, although not in instances of longer-range forecasts as the higher resolution HIRESW, HRRR, and RAP

overestimated the dry air and subsequent evaporation rates. More cases will need to be evaluated with forecast model guidance that are closer to the precipitation onset times.

3.3 March 09th, 2019 Case Study

On March 09th, 2020 a Colorado surface low developed on the leeside of the Rockies while a strong high-pressure center resided off the coast of North Carolina. Increasing southwest gradient flow between the high and developing low pressure systems increased the dry air advection into mid-Missouri. Forecast precipitation was expected around 08Z ahead of the front and was observed on the radar at KMCI at 0300Z as the system approached from the west. The 00Z observed sounding from Topeka, Kansas indicated a significant dry layer from the surface to 4 km as did the 00Z Springfield, MO sounding.

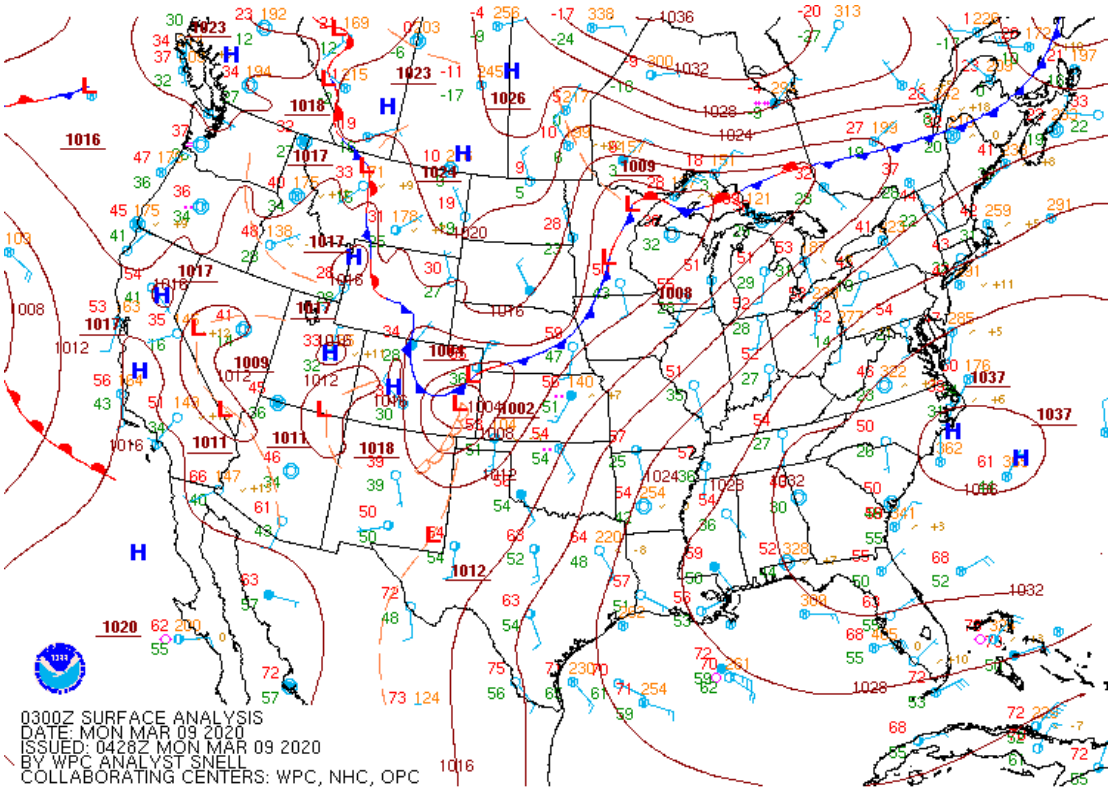

Figure 60 – Analyzed surface chart depicting strong SW gradient indicating dry air advection in the lower levels.

Three balloons were released, the first Balloon at 06Z, the next at 08Z and the last at 0930Z.

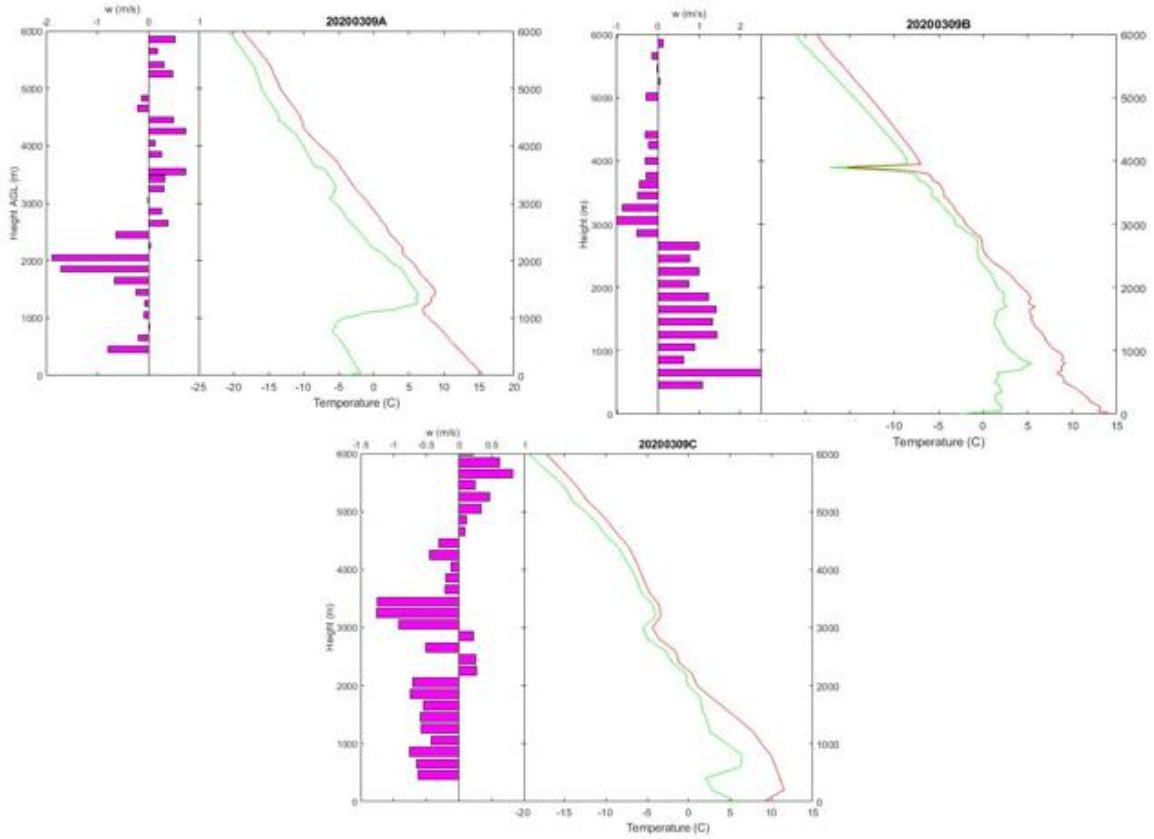

Figure 61 - Three observed soundings and the derived VM of March 9th, 2020. Balloon A was sent up at 06Z, Balloon B was sent at 08Z and Balloon C was sent at 0930Z.

The vertical motions did not trend as well as previous cases given saturating profile. All the balloons were launched in precipitation. From the previous case studies, balloon derived vertical motions in precipitation have skewed the results of the evaporation quantities, and the adiabatic trends have not matched the balloon ascent. They were assessed in these cases to a lesser extent.

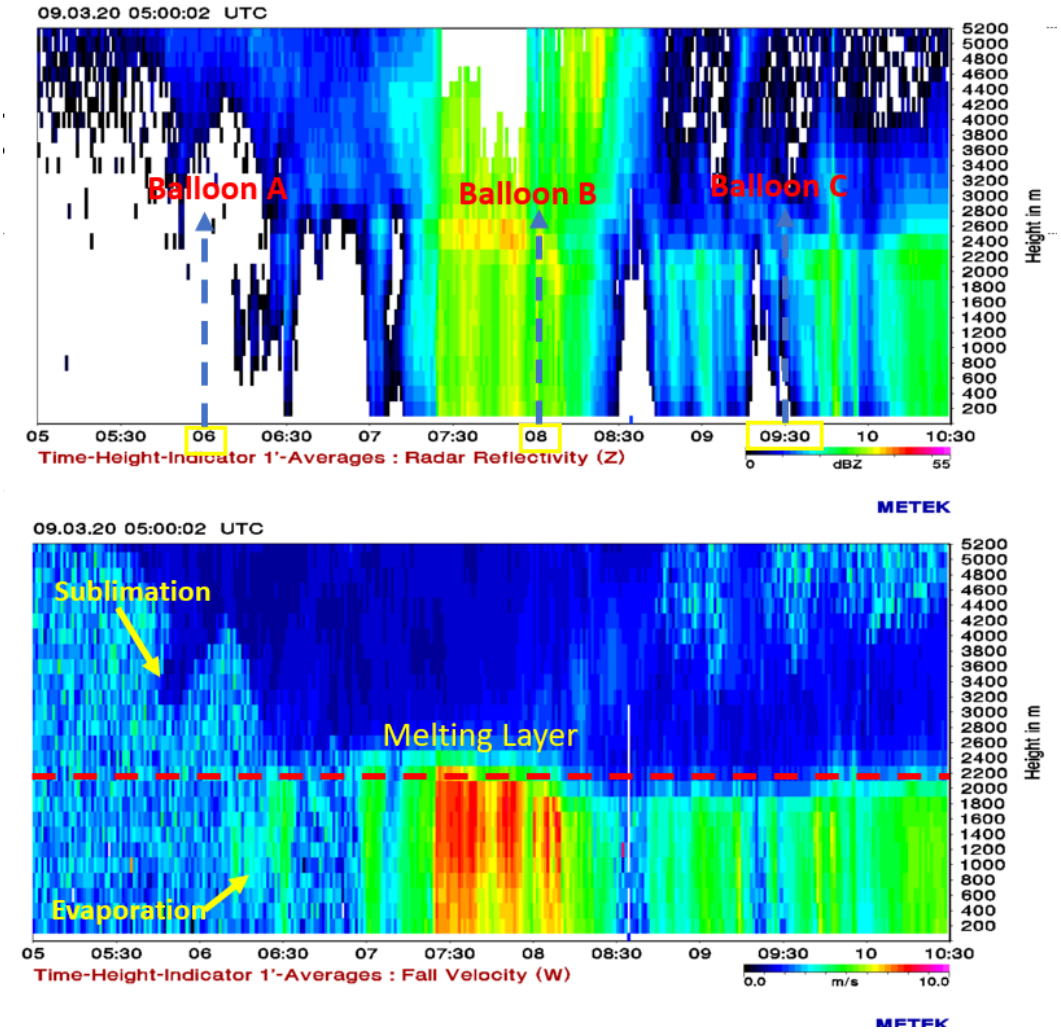

Figure 62 – (Top) The reflectivity image depicts the times of Balloons A,B and C, and that light precipitable echoes were diminishing before reaching the surface. (Bottom) The fall velocity image shows the melting layer around 2.2 km with sublimation occurring before 0600Z and evaporation occurring after the first balloon launch at 0600Z.

The radar images from the MRR show a healthy amount of evaporation occurring over the radar as the system progresses. In the heaviest rainfall indicated by the higher reflectivity values between 0715Z and 0845Z, the fall velocities decrease, indicating that drop diameters are shrinking with evaporation. The melting layer observed from this case was assessed at 2.2 km as the fall speeds increased above 2 m s^{-1} at this height. This served as the base height for the evaporation quantification as the cloud base was observed well above this level at 4 km.

3.3.1 March 09th, 2019 Balloon A Analysis

The first time examined in this case study was after balloon A's launch between 0600Z and 0630Z. Evaporation was being observed as indicated in Figure 62 with velocities decreasing in speed and reflectivity diminishing with height.

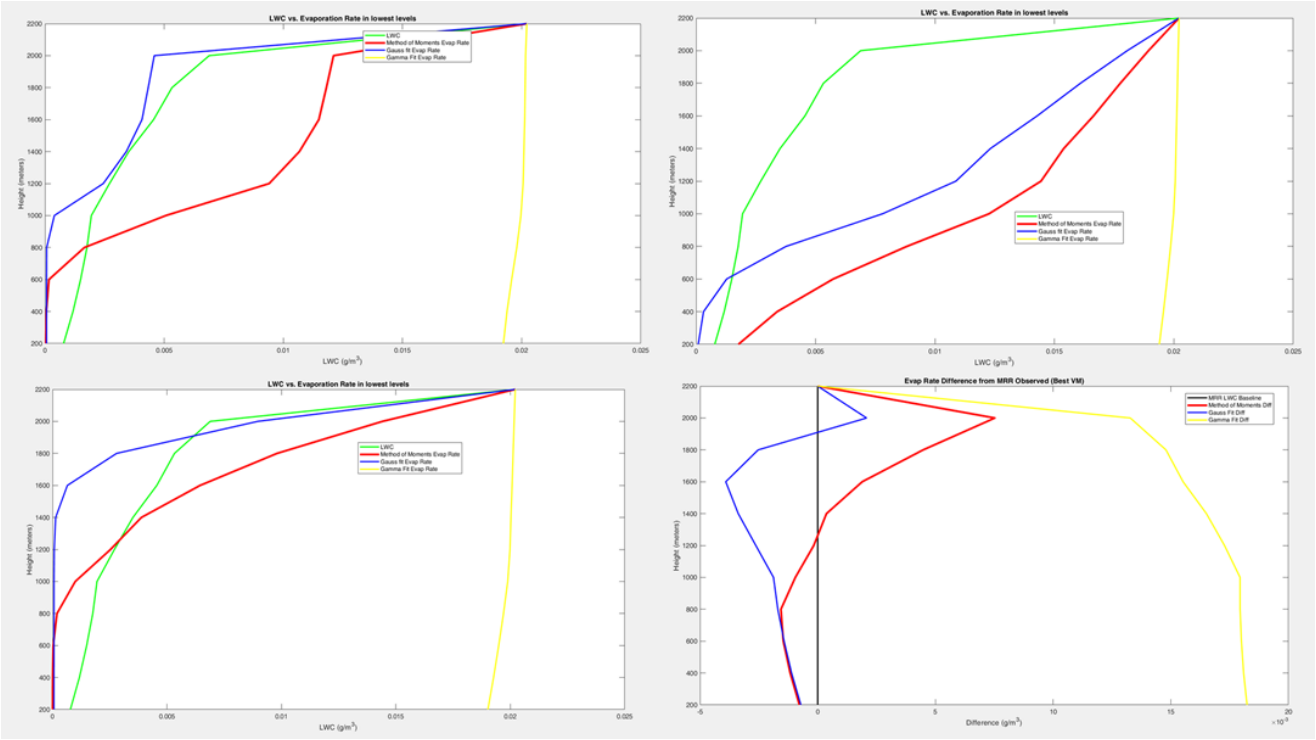

Figure 63 – The evaporation quantifications for 0630Z with varying derived quantities of VM. The top left is the raw sounding derived VM seen for balloon A in Figure 61. The top right is an averaged layer vertical motion of -0.48 m s^{-1}, and the bottom left is no VM. The bottom right shows the difference of the evaporation quantification of the DSD models to the observed MRR LWC.

The derived vertical motions shown in Figure 63 resulted in an underestimation of evaporation in the DSD models. Gauss3 was the closest to the observed quantity and the Gamma once again overestimated the DSD. With 0 vertical motions assumed, the Gauss3 corrects and closely follows the observed evaporation rate until under 2 km where it then overestimates the rate. This may be due in part to evaporative cooling increasing downward forcing at each level. By manually micro-adjusting each level of

the VM, a near perfect Gauss3 fit can be established. This demonstrates the magnitude of impact the VM has at each level.

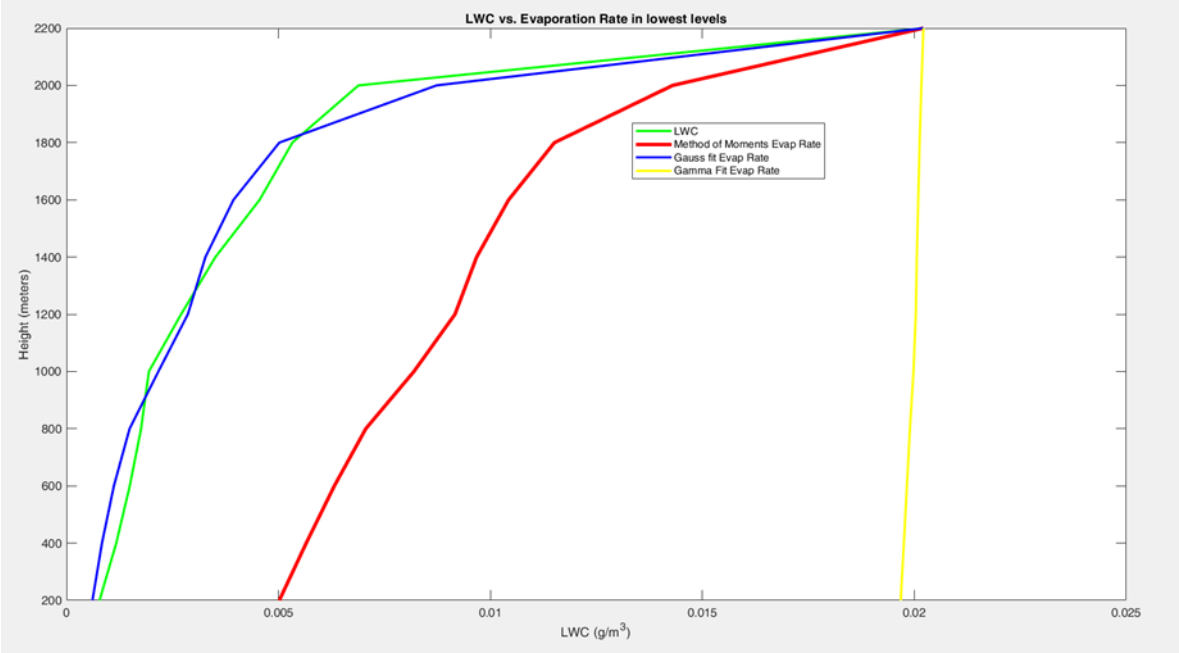

Figure 64 – Evaporation quantification with vertical motions micro-adjusted to match the Gauss3 quantification to the observed evaporation rate.

Adjusting the vertical motions at the top of the layer had greater response to the overall quantification through the column than adjustments at the bottom. A shift of values greater than .003 ms^{-1} at 2.2 km resulted in an inaccurate quantification over the entire column. This response rate is due to the smaller drop sizes at the top of the dry layer having a more significant response to a change in the residence time than the surviving larger drops at the bottom of the layer.

Vertal Motions By Level	200m	400m	600m	800m	1000m	1200m	1400m	1600m	2000m	2200m
Micro Adjusted (m/s)	-3	-2.8	-2.5	-1.5	-1	-0.8	-0.7	-0.4	-0.1	0.003
Balloon Derived VM (m/s)	-0.78249	-0.18902	0.024131	-0.086078	-0.24584	-0.660287	-1.8766	0.046513	-0.63178	0.386438
Averaged VM (m/s)	-0.41	-0.41	-0.41	-0.41	-0.41	-0.41	-0.41	-0.41	-0.41	-0.41

Table 9 – The vertical motions quantities in m s^{-1} used in the evaporation quantifications for Figures 63 and 64.

One reason to quantify evaporation is to make better estimations of cold pool development. In doing this, just matching the quantification at the bottom of the layer is not sufficient. A well-matched quantification of the entire column will be important, and the most sensitive part of the layer is directly beneath the cloud base. This was true for all the cases in question and was an important consideration in quantifying evaporation. The magnitude of the VM evaporation impact directly below the cloud base may be virtually impossible to observe or resolve numerically when considering these results. Even the highest resolution models are orders of magnitude larger than the quantity to be resolved, thus development of other parameterization and observation methods will need to be considered in future studies.

3.3.2 March 09th, 2019 Balloon B Analysis

The next quantifications were made at the 0800Z Balloon B launch set for 0810Z to capture the heaviest rainfall. This quantification demonstrates how the model handles the change in drop sizes in cases where steady rain is passing over the MRR. Quantification of the evolution of the DSD was important in making adjustments to rain rate calculations in QPF forecasts and radar rain estimations. The melting layer height increased slightly at this time to 2.4 km, and was used as the base for the quantification. Attenuation of the radar signal is shown in Figure 62 just before 08Z, but should not have an impact in the quantifications as the MRR has attenuation correction that applies to the DSD. Additionally, erroneous data was observed in the sounding profile, but this was also above the layer being quantified in this case and did not affect the results.

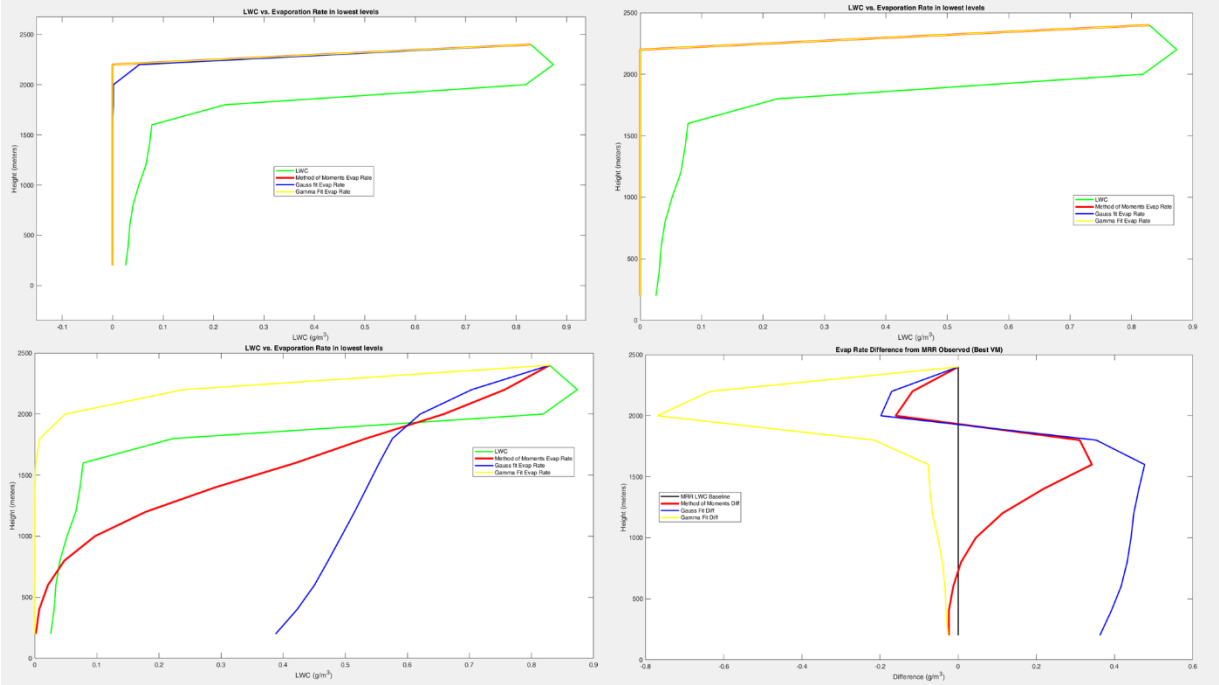

Figure 65 – Evaporation model with derived VM (top left), averaged vertical motion (top right) and no vertical motion (bottom left) for May 9th 2020 at 0815Z. The bottom right panel is the difference of the model evaporation rates (colored lines) to the observed evaporation rates (black 0 line) with no VM included. Accuracy is determined by how close the colored lines are to the 0 line.

In Figure 65 any VM caused an overestimation of evaporation in the profile. No vertical motion displayed a better quantification through the dry layer for all the DSD models. The MOM DSD was overall the most accurate of the three, while the Gamma overestimates the evaporation and the Gauss3 underestimates it.

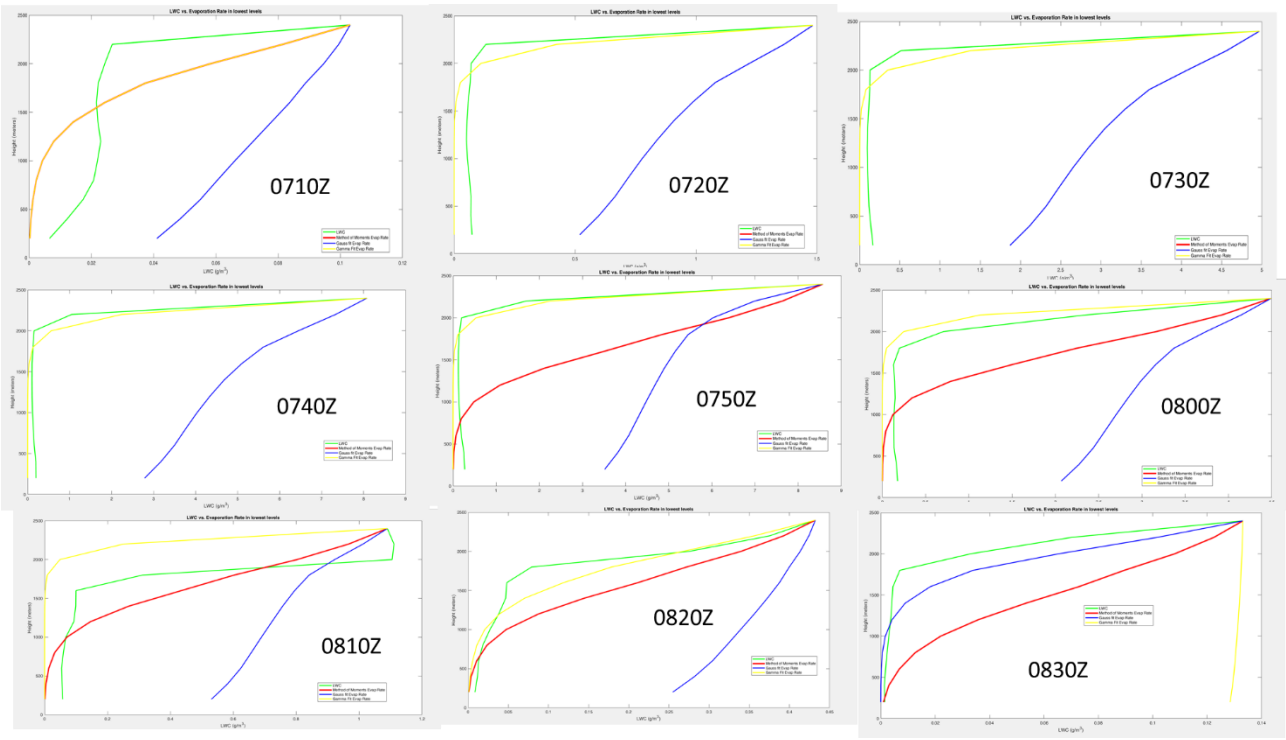

Figure 66 – The evaporation model results for each 10-minute increment of the heavy rainfall on March 09th 2020. This assumes no VM in the quantification and the Balloon B sounding.

Using balloon B as the representative sounding for the entire heavy rain event, some inferences can be made about each model's performance when examining the output for each 10-minute period (Figure 66). The Gauss3 had the tendency to underestimate the total evaporation rates for most of the timeframes while the Gamma and the MOM made representative estimations. In the 0830Z quantification, the Gauss3 and the MOM closely represent the observed evaporation rate while the Gamma understates the evaporation. While it may seem like Gamma and MOM made better quantifications overall, the lack of a vertical motion component may demonstrate a false quantification.

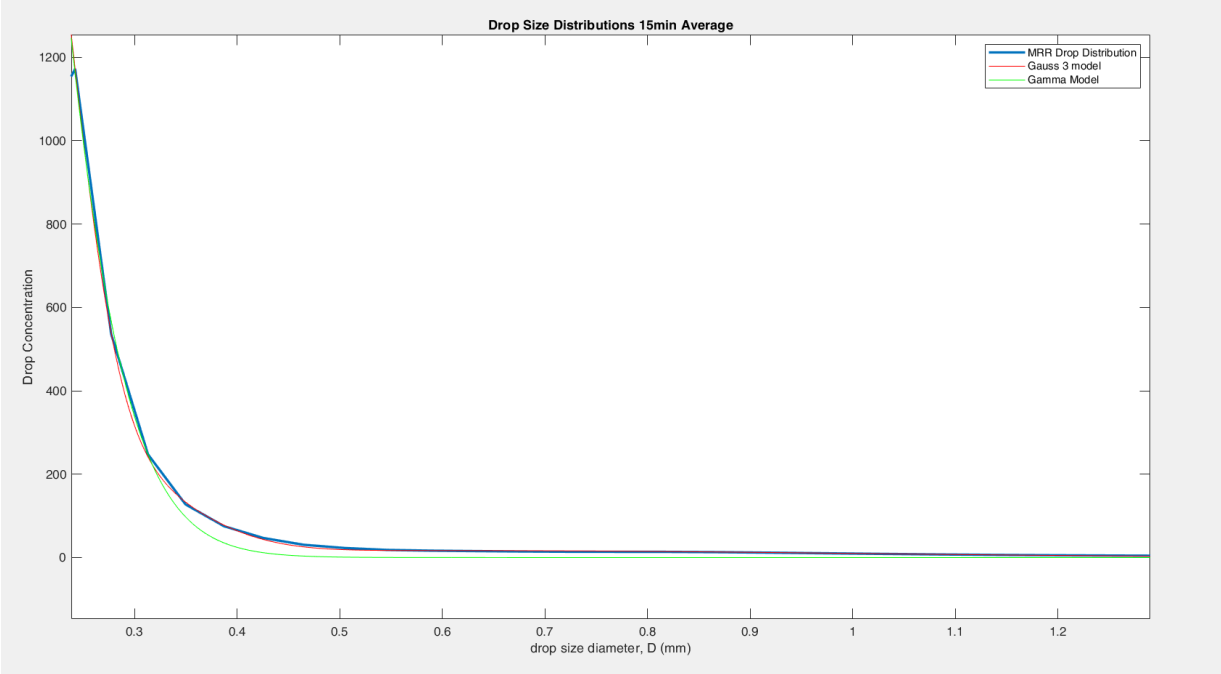

Figure 67 – The MRR observed DSD with the modeled Gauss3 and Gamma DSDs from March 9th, 2020 at 0810Z.

In cases of heavier rainfall, the Gamma distribution underestimates larger drop concentrations signified by the Gamma (green line) underneath the tail of observed larger diameters (blue line) seen in Figure 67 and was observed in all the time frames that evaporation rates were underestimated in the Gauss3. This suggests that the under quantification of the DSD of the larger drops may have been offset by lack of observed VM, resulting in a falsely accurate evaporation estimation for the Gamma and MOM. At the 0830Z time, rainfall at the surface had slowed and the observed DSD from the MRR showed little concentration of larger drops. This has allowed the Gauss and MOM to make an accurate quantification while the Gamma is overestimating the number of smaller drops, therefore underestimating evaporation. What can be inferred is that even with an accurate evaporation quantification, an evaluation of the DSD also needs to be evaluated in this model when considering vertical motions. If the DSD fit and the

evaporation rates are accurate, this increases the likelihood that a truly accurate quantification has been made.

3.3.3 March 09th, 2019 Balloon C Analysis

The last case examined is the quantifications using the balloon C sounding profile. In this case, lighter rain was being observed by the lighter echoes between 20 dBZ-25 dBZ. The reduction of reflectivity and fall velocities were not as evident as in the first two cases, therefore the evaporation rates would be less pronounced. This would also be expected in the evaporation models. The base of the freezing layer lowers back down to the 2.2 km level and is the base level in the evaporation model.

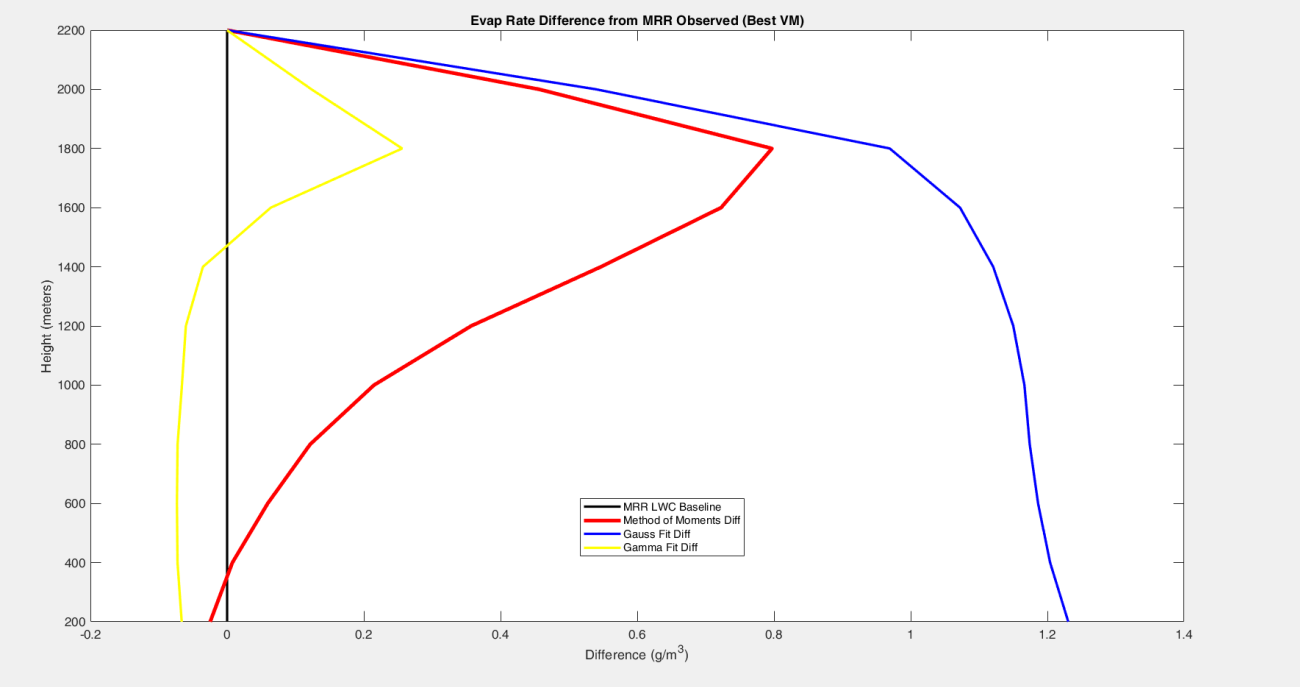

Figure 68 – Evaporation comparison using the difference of the observed evaporation to the Gauss3, MOM and the Gamma DSD models for March 09th 2020 at 0945Z.

The first run of the evaporation model under the balloon C sounding was taken at 0945Z with no VM input. The Gauss3 distribution once again underestimates the evaporation rates. The Gamma model follows the evaporation rate the closest while the

MOM has the best quantification at the LOL. The disdrometer observes the LWC at the surface as 0.06 g m^{-3} while the MOM shows a 0.04 g m^{-3} at the lowest observable level making for a reasonable quantification. Using the derived VM in the equation, the quantification doesn't change significantly with Gauss3 and calculates a better quantification for the Gamma and the MOM. The response of adding VM was most notable below the cloud base as positive difference in LWC for the MOM (0.8 g m^{-3}) and the Gamma (0.2 g m^{-3}) both switch to a negative difference of approximately -0.5 g m^{-3} before reaching the LOL level difference around 0.

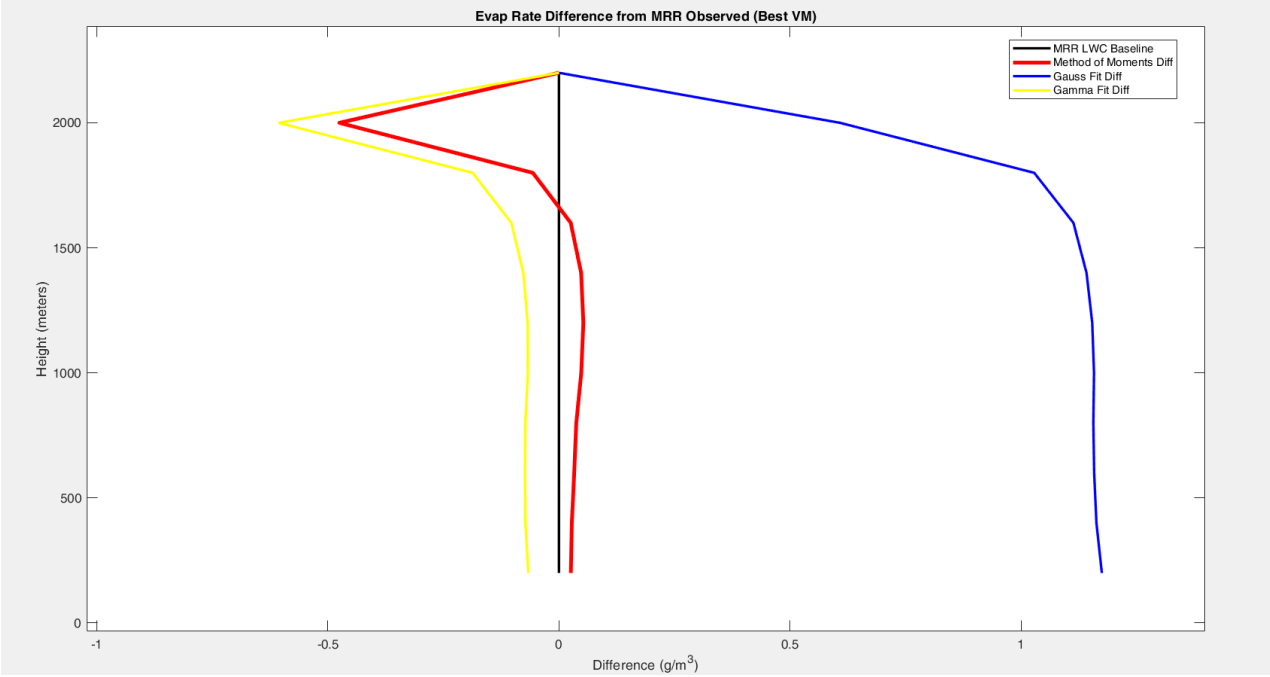

Figure 69 – Evaporation comparison using the difference of the observed evaporation to the Gauss3, MOM and the Gamma DSD models for March 09th 2020 at 0945Z with Balloon derived VM.

The results of the under quantification of evaporation in the Gauss3 is due to the overestimation of the DSD. Because the MOM and Gamma match the overall evaporation rates well with the vertical motions, and the modeled DSD matches the

observed MRR DSD, the quantities calculated in this instance can be taken with high confidence in their accuracy.

3.3.4 March 09th, 2019 Model Environment Analysis

The last area of examination is how the modeled sounding environment responds to the evaporation model and how that compares to the real sounding. This was done in the same way as the November 20th, 2019 case study, by comparing the averaged RH of the dry layer in the observed soundings to the modeled environment, then running the evaporation model through the most representative soundings and examining the results. This allowed an assessment of the accuracy of the modeled environment. The comparison will be made to the real sounding with the most accurate of the evaporation model data, which in this case was balloon B with no VM considered at 0820Z.

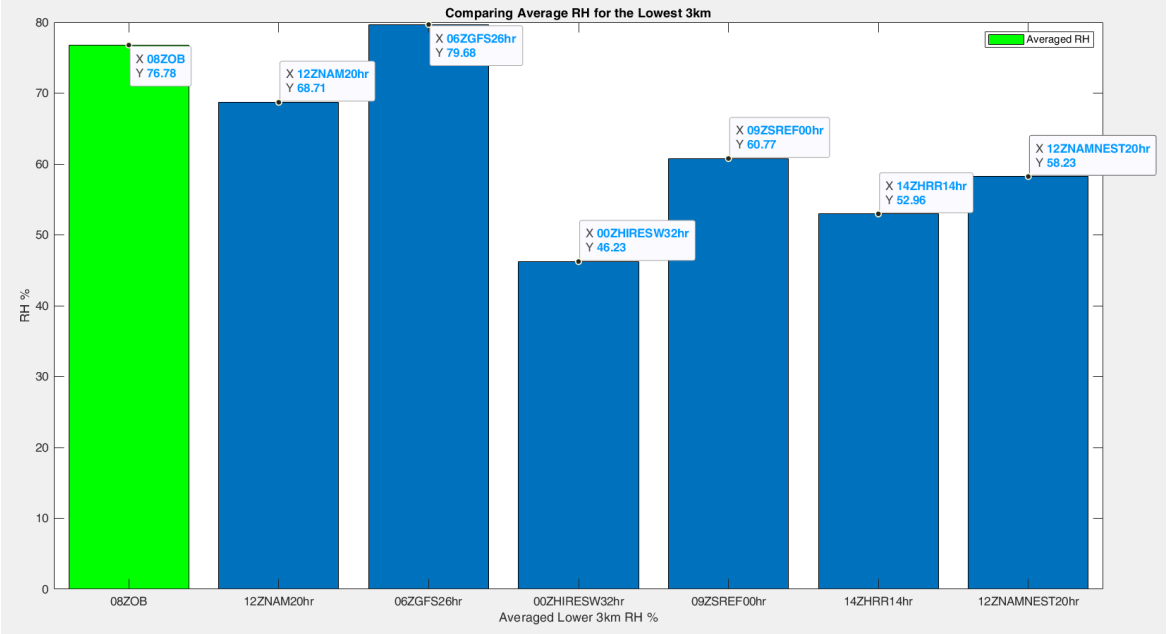

Figure 70 – Profile comparison of the average lower 3 km RH%. The green bar represents the observed balloon B sounding while the balloon bars represent the model outputs.

The models available for this case were gathered at 14Z on the 8th of March, apart from the 09Z 00hr SREF, which was collected the next morning. The 06Z GFS 26hr model matched the best with the average lower 3 km RH. The NAM was the second-best match and the SREF was the next.

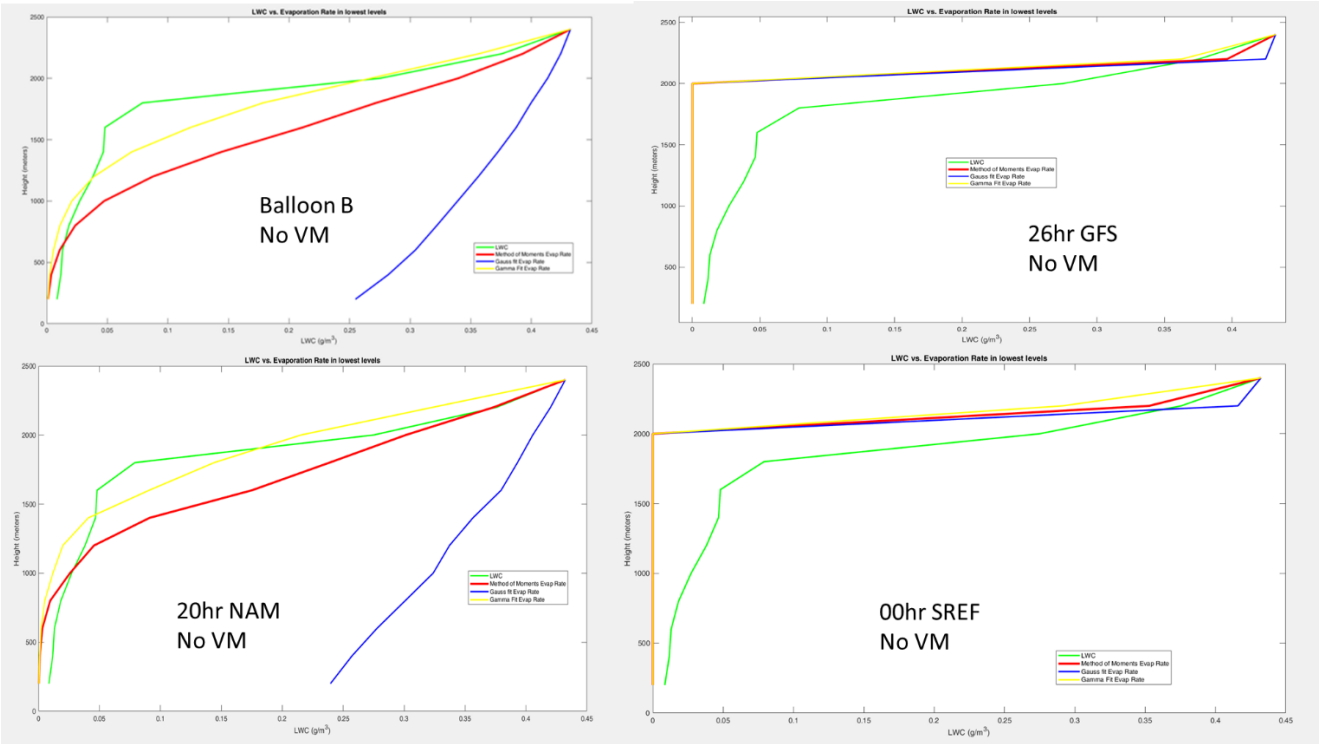

Figure 71 – 0820Z model comparison.

In comparing the model outputs for the closest RH lower level averages, the NAM was the most representative evaporation model to the balloon B output. Although the GFS had a better representation of the average RH in the lower 3 km, it still holds true that the profile best suited for comparison needs to have a higher resolution in the lower levels, and the RH values at the cloud base had the most impact on the total evaporation rates.

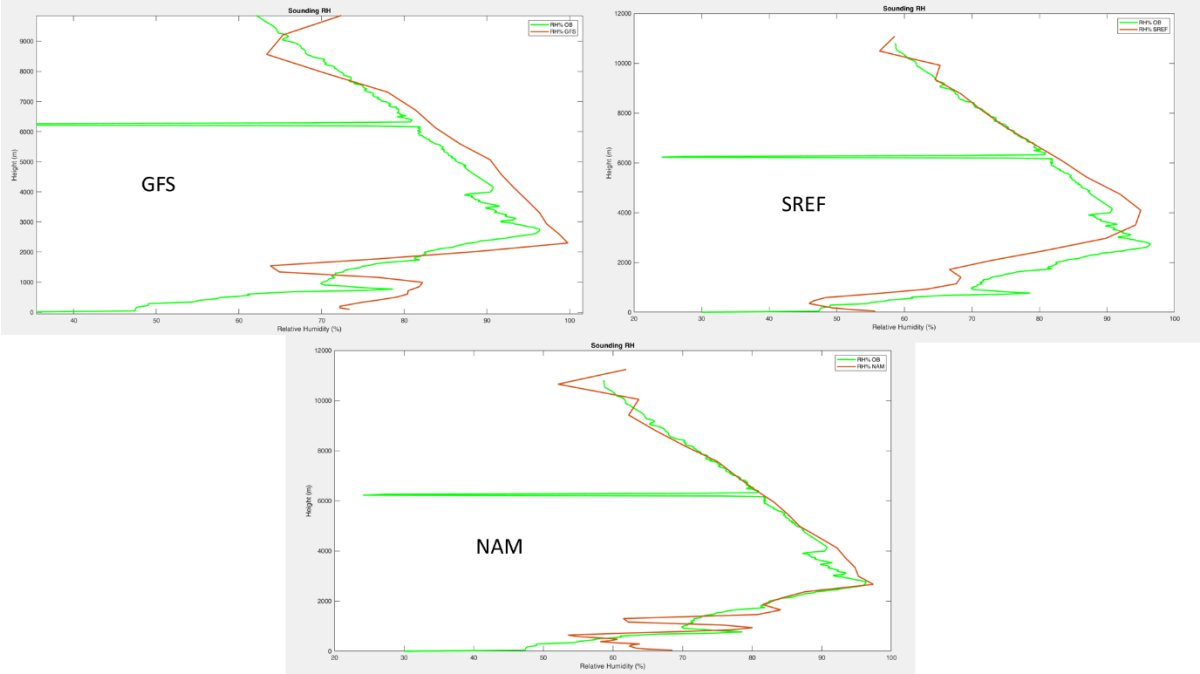

Figure 72 – Comparing the NAM, SREF and GFS model RH profile to the observed profile of balloon B.

The GFS model in Figure 72 shows a deeper and drier layer between 1.9 km down to 0.99 km that extends to 65% RH where the observed dry layer reaches 70% RH. The NAM also displays a drier environment than the observed sounding at 63% RH, however this layer is not as deep as the GFS and extends from 1.4 km to 0.93 km. As a result, the modeled evaporation in the NAM profile does not result in an over quantification of evaporation like it does in the GFS profile. The SREF model represents the trends of the profile well, but is dryer throughout the column, resulting in an over estimation for all DSD models.

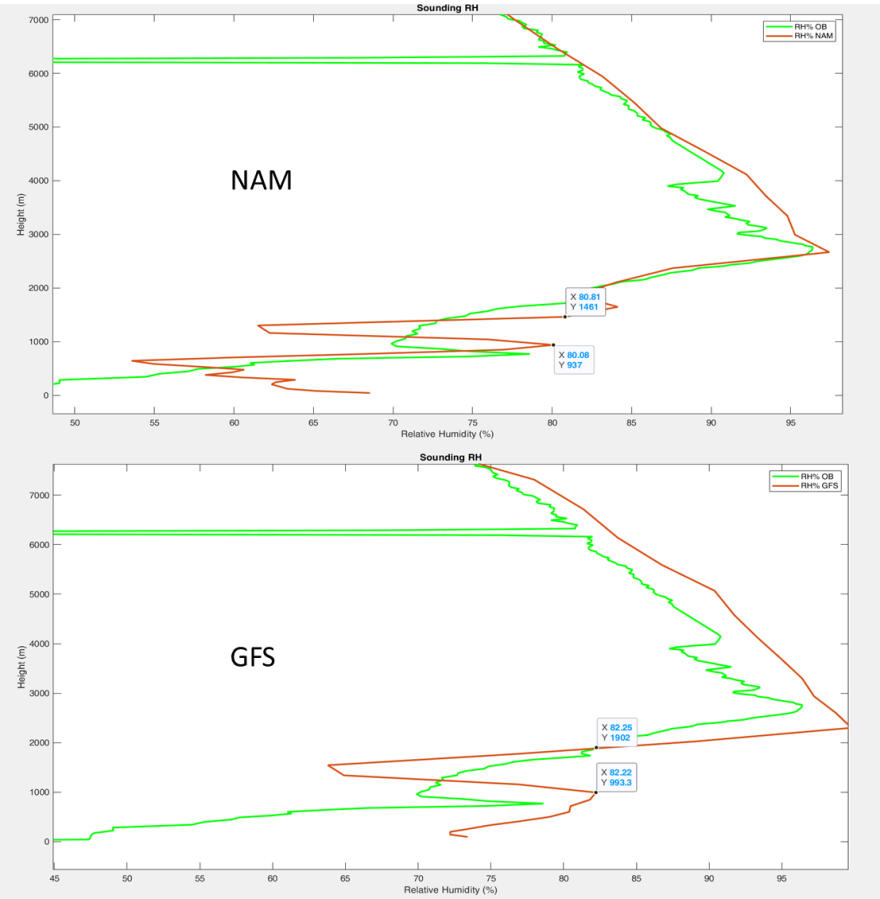

Figure 73 – Comparing the dry layers below the cloud base of the GFS, NAM and Observed 08Z soundings.

In the cases presented, the NAM model shows consistent representation of the lower level environmental profile that can be accurately used in the evaporation model. Although the NAM profiles were older runs of +16 hours out, evaporation was quantified well when compared to the observed soundings. Many operational forecasters make predictions within this timeframe, thus when the evaporation model is fully quantified, coupling short-range forecast soundings with potential evaporation could contribute to accurate quantities of low-level evaporation, improving a host of forecasting parameters. More work will need to be accomplished with the higher-resolution models for an accurate representation to alleviate the need of future balloon comparisons.

4. Conclusions

Because the evolution of the DSD played the largest role in the evaporation quantification for the observed environmental profiles, a new DSD model in the Gauss3 was developed using linear regression computer algorithms. The Gauss3 distribution was also compared with the results to past works in the method of moments (MOM) gamma distribution and a linear regression derived Gamma distribution. The MOM DSD evaporation quantification represented the evaporation rates well most often when vertical motions were not included, but underestimated the tail of larger diameters of the MRR observed DSD. The Gamma fit model proved the least accurate of the models often mis-quantifying the MRR DSD, leading to inaccurate evaporation rates. While the Gamma fit worked well with the laser disdrometer data, it often flattened out and under-quantified the DSDs with the MRR data leading to skewed evaporation results. There is some potential for the Gamma fit distribution in linear regression computer modeling as it performed well in the surface laser disdrometer quantifications. The Gauss3 DSD model was the most accurate of the evaporation rates overall. It modeled evaporation throughout the dry layer consistently when vertical motions were included in the calculations and had the best accuracy in modeling the MRR DSD. Understanding and improving DSD modeling with machine learning is an area of study that would significantly improve many forecasting parameters. Including controlled studies using rain tower simulations would also help with DSD quantification.

The case studies examined revealed several issues in the quantification of evaporation as it relates to VM. Bongard (2019) revealed the importance of accurate VM quantities. However, balloon-derived VMs seldom produced accurate quantifications.

This problem was exacerbated in cases where rainfall skewed the results of the balloon VM derivatives. Using derived vertical motions most often caused an over-quantification of evaporation. Using a further averaged derived VM helped in some instances, but was still not always accurate. The cases also revealed that evaporation quantifications may be accurate for the wrong reasons. High confidence in the evaporation model can be designated only if reasonable VMs are included and the modeled DSD fit is representative of the MRR DSD. Furthermore, VM and the depth of the dry pockets in the RH profile have the greatest response immediately below the cloud base. This is due to the higher concentrations of smaller drops and the sensitivity of smaller drops to the residence time as well as the depth of the DPD directly below the cloud base. Lastly, an accurate evaporation representation not only means that the LWC matches at the LOL, but the evaporation rate must match through the height of the dry layer. Micro-adjusting the vertical motions disclosed that an accurate VM needs to be coupled with an accurate DSD to maintain a sense of accurate evaporation rates through the entire column. This is especially important when considering estimations of cold pool development due to evaporative cooling. Finding a relationship for the adiabatic trends of the profile to the vertical motions could be a way to accurately quantify evaporation using model derived RH profiles. Also using the omega value output may be of some use with more study. Radar estimations of vertical motions induced by convergence zones also shows some potential in quantifying the accuracy of vertical motions and improve radar rain rate estimations. This will be an area for future study.

Although older model data was used in the evaporation computations, the NAM model was a respectable representation within a 20hr forecast period. This is a significant

observation as operational forecasters can use this to improve the accuracy of QPF forecasts a day in advance. Evaporation quantification is most sensitive to the resolution of the low-level environment. Environmental profiles with higher resolution, especially in the boundary layer work better with the evaporation quantification. The GFS represented the environment well overall, but for a microscale feature like evaporation, it was not well enumerated. High-resolution models like the RAP, NAMnest and the HRRR have the potential to be used as representative profiles in newer model runs, but do not serve the purpose of evaporation quantification greater than 20hrs from the observed time. More study will be needed in this area to determine accurate forecast ranges for these models. For the purpose of future study in evaporation quantification, the NAM within a 20hr forecast period is a decent profile representation.

These quantifications of evaporation would serve the meteorology and hydrology forecasting communities well in improving radar rainfall estimations, quantitative precipitation forecasts, as well as flooding and cold pool development amongst a host of other forecasting parameters. However, more work will first need to be accomplished in incorporating this data into forecasting models to make meaningful predictions. This research could also extend to quantifying ice crystal sublimation for snow total forecasting. Solving these parameters will require even more case studies to resolve some of the finer issues in DSD modeling with linear regression computer modeling and laser disdrometers. Also, more work is needed to incorporate this data into practical forecasting QPF tools. By quantifying the latent heat exchange resolved by the evaporation model, improvements in forecasting downdrafts, cold pooling and

thunderstorm initiation could be made. The results in this study have provided promising avenues to be explored to improve these and many more forecasting endeavors.

References

Alonge, A. A., and T. J. Afullo, 2012: Seasonal analysis and prediction of rain-fall effects in Eastern South Africa at microwave frequencies. *Prog. Electromagn. Res. B*, **40**, 279–303, https://doi.org/10.2528/PIERB12020305.

Atlas, D., and C. W. Ulbrich, 1976: Path and Area-Integrated Rainfall Measurement By Microwave Attenuation in the 1-3 Cm Band. 406–413, https://doi.org/10.1175/1520-0450(1977)016<1322:paairm>2.0.co;2.

Barth, M. C., and D. B. Parsons, 1996: Microphysical processes associated with intense frontal rainbands and the effect of evaporation and melting on frontal dynamics. *J. Atmos. Sci.*, **53**, 1569–1586, https://doi.org/10.1175/1520-0469(1996)053<1569:MPAWIF>2.0.CO;2.

Best, A. C., 1950: The size distribution of raindrops. *Q. J. R. Meteorol. Soc.*, **76**, 16–36, https://doi.org/10.1002/qj.49707632704.

Bongard, J., 2019: Quantifying Evaporation of Precipitation Below the Cloud Base Using a Vertically Pointing Radar. University of Missouri - Columbia, 60 pp.

Bradley, S. G., and C. D. Stow, 1977: The Effect of Raindrop Interactions on Observed Drop Size Distributions. *J. Appl. Meteorol.*, **16**, 1206–1213, https://doi.org/10.1175/1520-0450(1977)016<1206:teorio>2.0.co;2.

Carollo, F. G., and V. Ferro, 2015: Modeling rainfall erosivity by measured drop-size distributions. *J. Hydrol. Eng.*, **20**, 1–7, https://doi.org/10.1061/(ASCE)HE.1943-5584.0001077.

Duda, J. D., X. Wang, F. Kong, and M. Xue, 2014: Using varied microphysics to account for uncertainty in warm-season QPF in a convection-allowing ensemble. *Mon. Weather Rev.*, **142**, 2198–2219, https://doi.org/10.1175/MWR-D-13-00297.1.

Feingold, G., and Z. Levin, 1986: The lognormal fit to raindrop spectra from frontal convective clouds in Israel. *J. Clim. Appl. Meteorol.*, **25**, 1346–1363, https://doi.org/10.1175/1520-0450(1986)025<1346:TLFTRS>2.0.CO;2.

——, S. Tzivion, and Z. Levin, 1988: Evolution of raindrop spectra. Part I: solution to the stochastic collection/breakup equation using the method of moments. *J. Atmos. Sci.*, **45**, 3387–3399, https://doi.org/10.1175/1520-0469(1988)045<3387:EORSPI>2.0.CO;2.

Fox, N. I., 2004: TECHNICAL NOTE: The representation of rainfall drop-size distribution and kinetic energy. *Hydrol. Earth Syst. Sci.*, **8**, 1001–1007, https://doi.org/10.5194/hess-8-1001-2004.

Georgakakos, K. P., and M. D. Hudlow, 1984: Quantitative precipitation forecast techniques for use in hydrologic forecasting. *Bull. - Am. Meteorol. Soc.*, **65**, 1186–1200, https://doi.org/10.1175/1520-0477(1984)065<1186:QPFTFU>2.0.CO;2.

Gunn, R., and G. Kinzer, 1948: The Terminal Velocity of Fall for Water Droplets in Stagnant Air. *J. Meteorol.*, **6**, 243–248.

Kinzer, G. D., and R. Gunn, 1951: the Evaporation, Temperature and Thermal Relaxation-Time of Freely Falling Waterdrops. *J. Meteorol.*, **8**, 71–83, https://doi.org/10.1175/1520-0469(1951)008<0071:tetatr>2.0.co;2.

Kostinski, A. B., and A. R. Jameson, 1997: Fluctuation properties of precipitation. Part I: On deviations of single-size drop counts from the poisson distribution. *J. Atmos. Sci.*, **54**, 2174–2186, https://doi.org/10.1175/1520-0469(1997)054<2174:FPOPPI>2.0.CO;2.

Li, X., and R. C. Srivastava, 2001: An analytical solution for raindrop evaporation and its application to radar rainfall measurements. *J. Appl. Meteorol.*, **40**, 1607–1616, https://doi.org/10.1175/1520-0450(2001)040<1607:AASFRE>2.0.CO;2.

Licznar, P., and W. F. Krajewski, 2016: Precipitation Type Specific Radar Reflectivity-Rain Rate Relationships for Warsaw, Poland. *Acta Geophys.*, **64**, 1840–1857, https://doi.org/10.1515/acgeo-2016-0071.

Löffler-Mang, M., and J. Joss, 2000: An optical disdrometer for measuring size and velocity of hydrometeors. *J. Atmos. Ocean. Technol.*, **17**, 130–139, https://doi.org/10.1175/1520-0426(2000)017<0130:AODFMS>2.0.CO;2.

Markowitz, A. H., 1976: Raindrop Size Distribution Expressions. https://doi.org/10.1175/1520-0450(1976)015<1029:RSDE>2.0.CO;2.

Marshall, J. S., and W. M. K. Palmer, 1948: THE DISTRIBUTION OF RAINDROPS WITH SIZE. *J. Meteorol.*, **5**, 165–166, https://doi.org/10.1175/1520-0469(1948)005<0165:tdorws>2.0.co;2.

Moisseev, D. N., and V. Chandrasekar, 2007: Nonparametric estimation of raindrop size distributions from dual-polarization radar spectral observations. *J. Atmos. Ocean. Technol.*, **24**, 1008–1018, https://doi.org/10.1175/JTECH2024.1.

Ochou, A. D., A. Nzeukou, and H. Sauvageot, 2007: Parametrization of drop size distribution with rain rate. *Atmos. Res.*, **84**, 58–66, https://doi.org/10.1016/j.atmosres.2006.05.003.

Pallardy, Q., and N. I. Fox, 2018: Accounting for rainfall evaporation using dual-polarization radar and mesoscale model data. *J. Hydrol.*, **557**, 573–588, https://doi.org/10.1016/j.jhydrol.2017.12.058.

Peters, G., B. Fischer, and M. Clemens, 2010: Rain attenuation of radar echoes considering finite-range resolution and using drop size distributions. *J. Atmos. Ocean. Technol.*, **27**, 829–842, https://doi.org/10.1175/2009JTECHA1342.1.

Rogers, R. R. R., and M. K. Yau, 1996: Short Course in Cloud Physics. 295.

Sciences, A., 1997: Iselin&Gutowski-MWR97.pdf. 1954–1963.

Seifert, A., 2008: On the parameterization of evaporation of raindrops as simulated by a one-dimensional rainshaft model. *J. Atmos. Sci.*, **65**, 3608–3619, https://doi.org/10.1175/2008JAS2586.1.

Serio, M. A., F. G. Carollo, and V. Ferro, 2019: Raindrop size distribution and terminal velocity for rainfall erosivity studies. A review. *J. Hydrol.*, **576**, 210–228, https://doi.org/10.1016/j.jhydrol.2019.06.040.

Siscoe, G. L., and Z. Levin, 1971: Water-drop-surface-wave interactions. *J. Geophys. Res.*, **76**, 5112–5116, https://doi.org/10.1029/jc076i021p05112.

Testud, J., E. Le Bouar, E. Obligis, and M. Ali-Mehenni, 2000: The rain profiling algorithm applied to polarimetric weather radar. *J. Atmos. Ocean. Technol.*, **17**, 332–356, https://doi.org/10.1175/1520-0426(2000)017<0332:TRPAAT>2.0.CO;2.

Tokay, A., A. Kruger, and W. F. Krajewski, 2001: Comparison of drop size distribution measurements by impact and optical disdrometers. *J. Appl. Meteorol.*, **40**, 2083–2097, https://doi.org/10.1175/1520-0450(2001)040<2083:CODSDM>2.0.CO;2.

Ulbrich, C. W., 1983: Natural variations in the analytical form of the raindrop size distribution. *J. Clim. Appl. Meteorol.*, **22**, 1764–1775, https://doi.org/10.1175/1520-0450(1983)022<1764:NVITAF>2.0.CO;2.

Weibull, W., 1951: Wide applicability. *J. Appl. Mech.*, **103**, 293–297.

Wilks, D. S., 1989: Rainfall Intensity, the Weibull Distribution, and Estimation of Daily Surface Runoff. https://doi.org/10.1175/1520-0450(1989)028<0052:RITWDA>2.0.CO;2.

Williams, C. R., 2016: Reflectivity and liquid water content vertical decomposition diagrams to diagnose vertical evolution of raindrop size distributions. *J. Atmos. Ocean. Technol.*, **33**, 579–595, https://doi.org/10.1175/JTECH-D-15-0208.1.

Willis, P. T., 1984: Functional Fits to Some Observed Drop Size Distributions and Parameterization of Rain. *http://dx.doi.org/10.1175/1520-0469(1984)041<1648:FFTSOD>2.0.CO;2*.

Willis, P. T., and P. Tattelman, 1989: Drop-size distributions associated with intense rainfall. *J. Appl. Meteorol.*, **28**, 3–15, https://doi.org/10.1175/1520-0450(1989)028<0003:DSDAWI>2.0.CO;2.